uOttawa

L'Université canadienne
Canada's university

**FACULTÉ DES ÉTUDES SUPÉRIEURES
ET POSTOCTORALES**

uOttawa

L'Université canadienne
Canada's university

**FACULTY OF GRADUATE AND
POSDOCTORAL STUDIES**

Leslie R. Lamb
AUTEUR DE LA THÈSE / AUTHOR OF THESIS

M.Sc. (Human Kinetics)
GRADE / DEGREE

School of Human Kinetics
FACULTÉ, ÉCOLE, DÉPARTEMENT / FACULTY, SCHOOL, DEPARTMENT

Contribution of Air Flow to Impact Attenuation in Chamber Structures
TITRE DE LA THÈSE / TITLE OF THESIS

Thomas Blaine Hoshizaki
DIRECTEUR (DIRECTRICE) DE LA THÈSE / THESIS SUPERVISOR

CO-DIRECTEUR (CO-DIRECTRICE) DE LA THÈSE / THESIS CO-SUPERVISOR

EXAMINATEURS (EXAMINATRICES) DE LA THÈSE / THESIS EXAMINERS

Gordon Robertson

Jing Xian Li

Gary W. Slater
Le Doyen de la Faculté des études supérieures et postdoctorales / Dean of the Faculty of Graduate and Postdoctoral Studies

CONTRIBUTION OF AIR FLOW TO IMPACT ATTENUATION IN CHAMBER STRUCTURES

by

Leslie R. Lamb

Thesis submitted to the
Faculty of Graduate and Postdoctoral Studies,
in partial fulfillment of the requirement for the degree of Master of Science

School of Human Kinetics
Faculty of Health Science
University of Ottawa

Library and
Archives Canada

Published Heritage
Branch

395 Wellington Street
Ottawa ON K1A 0N4
Canada

Bibliothèque et
Archives Canada

Direction du
Patrimoine de l'édition

395, rue Wellington
Ottawa ON K1A 0N4
Canada

Your file Votre référence
ISBN: 978-0-494-46486-1
Our file Notre référence
ISBN: 978-0-494-46486-1

NOTICE:
The author has granted a non-exclusive license allowing Library and Archives Canada to reproduce, publish, archive, preserve, conserve, communicate to the public by telecommunication or on the Internet, loan, distribute and sell theses worldwide, for commercial or non-commercial purposes, in microform, paper, electronic and/or any other formats.

The author retains copyright ownership and moral rights in this thesis. Neither the thesis nor substantial extracts from it may be printed or otherwise reproduced without the author's permission.

AVIS:
L'auteur a accordé une licence non exclusive permettant à la Bibliothèque et Archives Canada de reproduire, publier, archiver, sauvegarder, conserver, transmettre au public par télécommunication ou par l'Internet, prêter, distribuer et vendre des thèses partout dans le monde, à des fins commerciales ou autres, sur support microforme, papier, électronique et/ou autres formats.

L'auteur conserve la propriété du droit d'auteur et des droits moraux qui protège cette thèse. Ni la thèse ni des extraits substantiels de celle-ci ne doivent être imprimés ou autrement reproduits sans son autorisation.

In compliance with the Canadian Privacy Act some supporting forms may have been removed from this thesis.

While these forms may be included in the document page count, their removal does not represent any loss of content from the thesis.

Conformément à la loi canadienne sur la protection de la vie privée, quelques formulaires secondaires ont été enlevés de cette thèse.

Bien que ces formulaires aient inclus dans la pagination, il n'y aura aucun contenu manquant.

Canada

ABSTRACT

Head injuries are a major cause of morbidity and mortality worldwide, many resulting from sporting activities. Currently, there is a need in the head protection industry for improved technology capable of reducing the risk of mild and severe head injuries. Contemporary head protection devices are comprised mainly of foam and have several inherent disadvantages, including a limited ability to provide effective energy absorption under both low and high impact velocities. New thin-walled collapsible chamber energy absorption systems may resolve this problem. The chambers consist of four engineering elements which alter their performance - geometry, air volume, material, and venting system. This research analyzed the contribution of air flow through an orifice to the chamber's management of impact energy. The main objective of the study was to determine the effect of the chamber's vent diameter on peak force and venting rate during an impact. Two material stiffnesses and five vent diameters were tested at three inbound velocities. Each chamber was impacted ten times using a monorail drop system. Significant main effects were found for material stiffness, vent diameter, and inbound velocity on peak force and venting rate ($p<0.0001$). Under low inbound velocities the largest vent diameters transmitted less force than the smallest, while this relationship reversed at high inbound velocities. Under low velocities air flow rate was negatively, and flow duration was positively correlated to peak force. Under high velocities, air flow rate was positively, and duration was negatively correlated to peak force. This suggested that under low velocities chambers performed optimally when air was dissipated fast, for a short duration; however, as the chamber approached a critical failure region, the increased duration and decreased velocity of air released prevented larger peak forces. Overall, this research confirmed that engineered thin-walled collapsible chambers use air as a mechanism to absorb impacting force.

ACKNOWLEDGEMENTS

Over the course of the last two years, I have had the opportunity to work with incredibly supportive and knowledgeable individuals. I would like to extend my deepest appreciation to each of them for their participation in this project and influence on my life. First, I would like to express my sincere gratitude to my supervisor, Dr. Blaine Hoshizaki. Dr. Hoshizaki is the most inspirational and motivational individual I have ever worked with. I am grateful for his insight, guidance, and knowledge as I completed this degree. He has encouraged and supported my career choices and has prepared me for future research in my career. It has truly been an honour and a privilege to work with him.

I would like to thank Andrew Post, our lab research coordinator who guided me every step of the way as I completed my thesis. Andrew's technical expertise in impact science are invaluable, and I am grateful for his advice on aspects of my thesis. In addition, I would like to thank Genille Gimbel, Philip Rousseau, and Natalie Coulson, my three lab peers, for countless discussions on all projects and for truly making this a fun experience. Good luck to all of you!

I would also like to express my gratitude to my advisory committee members, Dr. Gordon Robertson and Dr. Jing Xian Li for their valuable suggestions and guidance. I am grateful to Dr. Sadok Guellouz, who assisted in establishing the methodology of my study and Dr. Stavros Tavoularis for the use of his equipment to complete this project. I would also like to thank Xenith LLC for financial support of the Neurotrauma Impact Laboratory. I sincerely hope this study assists in the development of their product, capable of protecting the brain from injury.

Last, but not least, I would like to thank my family and friends for their love, support and encouragement as I completed this thesis. Thank you mom and dad for always being a constant pillar of support and encouragement throughout this degree and my entire education.

TABLE OF CONTENTS

LIST OF TABLES

LIST OF FIGURES

CHAPTER 1. INTRODUCTION

Head injuries are a major cause of morbidity and mortality worldwide (Zhang, Yang & King, 2004). In Canada, there were 16,811 hospitalizations due to traumatic brain injuries (TBIs) in 2003-2004, representing 9% of all trauma admissions that year (Canadian Institute for Health Information, 2006). In the United States, approximately 2 million people suffer TBIs each year (Kraus & McArthur, 1996). The estimated cost of TBIs, including medical costs and lost productivity, averages $3 billion a year in Canada and $60 billion a year alone in the United States (Brain Injury Association of Alberta, 2008; Finkelstein, Corso & Miller, 2006). Thus, brain injuries are not only a burden to the sufferers but to society in general due to the heavy economic, social, and emotional costs.

Head injuries incurred while participating in sport are of particular importance due to the potential number of people affected. In recent years, helmet use has increased in Northern European and North American countries due to increased head protection promotion (Hoshizaki & Brien, 2004). Nevertheless, standards which govern helmet design have received little consideration and many head injuries as a result of sport occur even while athletes are wearing helmets (Hoshizaki & Brien, 2004; Zhang et al., 2004).

There is no treatment available to reverse the damage incurred in a TBI; therefore, three options exist to help minimize the risk of injury – (1) not participating in activities which place the brain at a high risk, such as sport; (2) educating people on head injury prevention and protection; and (3) manufacturing head protection devices which manage energy efficiently. Nevertheless, because helmet standards have received minimal attention over the years, there have not been adequate increases in the level of protection which helmets provide (Hoshizaki & Brien, 2004). The technology helmets currently use is over 40 years old (Hoshizaki & Brien,

2004) and does not protect people as well as believed. As a result, it is essential that we find a way to better protect the brain.

One possible way to increase brain protection is through the use of dynamic air chambers in helmet construction - a new method to help reduce head injuries. These elastic, thin-walled, vented air chambers have the potential to absorb more energy than current helmet technology, thereby decreasing the amount of force transmitted to the brain and the possibility of injury. There are several engineering factors which influence how the air chamber absorbs energy, such as its shape, material composition, air volume, and vent diameter. A key element of these chambers involves the air venting system. The air chamber vents are used as a mechanism to manage energy absorption of the chamber. The purpose of the present study is to determine how vent diameter influences energy absorption during impact in the dynamic air chambers.

It is imperative to understand the mechanisms of head injury and possible consequences of an impact to the brain to develop adequate head protection devices which prevent injuries. Furthermore, a thorough understanding of the procedures and standards which govern helmet certification are necessary to ensure these standards are met in the development of new helmet technology. Finally, current helmet designs must be considered when developing new technology, such as the dynamic air chambers, to identify possible areas of improvement for head protection devices, as well as existing technology and ideas which are working well. The review of literature following in Chapter 2 will address these issues.

1.1. Research Description

1.1.1. Statement of Problem

To analyze the contribution of air flow in managing impact energy in a new thin-walled collapsible chamber energy absorption system.

Main Objective: To determine the effect of the chamber's vent diameter on force during an impact.

In addition to studying chamber vent diameter, chamber venting rates will be examined.

Venting Rate Objectives:

1. To determine the relationship between chamber vent diameter and air flow rate during impact under a range of impact velocities.
2. To determine the relationship between vent rate and peak impact force.
3. To determine the relationship between air flow duration and peak impact force.

1.1.2. Hypotheses

1. There will be a significant difference in peak force during an impact for the chambers' vent diameters (1 mm, 2 mm, 3 mm, 4 mm, 5 mm) and material stiffnesses (TPU 45D, TPU 90A).
2. There will be a significant difference in peak air flow rate during an impact for the chambers' vent diameters (IV) (1 mm, 2 mm, 3 mm, 4 mm, 5 mm) and material stiffnesses (TPU 45D, TPU 90A).
3. A significant linear relationship will exist between peak air flow rate and peak force, using Pearson's correlation.
4. A significant linear relationship will exist between air flow duration and peak force, using Pearson's correlation.

1.1.3. Variables

Independent Variables:
Vent diameter - 5 levels: 1 mm, 2 mm, 3 mm, 4 mm, 5 mm
Material stiffnesses - 2 levels: TPU 45D, TPU 90A

Treatment/Stimulus:
Inbound velocities - 1.3 m/s, 2.3 m/s, 3.0 m/s (based on 10, 30, 50 cm drop heights)

Dependent Variables:
Air flow - duration (ms), beginning time (ms), ending time (ms), peak flow rate (m/s)
Force - peak force (N)

1.1.4. Assumptions

For the purpose of this study, the following assumptions were made:

1. It shall be assumed that the vent was perfectly centered above the anemometer.

2. It shall be assumed that the chamber was sealed, so that air did not escape anywhere other than the vent.

3. It shall be assumed that the chamber was filled with smoke immediately before flow visualization impacts.

4. It shall be assumed that the impacting mass and jig/force plate were rigid bodies.

1.1.5. Limitations

For the purpose of this study, the following limitations were made:

1. The anemometer placement was restricted by the dimensions of the steel jig and therefore the distance between the anemometer and orifice was 4 mm. Air flow speeds measured were therefore less than at the orifice.

2. The anemometer sensor placement was done manually and centered by eye. Therefore, it was assumed the vent was centered above the anemometer.

1.1.6. Delimitations

For the purpose of this study, the following delimitations were made:

1. Testing was performed using a monorail drop rig. Consequently, it was assumed that the testing apparatus closely approximates the mechanics of the air chambers in a helmet upon impact.

2. Testing was performed at laboratory temperatures (21-25.5°C). It is unknown if the chambers perform differently under various atmospheric conditions.

3. Forces measured were restricted to a plane orthogonal to the surface of the impactor.

4. Testing was performed using a 5 kg headform.

5. The headform was in the crown position. Since headform positions create different footprints on impact, results are only in reference to this position.

1.1.7. Significance

Protecting the brain through a range of inbound velocities has been problematic for head protection manufacturers for decades. Historically, helmets have been designed to optimally absorb energy for the level of severity in a given sport or activity in which they are used. As a result, many of the materials currently used in helmets provide protection only for severe impacts, such as skull fractures. Many conventional foams used such as vinyl nitrile, are relatively ineffective at optimally absorbing sub-severe impact energy. Standards have precipitated this trend, many only requiring helmets be impacted from one inbound velocity at a very severe level. Nevertheless, mild impacts can result in head injuries such as concussions. Yet, manufacturers continue to design helmets to meet performance requirements in standards, rather than considering the range of impacts that will occur when wearing a helmet (Gilchrist & Mills, 1994).

Air chambers are thin-walled, collapsible energy management systems which may help solve this problem and broaden the range of impact energies over which energy absorption is optimal and effective. There are several engineering elements comprising these structures which influence their energy attenuation capability, such as geometry, material, enclosed air volume, and air venting. Each engineering element needs to be optimized to maximize the amount of energy the chambers are capable of absorbing. This study examined the chambers' air management system and the influence of various vent diameters on the structure's performance. With knowledge of how the air venting system works, chamber venting systems can now be optimized in helmet designs, to ensure optimal protection of the brain and prevention of injury.

CHAPTER 2. REVIEW OF LITERATURE

2.1. Head Injury Mechanisms

The neurophysiology and mechanisms of brain and head injury have been studied comprehensively using observations, experiments, and mathematic modeling (McIntosh & McCrory, 2000). Impact head injuries are caused by the deformation of brain tissues beyond their recoverable limit, resulting in damage to brain structures or changes in normal functioning (Viano, King, Melvin & Weber, 1989). A TBI has been defined by the United States' National Center for Injury Prevention and Control (2006) as a "blow or jolt to the head or a penetrating head injury that disrupts the normal function of the brain" (par. 1). TBIs can range from mild to severe. For example, concussions and many sports related injuries are considered mild events, whereas typical injuries incurred in devastating car accidents, such as skull fractures, are severe events (Bayly et al., 2005).

TBIs can be classified as primary or secondary injuries (Nolan, 2005). Primary TBIs result from an impact to the brain which directly causes neuronal tissue damage. Neurons and glial cells are injured and, consequently, axonal dysfunction occurs. Neurons are the structural cells of the nervous system which conduct messages from one body part to another (Marieb, 2001). Glial cells are the supporting cells of the nervous system and axons are the neuronal structures which carry the nerve impulse away from the neuronal cell body (Marieb, 2001). Changes in severely damaged axons, such as axonal swelling, have been documented to occur within a few minutes of injury (Gaetz, 2004). Typically, injured axons are evident in areas where a change in tissue density exists, such as the grey-white matter interface (Gaetz, 2004). White matter is a substance of the central nervous system (CNS) which contains myelinated nerve fibers. That is, fibers which are surrounded by a fatty sheath. Grey matter is the area in the CNS which contains cell bodies and unmyelinated nerve fibers. Further, axons often alter their direction to accommodate a blood vessel whose location in the brain may have been changed during an impact which can then place stress on other brain structures, possibly resulting in damage (Gaetz, 2004).

Over the years, there have been several hypotheses attempting to account for the mechanisms of axonal injury (Strich, 1961; Omaya, 2002). More recent publications have suggested that mechanical strain, deformation of tissue due to an external application of a load (Nordin & Frankel, 2001), is the cause of axonal injury. More specifically, during an impact a sequence of events occurs, beginning with stress on the axon, causing it to stretch. This results in an influx of calcium (Ca^{2+}), sodium (Na^{+}), and chloride (Cl^{-}) and an efflux of potassium (K^{+}). It is now widely accepted that Ca^{2+}, which enters through the N-methyl-D-asparate receptor channel, is responsible for the axonal changes. The influx of Ca^{2+} results in the axon becoming dependent on oxygen and mitochondria dysfunction results. Further, due to the ionic imbalances, action potentials (depolarization events which are conducted across a nerve fiber) fail to generate and propagate. As the severity of injury increases, axonal stretching also increases, causing irreversible damage to the axons, as the Ca^{2+} influx is irreversible (Gaetz, 2004). This Ca^{2+} influx can also disrupt axonal cytoskeletal components (Hoshizaki & Brien, 2004).

Secondary TBIs occur as a response to the primary injury and are the body's normal physiological response to injury (Gaetz, 2004). Secondary injuries include tissue hypoxia (deprivation of oxygen in tissues), hemorrhages (loss of blood from damaged blood vessels), and cerebral edema (accumulation of fluid in brain tissue causing swelling). Of particular concern is tissue hypoxia, which occurs from decreased cerebral blood flow ultimately leading to neuronal cell death (Marieb, 2001).

Primary TBIs can be further categorized into focal and diffuse brain injuries. Focal injuries occur in a localized area and include cortical contusions (cortical tissue bleeding) as well as hemorrhages and hematomas (blood clots) in the extradural, subarachnoid, subdural, and intracerebral areas of the brain (Gaetz, 2004). Contusions usually occur in the frontal and temporal lobes of the brain which are responsible for attention, memory, planning, motivation, self-control, emotions, and affect (Nolan, 2005). Thus, often with contusions, symptoms reflecting irregularities in these functions are evident.

Head acceleration in the sagittal plane typically results in subdural hematomas (SDHs). SDHs generally occur under the dura matter, the outermost membrane of the brain and spinal cord (Marieb, 2001) and are normally venous, not arterial in nature. They are often caused by rupturing the parasagittal bridging veins (Goldsmith & Plunkett, 2004). Epidural hematomas (EDH) occur above the dura matter and are typically caused by arterial tearing. Once EDHs have been identified, they in themselves are usually easy to recover from. Ninety percent of the time, however, they are associated with skull fractures (Nolan, 2005). Signs of EDHs include temporary loss of consciousness, lucid periods lasting minutes to hours, and rapid neurological health deterioration (Nolan, 2005).

Further, frontal plane acceleration of the head often results in traumatic axonal injuries, which can be focal or diffuse (Goldsmith & Plunkett, 2004). Diffuse injuries occur over a larger area and include only cerebral concussions and diffuse axonal injuries (DAIs). These two types of injuries are associated with microscopic cellular changes of the cerebral tissue (Nolan, 2005). Concussions are usually induced mechanically by acceleration of the head. They are transient, temporary, neurological dysfunctions. They typically occur when the head is impacted causing it to accelerate, however, the motion of the brain lags behind that of the skull and, therefore, distortion of the brain occurs (Newman, Beusenberg, Shewchenko, Withnall & Fournier, 2005). Unlike moderate (classic) concussions, mild concussions can occur without loss of consciousness or memory. Recovery for moderate concussions can take anywhere from minutes to days and some people suffer post-concussion symptoms such as dizziness, headaches, fatigue, irritability, and memory problems. These may occur days or years after the initial injury (Nolan, 2005).

Brain injuries can also be coup or contrecoup injuries. Coup injuries result from the brain compressing against the skull at the site of impact. Contrecoup injuries occur as a result of the rebound effect of the brain after a coup injury, where the brain compresses at a point 180° from the point of impact (Nolan, 2005).

As well, the skull is a closed compartment with limited space and consists of blood, cerebral spinal fluid (CSF), and the brain. Therefore, when any one of these components increases in volume, the others must compensate and decrease in volume or a rise in intracranial pressure (ICP) occurs (Nolan, 2005). For example, when a SDH occurs some CSF is transported out of the brain to maintain a stable ICP. This process continues until there is no CSF left in the brain. At that point, the ICP increases which places stress on brain structures such as the brainstem, causing neurological dysfunction (Nolan, 2005).

2.2. Biomechanical Responses

The severity of any brain injury has been demonstrated to be directly related to the amount of energy transferred to the head during an impact (McIntosh & McCrory, 2000). All impacts are governed by one of the fundamental laws of physics, the conservation of energy, which states that the total amount of energy in a system remains constant, although it may change between forms, such as kinetic and potential energy. That is, energy cannot be created nor destroyed (Silberberg, 2000). Thus, when two objects collide and the kinetic energy of the object changes, that energy is either transferred elsewhere, for example by changing the velocity of the colliding objects, or is used to do work such as deforming something. The energy of deformation is often considered to be "absorbed."

It is the actual transfer of energy during an impact which causes the injury. When the head, or any other mass, *m*, is impacted, it moves at a given velocity, *v*, and possesses translational kinetic energy. This transfer of energy is represented by the formula: $KE = \frac{1}{2} mv^2$, where *KE* is the kinetic energy transferred to the head from the impact (J), *m* is the mass of the head (kg), and *v* is the velocity of the head (m/s) (Nolan, 2005).

The basic biomechanical injury mechanisms for all brain injuries are identical - forces are applied to the head directly or indirectly, via the neck and trunk, which results in acceleration of the head. Internal stresses within the brain are thereby created which may subsequently cause pathological injury such as neuronal or axonal damage. The resultant brain injury is dependent on the impact force magnitude, impact location, and the ensuing head and brain acceleration (McIntosh & McCrory, 2000).

More specifically, force is developed on the head during an impact because of the inertial resistance of body tissues and viscoelasticity of body structures, which delay the return of the deformation to its original form for some time period. Some researchers suggest both head deformation and acceleration resulting from an impact can cause injuries (Viano et al., 1989.) According to Newman, however, head injuries are not caused by acceleration (Newman, 2006). They are caused by the forces that develop during collision. During head impacts, the acceleration that the head undergoes and the injury that may be sustained are both responses to the impact. How these two responses might correlate to each other has been the subject of considerable research over the years and is essentially unknown.

Further, Varney and Roberts (1999) suggested that Newtonian formulas be applied to the description of forces on the head during acceleration. Newton's Second Law governs the relationship between the head's acceleration upon impact and the force imparted on the brain as a result (Goldsmith & Plunkett, 2004). This law is represented by the equation, $F=ma$, where F is the net force (N), m is the mass of head (kg), and a is the acceleration of head (g's), where 1 g is the acceleration due to gravity at sea level and is considered to be 9.81 m/s^2 (Robertson, 1997). It is common when describing head injury mechanisms or head protection devices to refer to the acceleration of the head in g's (Newman, 2002). It is important to remember that the head is not a rigid structure and can, in the process of the energy transfer, deform under the influence of a force. Therefore, the application of the theories provided in this section must be treated with caution when applying them to mechanisms of head injury, despite their wide use.

Serious brain injuries can be attributed to two primary types of forces imparted to the head on impact – translational (linear) and rotational acceleration. Translational simply implies that an object does not rotate. This movement is often referred to as linear. Therefore, if the vector of the impact force travels through the center of gravity of the head, the head will accelerate in a straight line, known as linear acceleration. Rotation means the angular orientation of an object changes (Newman, 2002). If the impact vector does not travel through the center of gravity, the head will experience both linear and rotational acceleration, the latter resulting in rotation of the head about the center of gravity (McLean & Anderson, 1997). Research has suggested that linear acceleration of the head can result in movement and distortion of the brain. When the surfaces of the brain, particularly the temporal and frontal lobes, impact the skull injuries may result. In addition, when the brain experiences high levels of rotational acceleration, a high risk of concussion and permanent diffuse brain damage exists (Mills, 2007).

In summary, the severity of any head injury is dependent on the amount of energy transferred to the brain. The formulas provided in the above section allow the stress and energy displacement on neurons, or head injury severity, to be closely approximated (Barth, Freeman, Broshek & Varney, 2001).

2.3. Impact Tolerance of the Brain

As long as the energy delivered to the tissue is below its tolerance limit, recovery from the deformation occurs. Thus, it is important to understand the relationship between an impact force and the resulting injury to determine these brain tolerance limits (Viano et al., 1989).

The criterion to develop injury tolerance levels has been traditionally based on head acceleration values. Most of this information has been derived from the Wayne State Tolerance Curve (WSTC), introduced by Lissner in 1960, which was developed from data collected by dropping embalmed cadaver heads onto flat surfaces (McElhaney, 1976; Gadd, 1966; Newman, 1993). This curve was subsequently reproduced by Gurdjian in 1962 and is shown in Figure 1.

The WSTC is the basis for most currently accepted head injury indices. It was the first attempt at demonstrating the relationship between peak acceleration levels and impulse durations necessary to cause a head injury. The curve indicates that short impacts of high acceleration can produce injury, while lower accelerations require longer impacts to produce injury. Thus, the WSTC suggests that impact durations should also be considered in addition to force/acceleration levels to determine injury threshold levels (Gadd, 1966).

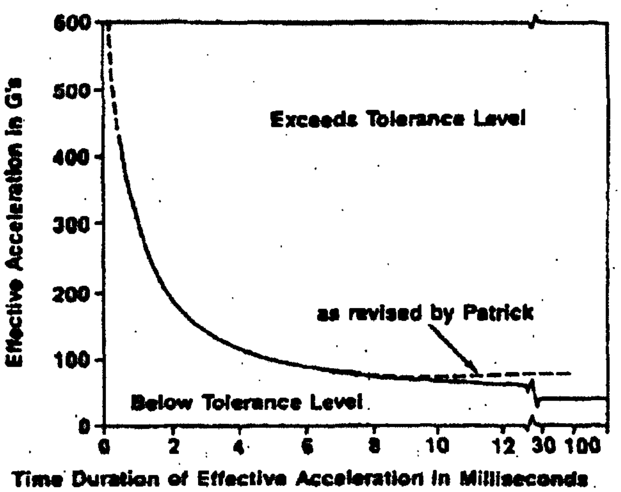

Figure 1. The present Wayne State Tolerance Curve illustrating the relationship between acceleration and time required to cause fracture in cadaver heads (McHenry, 2004).

There have been many criticisms of the WSTC since it originated. For instance, the data were first presented by a series of six data points and did not consider factors such as age, sex, weight, or size (Goldsmith & Plunkett, 2004). The original data only covered a time duration range of 1 to 6 ms and only addressed head injuries in which cadaver skulls were linearly fractured. Many people have also questioned the researchers' instrumentation techniques, lack of documentation regarding the scaling of animal data used in its extension to longer durations, and the uncertainty of definition of the acceleration levels.

Possibly the most important criticism of the WSTC is that there has yet to be any direct demonstrations of functional brain damage in an experiment in which biomechanical parameters, sufficient to determine a failure mechanism, in the tissue were measured. The assumption behind the WSTC is that the translational acceleration produces pressure gradients in the region of the brainstem that result in shear-strain-induced injury. The extension to the human brain remains to be verified (McHenry, 2004).

Overall, kinematic descriptions such as acceleration described by the WSTC, do not completely explain an impact event. Measuring linear acceleration, however, is fairly easy compared to quantifying levels of deformation. Existing tolerance levels which use acceleration do not consider the brain as being a deformable object and are, at best only "indirectly or incompletely related to brain injury" (Zhang et al., 2004, p.234).

The federal government has appointed private organizations to dictate the standards which base injury thresholds on peak acceleration, acceleration-time relationships, or acceleration history (Goldsmith & Plunkett, 2004). Further, injury threshold standards are based on linear acceleration values and do not consider angular acceleration patterns which result in different injuries. Although it is known that translational and rotational accelerations occur simultaneously in many head impacts, rotational accelerations are difficult to test and, therefore, have traditionally been excluded from tolerance limits (Goldsmith & Plunkett, 2004).

It is thought that accelerations as low as 80 g have the potential to cause mild TBIs (Newman et al., 1999; Pellman, Viano, Tucker, Casson & Waeckerle, 2003). Grade I concussions - concussions in which an individual may or may not lose consciousness - have also been shown by Patrick and Grime to occur at 80 g (1970). Other researchers have suggested that head accelerations of 220 g for 2 ms and 90 g for 9 ms should be the concussion thresholds (Zhang et al., 2004). Traditionally, concussions have not been considered dangerous and athletes suffering from concussions were encouraged to resume play; however, medical evidence has shown these injuries to be serious (Cantu, 2000).

After much deliberation, the tolerance limit for head acceleration in certifying helmets has been set at between 275 and 300 g (Hoshizaki & Brien, 2004). At this level of acceleration, however, skull fractures can occur. It could be argued that a more realistic tolerance limit should be as low as 150 g (McIntosh & McCrory, 2000).

Several methods have been devised to predict injury to the head based on the acceleration of the head upon impact and time. The Gadd Severity Index, $GSI = \int_T a(t)^{2.5} dt$, is based on the WSTC and is likely the most used injury assessment function in biomechanics (Gadd, 1966). It is defined as a measure of the severity of impact with respect to the immediate acceleration experienced by the head at impact. A GSI value of 1000 indicates there is approximately a 70% chance of a severe brain injury, calculated using the Abbreviated Injury Scale (AIS) (American Association for Automotive Medicine, 1980). The AIS is a standardized, anatomical scoring system designed to define the severity of injuries throughout the body. It was originally conceived to categorize and compare vehicular injuries but has been broadened to include almost all causes of injury (Gennarelli & Wodzin, 2006). In the AIS, injuries are assigned a value from one to six, one being a minor injury and six being a fatality (Kramer, Barancik & Thode, 1990).

The Head Injury Criterion (HIC) is a refinement of GSI and is used to determine acceptable levels of force transmitted to the brain. It is a derivative of head acceleration and is represented by the formula $HIC = [(1/_{t2}-t_1)\ {}_{t1}\int^{t2} a(t)dt]^{2.5}\ (t_2-t_1)$. HIC is based on the resultant translational acceleration. The acceptable threshold for injury to the brain for HIC was proposed to be 1000 by McIntosh and McCrory (2000). Thus, if the HIC is less than 1000, the injury would be completely reversible. There is evidence, however, that a HIC value of 1000 may be too high. Some researchers have suggested that a HIC of 1000 represents a 16% chance of a life threatening injury (Prasad & Mertz, 1985).

Thus, determining the actual forces which occur during an impact to the head, and the forces at which an injury occurs, is very difficult to calculate as head injuries can involve impacts and non-impacts (i.e. whiplash) and a combination of linear and angular accelerations. Nevertheless, it is important that the brain's best known tolerance levels, described by the above measures, are well understood so adequate head protection devices can be developed to protect the brain.

2.4. Head Protection and Helmet Design

2.4.1. Energy Management

Protective headgear has the potential to mitigate the extent, or number, of head injuries by reducing the mechanical loading placed on the head. Helmets do this by decreasing the acceleration of the head on impact by absorbing energy, thereby decreasing the magnitude of the impact force to the head and potential injurious stress to the brain and tissues. Helmets absorb energy through linear deformation, whereas an inverse relationship exists between the magnitude of the impacting force and the magnitude of linear deformation (McIntosh & McCrory, 2000).

Thus, the basic principle of head protection is to reduce the forces which can injure the head by absorbing some of the kinetic energy into itself, through deformation or destruction of something (i.e. padding in a helmet). If the moving head strikes an object, the object will absorb some of the kinetic energy of the head, and the forces generated in the impact will be less. The extent of this reduction is a function of how much deformation is achieved and the force required to deform the object.

An energy absorber is defined as “a system, that converts, totally or partially, kinetic energy into another form of energy” (Alghamdi, 2001, p.190), such as heat. It is important that energy attenuators, such as helmets, absorb the maximum amount of energy “irreversibly”, so that it does not store energy and rebound like a spring, to ensure that injury to the head is minimized (Alghamdi, 2001). The main function of any energy absorber is to control the deceleration pulse during an impact (Aljawi, Alghamdi, Abu-Mansour & Akyurt, 2005). Optimal energy absorbers spread the energy of the impact, or dissipation of kinetic energy, out over a long period of time, for instance 6 ms versus 1 ms, thereby reducing the peak spike of energy to the head and brain. That is, the energy attenuator temporarily stores some of the energy which evens out the force transmitted to the brain (Hwang & Kim, 2006). Ideally, the absorbers also reduce the maximum force transmitted to the brain by absorbing the energy in itself (Hwang & Kim, 2006). Thus, the more energy absorbed the less the head accelerates and as a result the force transmitted to the brain is also decreased as a function of the equation $F=MA$.

Both time and distance over which changes in velocity also occur influence the outcome. The cushioning effect of helmets increases the distance of head deceleration and reduces peak forces associated with injuries. Helmets also increase the surface area across which a force is absorbed. This is evident in another Newtonian formula: $p=F/a$, where p is the pressure (Pa), F is the force applied (N), and a is the acceleration (g). By distributing the applied force to the helmet, the pressure exerted on the head is actually decreased as a function of the area of the helmet (Varney & Roberts, 1999).

An ideal energy absorber would therefore have the impact force rise to a predetermined critical force level instantaneously, maintain that load for the duration of the impact, and then instantaneously drop to zero at the end. The force-time curve, a visual representation of force progression with respect to time, would appear to be a square wave or shock pulse as shown below (Yu-Hallada, Kuczynski & Weierstall, 1998).

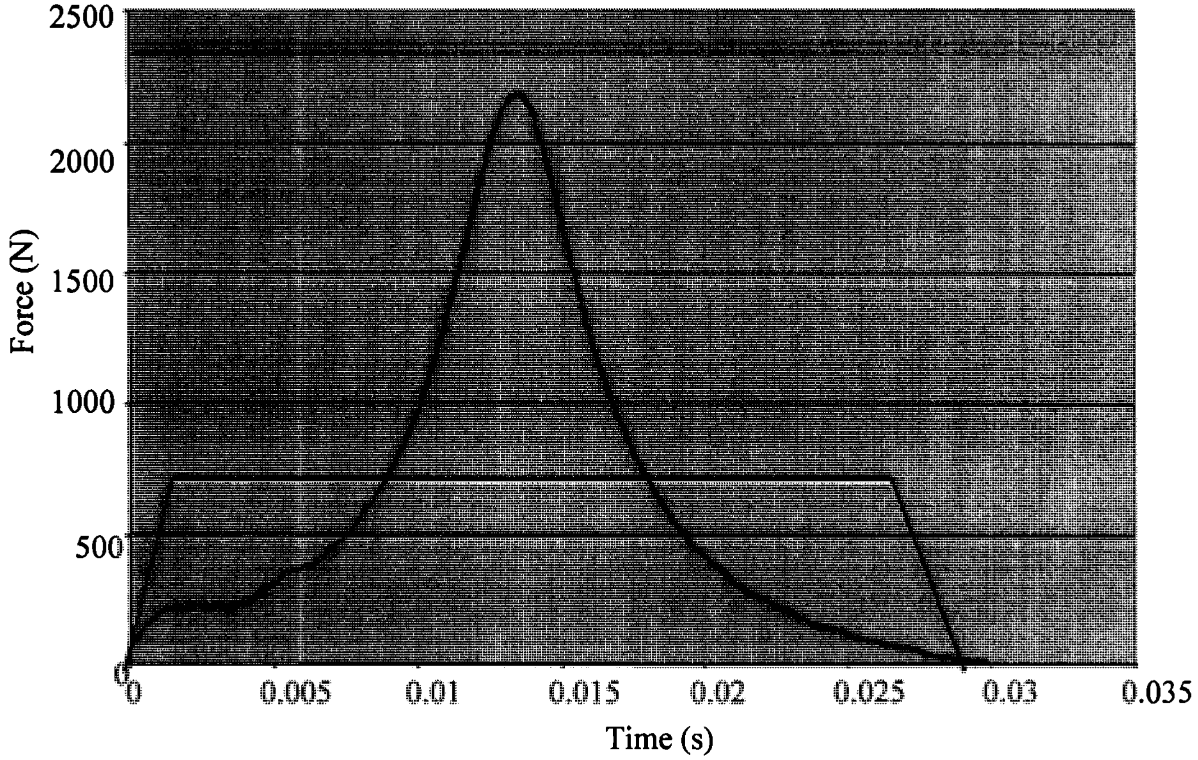

Figure 2. Target force-time curve for any given shock absorber (square shock pulse) shown in red and force-time curve for a classic energy absorber used in helmet shown in blue.

The goal of any energy absorption system used in a helmet is to therefore achieve the theoretical square force trace. To accomplish this, Newman (2002) suggests that helmets compress all the available energy absorption material to the fullest extent. He advises 80% compression is a practical upper limit before the material bottoms out. He also recommends that the velocity change be minimized (i.e. to eliminate rebound), onset rate maximized, constant acceleration maintained throughout the impact, and the finishing rate maximized.

2.4.2. Head Protection Design

Modern helmet designs have traditionally focused on merely decreasing the peak forces transmitted to the brain. Currently, typical helmets consist of (a) an outer shell, (b) an energy-absorbing liner, (c) a soft foam or padding for comfort, and (d) a chinstrap (Liu, Chang, Fan & Hsu, 2003). Consequently, impact energy can be absorbed by the shell, liner, or padding in a helmet, enabling the impacting and impacted surfaces to deform, extending the impact duration and reducing its severity (Viano et al., 1989).

The shells generally consist of a plastic material such as polycarbonate or polyethylene. Polycarbonate is durable and capable of sustaining several impacts. Nevertheless, it can crack under high-energy stress. Polyethylene rarely fractures; however, it is easily distorted. Thus, the performance characteristics of the shell depend on the material used (Hoshizaki & Brien, 2004). Further, the geometry of the shell is also implicated in energy absorption. The larger the area of impact, the more distributed the impact is, which reduces the amount of stress at a given area in the brain. Hoshizaki and Brien indicated that shells have the capability of absorbing up to 18% of the total energy absorbed by the helmet on impact (2004).

Liners are usually the primary impact absorbing material in a helmet (Mills & Gilchrist, 1991). They typically consist of expanded polystyrene (EPS), expanded polyethylene (EPE), expanded polypropylene (EPP), or vinyl nitrile (VN) foam. EPS is generally used in single impact (crash) helmets. It consists of polystyrene "beads" which are formed in a mold and then injected with steam melting the beads together to form the liner (Hoshizaki and Brien, 2004). During an impact, EPS compresses while it absorbs energy crushing the beads. It is, however, inexpensive, light, and effective, making it appealing to use. EPP and EPE are similar to EPS however, the beads are not destroyed upon impact. Rather, the foam is able to regain its original shape without severe damage. The foam does, however, degrade over time and does not absorb energy as effectively. VN is similar to EPP and EPE in that they are able to recover their shape after an impact and also degrade with repeated use (Spyrou & Hoshizaki, 2001). Consequently, EPS is often used for single impacts such as in helmets designed for bicycling, whereas EPP, EPE, and VN are used in helmets designed to sustain multiple impacts such as in ice hockey or American football helmets (Hoshizaki & Brien, 2004).

With the appropriate choice of materials, helmet manufacturers are able to decrease HIC and GSI values (Camacho, Nightingdale & Myers, 2001). Manufacturers have a particularly difficult decision to make when considering helmet design. The composition of the helmet requires a balance of energy attenuation performance as well as stiffness. There is concern over using materials which are very stiff, as a substantial amount of energy may be transmitted to the brain during low to medium velocity impacts since the foam would not deform easily and thereby absorb energy (Newman, 1993).

In general, helmets which are designed to manage high-energy impacts (40 to 60 J) are not nearly as effective at preventing brain injuries during low to medium energy impacts (Hoshizaki & Brien, 2004). The following figure illustrates this concept:

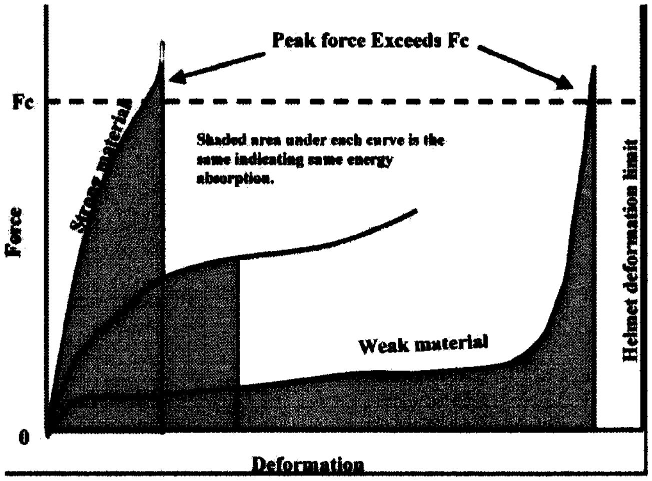

Figure 3. Theoretical graph showing strong, medium, and weak impact material performance (Newman, 1993).

Figure 3 illustrates strong, stiff material exceeds the force limit very quickly. The weak material did not absorb much energy by comparison to the strong material before it bottomed out, transmitting a substantial amount of energy. The medium material absorbed a substantial amount of force without passing the force limit. Thus, this medium material would be optimal to use in a helmet. The difficulty lies in choosing materials capable of such performance.

As foam thickness increases, the potential for work to be performed through foam deformation also increases, thereby increasing the energy attenuation of the impact (McIntosh, McCrory & Finch, 2004). Helmet designers have manufactured soft foams thick enough to manage low and medium velocity impacts. However, when trying to protect against high velocity impacts, manufacturers face a difficulty, since they are unable to continue increasing the foam thickness as they are restricted by the helmet size. The following figure (4) depicts the relationship between the thicknesses of foams required to adequately absorb energy on impacts at various velocities (Newman, 1993).

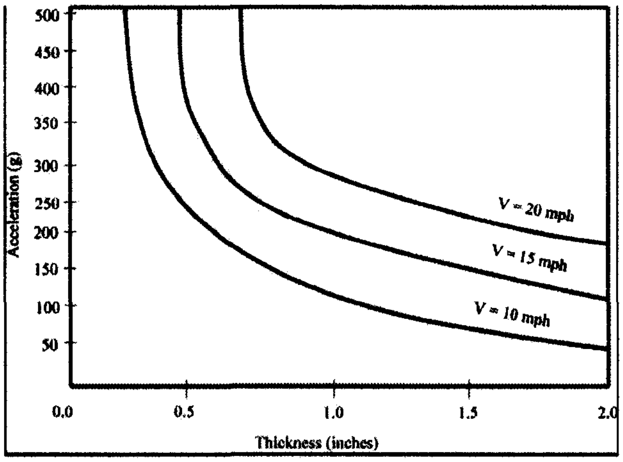

Figure 4. Graph showing minimum foam thicknesses required to absorb head impacts at 10, 15, and 20 miles per hour (Newman, 1993).

According to Newman (1993), if the head is traveling at 10 mph on impact, a helmet liner of 1.5" could limit acceleration of the head to approximately 100 g. Thus, it is hard for designers to create a helmet which is stiff enough to absorb energy in high velocity impacts without bottoming out but deformable enough to absorb energy at low and medium velocities and which has enough foam to absorb low and medium velocity impacts but is thin enough to fit inside the helmet properly.

2.5. Helmet Assessment

The GSI is often used to provide biomechanists with a standard to assess the safety of sport head protection devices. It predicts a helmet's ability to reduce the force transmitted to the head upon impact under controlled conditions and, therefore, protect the brain. Current helmets on the market do not protect against concussion, hence the high number of athletes who sustain concussions while wearing a helmet. For most helmets to pass current standards, the peak GSI may not exceed 1200.

In regards to linear acceleration, the best performing helmets protect the brain from accelerating over 120 to 130 g and as stated before, concussions can occur at 80 g. In general, however, present helmets protect the head from accelerating over 200 g (Hoshizaki & Brien, 2004).

Although there has been an increase in the promotion of helmet use which has proven benefits, the standards that govern helmet design have not received the same amount of attention. The scientific knowledge behind the mechanisms of brain injury during impacts and the relationship between impact testing and resultant injuries has continued to advance, yet changes to the standards have not been adequate. Despite the dramatic increase in the head protection market, the level of protection offered by helmets has not increased. Unless helmet standards change, helmet performance is unlikely to improve (Hoshizaki & Brien, 2004).

Thus, if injury thresholds adequately reflected forces which cause injuries, the performance of head protection devices would be seen to be even poorer than they currently are. Nevertheless, researchers, clinicians, and athletes alike are all interested in having helmets protect better than current designs, which would facilitate the reduction of injury thresholds used to certify helmets protecting people far better from TBIs.

The development of better methods capable of absorbing a large amount of the impacting force without compromising the size and fit of the helmet is not an easy feat. Thus, it is important that head protection researchers consider incorporating energy absorbers used in other applications into helmet designs.

2.6. Energy Absorbers

One system used as an energy absorber in other industries is enclosed air. The use of enclosed air as an energy absorber is not a new concept; however, it has not been commonly used in helmets. Air chamber type systems have been used by sporting manufacturers for the Cascade helmet, Nike Air products, and Riddell air impact system, however, little literature exists on these products. Air chamber type systems have also been used in energy attenuation applications including a) a wrist guard, b) a novel air cushioning material, and c) corrugated fibreboard.

2.6.1. Wrist Guard

A very recent study examined the shock attenuation capability of several devices which could be incorporated in a wrist guard used in sport (Kim, Alian, Morris & Lee, 2006). The objective of the study was to enhance the shock absorption function of the wrist guard. The researchers evaluated a bare-hand, a generic-brand wrist guard, a Sorbothane glove, *an air cell*, and an air bladder using a free-fall device which they constructed using a mechanical surrogate to imitate a falling impact (see Appendix A for diagram). The researchers dropped the mechanical arm on each of the devices to determine the energy absorbed by each material, obtained from force plate readings.

There does not appear to have been any other researchers which have used this type of free falling device, thus, the reproducibility of their results in another lab is essentially unknown. The researchers did not refer to the validity and reliability of their study or their equipment; however, this is a new method which had not previously been reported in the literature. The authors used a force plate to measure the force transmitted by the devices, however they did not report their validation or calibration procedures. They repeated each trial three times at four different heights.

In material testing, it is common that an impactor is dropped on the material being examined to simulate a real life impact (Harte, Fleck & Ashby, 2000; Di Landro, Sala & Olivieri, 2002). In addition, when the energy attenuation of various foam materials is tested, several drop heights are typically used (Harte et al., 2000; Di Landro et al., 2002). These researchers varied the drop heights of the mechanical arm on the energy attenuating devices, thereby altering impact velocities. One limitation of this drop system, however, is that it does not consider the effects of the shoulder and the rest of the body when falling.

The researchers determined that of the five conditions tested, the air bladder and air cell were the most effective at absorbing energy. The peak impact force, peak time, and peak accelerations were best for the air bladder followed by the air cell (see Figure 5).

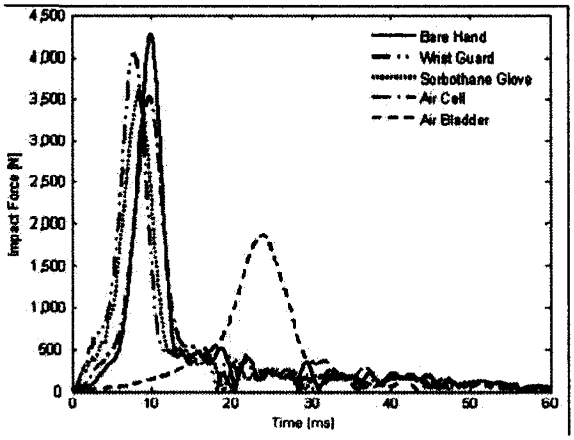

Figure 5. Shock attenuation profiles from a dropping distance of 51 cm (Kim et al., 2006).

The air cell appeared to be a circular chamber, approximately 1" thick, filled with air. The authors provided a photograph of the air cell, however, they did not describe its composition. The air bladder consisted of a manual air pump and multilayer air chambers. The researchers did not attempt to explain the differences observed between the energy absorbers. They simply stated their results and noted that more research is required. The authors did, however, state that the designs of the air cell and air bladder were not optimized for falling impacts of human beings. They were interested in only determining the possible shock absorbing characteristics. Thus, they indicated that further research needs to be done to optimize their geometric designs for human use. Consequently, this study identified air chambers as a potentially effective way to manage impact energy.

2.6.2. Novel Air Cushioning Material

The packaging industry has also used somewhat similar technology to protect parcels from impacts during the shipping process. A Japanese research team developed a packaging material consisting of enclosed air and foam, described as a novel air cushioning material (NACM) (Sasaki, Saito & Abe, 1999). In their brief, published study on the NACM, the authors did not state a purpose for their research; they merely described the NACM (see Appendix B for diagram) and a few of its energy absorbing characteristics. They constructed the material using a nylon cloth for the outer surface which enclosed an air and a foam chamber, which were also surrounded by a sheet of polyethylene and nylon films. The air chamber was a simple air bag, while the other chamber contained urethane foam. The system worked when outside pressure compressed the air filled chamber. As the compression continued, the urethane foam was compressed and the air escaped through a perforated surface in the foam liner.

The researchers used a drop test rig (see Appendix C for diagram) to examine the NACM's energy absorbing ability, similar to most others used in the packaging industry. The equipment, however, is not standard in the field (Mills & Masso-Moreu, 2005; Naganathan, He & Kirkpatrick, 1999). They did not refer to the reliability or validity of their research. In fact, the researchers inserted a diagram of their drop tester but did not describe the apparatus or how they collected the acceleration data. They tested the NACM at three different drop heights (20 cm, 45 cm, 60 cm), with three NACM thicknesses (40 mm, 70 mm, 100 mm) of the test samples, 30 times each. They performed 30 tests, to establish the reliability of the data in the study. The researchers determined that the NACM had stable energy absorbing properties (not much difference between the 1st and 30th drops), at the highest drop height. Hence, the design of the material appeared to manage energy well and could be used in other applications.

2.6.3. Corrugated Fibreboard

A similar energy absorbing system has also been employed in corrugated fibreboard, a commonly used packaging material (see Appendix C for photograph). The wave-shaped cardboard material contains air spaces throughout which aid in absorbing energy during impacts. One study, which looked at the structure of the material, aimed to "establish whether the shock absorbing properties of corrugated fibreboard are indeed dependent on cushion size for impacts under static loading and to determine whether this could in part be explained by the effect of air enclosed within the flutes" (Naganathan et al., 1999, p.82).

The researchers used a Lansmont cushion drop tester, to examine the fibreboard's energy attenuation capacity, commonly used in the packaging material industry (Mills & Masso-Moreu, 2005; Naganathan et al., 1999). Again, the authors did not address issues of validity and reliability, although this is a commonly used drop test system. They did not refer to the design of the drop tester or the equipment used. They tested the materials from 30 and 60 cm, typically the impact drop heights packaging materials are designed to withstand (Naganathan et al., 1999). Each cushion was tested twice and each trial repeated seven times.

The authors tested seven fibreboard sizes ranging from 47 mm by 47 mm to 120 mm by 120 mm. They found that a difference existed in the shock absorbing characteristics of larger and smaller cushion sizes because of the ease with which air was able to flow out of the material during an impact. The largest fibreboard had a higher resistance to air flow out of the material, due to the greater distance the air needed to travel from the centre of the material to escape the material as well as a smaller relative escape area, when compared to the smaller fibreboards. The greater resistance to the air escaping from the larger cushion during compression, led to a higher internal pressure within the larger chamber and thus, a greater proportion of impact energy was absorbed. The researchers determined that cushion size was significant. As the cushion size was reduced, the shock transmitted values increased steadily and then catastrophically when the cushion size reached a certain size. On the first drop, the smallest cushion (47 mm by 47 mm) transmitted 137% more energy than the largest cushion (120 mm by 120 mm). On the second drop, the effect of the cushion size was less pronounced.

The researchers also used polyethylene foam as a control, to determine if the amount of air enclosed in the fibreboard actually made a difference. Since polyethylene is a closed cell, no difference was expected in shock absorption values of various sizes with constant thicknesses of 1". This supported the hypothesis that the amount of air enclosed in the fibreboard was related to the shock absorption values of the materials.

The authors also determined that by taping the ends of the fibreboard, allowing only a small passage of air, the material was able to absorb a significantly greater amount of energy at high impact speeds (50 mm/s and 400 mm/s) compared to unsealed fibreboard. Thus, the taped end reduced the escape area for the air, increasing the air velocity out of the material. According to Bernoulli's equation, a greater air velocity is directly related to a pressure build-up near the centre of the cushion (Simmonds, 1996). That is, pressure is reduced as air flow velocity increases. Thus, the sealed cushions had a build up of pressure which only became significant when the chamber was compressed enough to collapse, forcing the air out. Therefore, the pressure resulted in an increase in energy absorbed by the cushion without increasing the maximum force transmitted, causing the shock pulse to become squarer. The squarer shock pulse resulted from an increase in the amount of impact energy absorbed before bottoming out. Thus, the pressure from the taped ends resulted in the cushion absorbing a substantial amount of energy when impacted reducing the force transmitted, until the fibreboard bottomed out, causing the pulse to catastrophically drop. Nevertheless, at a very slow impact velocity (1 mm/s) there was no difference in the sealed and unsealed energy absorption values. This can be explained by the venting system not being activated at very low velocities since there is not enough compression and pressure build-up in the material.

Thus, the researchers determined that the air enclosed within the material greatly affected its cushioning function. This study indicates that air in a closed cell absorbs energy much better than an open cell. It also indicates that there is an optimal chamber size to manage energy. Further, it provides evidence that a small vent within the closed cell may help to manage the energy. The above three applications illustrate the potential of an enclosed air chamber as an energy absorber. Nevertheless, air chamber type systems have yet to be incorporated into marketed helmets.

2.7. New Method

There is a need in the head protection industry for improved energy absorption systems within helmets without the disadvantages of current helmet designs. An energy management system is needed, which broadens the range of impact energies over which energy absorption is optimal, to reduce the risk of both mild and severe head injuries. Ultimately, the challenge of helmet design is to achieve the theoretical square force-time trace across a wide range of impact energies, reducing overall peak forces transmitted to the brain and increasing the duration of impact. This has yet to be accomplished by contemporary headgear and thus current designs must be modified if increasing protection is the goal.

Air chambers could replace or be used in conjunction with the foam currently used in helmets (see Figure 6 and Appendix E for more detailed drawings and pictures).

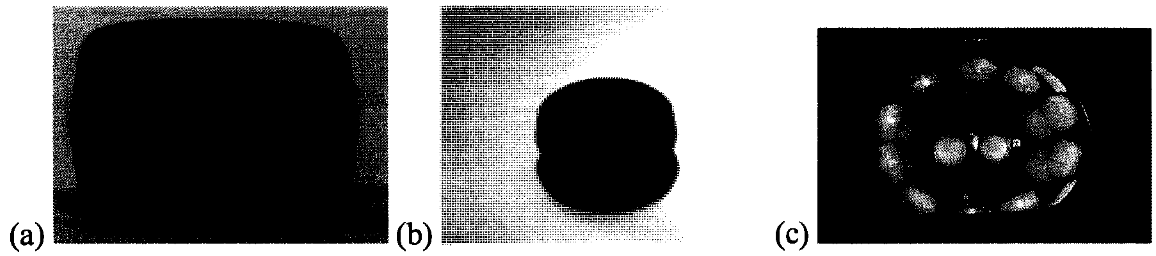

Figure 6. (a) Photograph of a single air chamber used in the present study. (b) Photograph of newly designed chamber. (c) Photograph of an array of air chambers in a helmet.

The chambers are involved in the management of energy during an impact. They are intended to improve helmet performance by reducing the magnitude of the impact force to the head, the head's acceleration, and resultant injury. Essentially, the chambers are used for energy management as foam is in contemporary helmets. Like foam, the chambers absorb energy by deforming the structure and material both elastically and plastically, thereby decreasing the distance of head deceleration. They also reduce the force transmitted to the head by trying to convert some of the impact energy to heat, slowing the stopping process and increasing the duration of the impact.

A recent study by Gimbel and Hoshizaki (2008) compared air chambers (TPU 45D and TPU 90A, 2 mm vent - chamber properties described in next section) to VN (600, 602, and 740). All samples were impacted from 20, 40, and 60 cm using a free drop rig containing a 5.02 kg flat impactor (see Appendix D). Researchers indicated across all drop heights, air chambers resulted in significantly less peak linear acceleration than VN, with the exception of between TPU 45D and VN 740, and VN 600 and TPU 90A. This can be explained by the relative stiffness of the materials, as VN 740 and TPU 45D are considered harder materials, while VN 600 and TPU 90A are both softer materials. Overall, compared to VN, chambers were able to manage the impact energy approximately 30 to 40% better, throughout a wider range of drop heights.

There are several properties of these air chambers which can change the way they absorb energy and can be altered to optimize their function. The chambers, which measure approximately 5.2 cm in diameter and 2.6 cm in height, essentially consist of four engineering elements which influence their ability to manage impact energy efficiently: i) rigid wall cylinder (geometry), ii) air filled chamber (ride down allowance), iii) elastic/plastic material (stiffness and thickness), and iv) controlled vent.

2.7.1. Rigid Wall Cylinder

Although there have yet to be any published studies on these chambers, research on the general design of collapsible impact energy absorbers has confirmed that a circular shape of the chambers, such as the above chambers, optimizes their energy absorbing properties (Abdul-Latif & Nesnas, 2003; Singace, El-Sobky & Petsios, 2001). Alghamdi stated that "The circular tube proves to be a popular energy absorber because it provides a reasonably constant operating force, which is, in some applications, a prime characteristic of the energy absorber" (2001, p.202). Circular tubes and conical structures have been used in several structures in which energy absorption is crucial such as to protect ships when contacting wharves, in automobile bumpers, and in aircraft landing technology (Singace et al., 2001).

Thin-walled structures with symmetrical cross sections such as the dynamic air chambers, can collapse in the form of a concertina or diamond mode (Aljawi et al., 2005). Concertina collapse occurs when the wall collapse is axisymmetric, symmetrical about an axis, and sequential folding occurs, beginning at one end of the cylinder or tube. The diamond mode of collapse involves non-axisymmetric collapse and sequential folding with a change in the cross-section shape of the tube (Andrews, England & Ghani, 1983).

When cylinders are compressed axially, the sides bulge out, as the material, although strong enough to not crack or fail, is not strong enough to support the load without change. As a result, the material is forced out laterally. Therefore, axial compression at a high enough force can create high internal pressures on the wall. This has the potential to induce extensive local bending near the bottom edge of the structure which can lead to the cylinder "bottoming out."

As chambers are impacted, they collapse in concertia mode, shown in Figure 7, and appear as a bellow. The chambers have hinges, similar to the diagram below (points A, B, C), where work is done to bend the structure (Alexander, 1968). As well, work is done to stretch the material between the plastic hinges when impacted. This increases the energy absorption capability of the chambers. Abramowicz (2003) indicated that in thin-walled structures plastic deformations are localized at the hinges, where most of the plastic deformation takes place. Plastic deformation has been commonly used in energy absorbing applications (Abdul-Latif & Nesnas, 2003), allowing the conversion of kinetic energy into deformation in thin collapsible structures, such as dynamic air chambers (Aljawi et al., 2005). (See section 2.7.3 for full discussion).

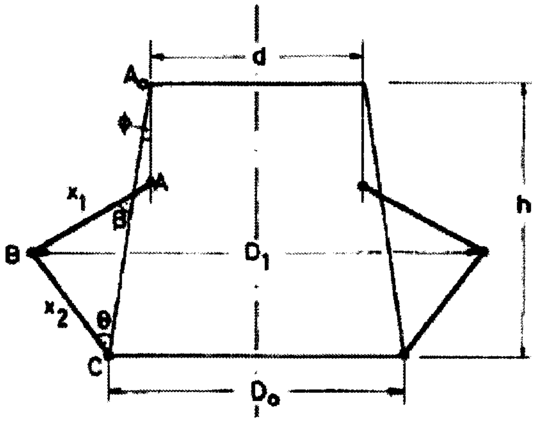

Figure 7. Diagram illustrating deformation mode for an extensible, collapsible, thin-walled structure, forming external convolutions similar to the chamber structure (Mamalis, Manolakos, Saigal, Viegelahn & Johnson, 1986).

2.7.2. Air Filled Chamber

Further, compressed air is an excellent energy absorber as it has a high energy-storage capacity for its weight and "greater isolation efficiency to high-frequency loading" (Kim et al., 2006, p.638). In relation to the studies described in section VII, the dynamic air chambers appear to be very similar to the air filled cell used in the wrist guard. The distinguishing characteristic, however, is that the dynamic air chambers are specific to the energy attenuation requirements of the brain and head. As well, the NACM resembles the combination of the dynamic air chambers and foam used together.

2.7.3. Thermoplastic Polyurethane Material

2.7.3.1. Material Composition

Another impact engineering opportunity which can be altered is the material of the chamber – its elastic/plastic composition. The chambers are made of thermoplastic polyurethane (TPU), a thermoplastic elastomer made of BASF Elastollan® S series, polyester type, which can be adapted for several applications as it can provide many different physical properties. TPU is often considered a soft plastic or hard rubber, however, Nardo (1987) has suggested it is neither. Rather, it combines the best engineering qualities from both and adopts its own identity.

2.7.3.1.1. Chemistry and Properties

Elastomers, often used interchangeably with rubbers, consist of an elastic component ("elasto") as well as a polymer backbone ("omers"). Typically, they are often used for seals, adhesives, and molded flexible parts. Thermoplastic elastomers are a class of copolymers and consist of a physical mix of polymers, usually plastic and rubber. Typically, urethane elastomers appear to be a solid rubber and are not "foam-like" (Bank, Sardanopoli, Henri & Sayigh, 1971). Thermoplastics are relatively easy to manufacture in contrast to thermosets (most elastomers are thermoset). The difference between thermoplastic elastomers and thermoset elastomers is the type of crosslinking between bonds within their structures. Crosslinking is a critical factor which contributes to the high elastic properties in a material. The crosslink in thermoset elastomers is a covalent bond, whereas the crosslink in thermoplastic elastomers is a weaker dipole or hydrogen bond.

Polyurethanes are polymers consisting of a chain of organic units joined by urethane links. They are in a class of compounds known as reaction polymers and are formed by reacting an isocyanate group, –N=C=O, with a hydroxyl (alcohol) group, -OH. That is, polyurethanes are produced by the polyaddition reaction of a polyisocyanate with a polyalcohol (polyol) in the presence of a catalyst and other additives. The reaction product is a polymer containing the urethane linkage, -RNHCOOR'-, where R is the nucleus of a diisocyanate (Ehrlich, Farrissey, Goldwasser, Oertel & Onder, 1984).

TPU has a linearly segmented block copolymer structure, composed of hard and soft components. Within TPU, the hard segment can be aromatic or aliphatic, both of which consist of isocyanates. When these isocyanates combine with short-chain diols, or low molecular weight diol, they become hard segments. Typically, the hard portion is aromatic, however, if color and clarity retention in sunlight is required, aliphatic hard segments are used. The soft segments of TPU can be a polyether or polyester, depending on the application. For instance, polyether TPU's are usually used in wet environmental applications, while oil, fuel, and solvent resistance require polyester based TPU, the type used in the chambers. The soft segments are generated by the reaction of a diisocyanate and a high molecular weight resin. The hard and soft segments' molecular weights, ratios, and chemical types can be altered for even greater usage (Nardo, 1987).

Thus, the main polyurethane production reaction is between a diisocyanate (aromatic and aliphatic types exist) and a polyol, typically a polypropylene glycol or polyester polyol, in the presence of a catalyst and materials for controlling the cell structure (Zhang et al., 2008).

Polyurethane can be made in a variety of densities and hardnesses by varying the type of monomer(s) used and adding other substances to modify their characteristics, notably density, or enhance their performance. Other additives can be used to improve the fire performance, stability in difficult chemical environments and other properties of the polyurethane products. Injection moldable TPU elastometers generally range in hardness from durometers 70A to 80D (Ehrlich, Farrissey, Goldwasser, Oertel & Onder, 1984). (See section 3.3.1.3. for a complete description on material stiffness measures).

Among elastomers, polyurethanes are extremely resistant to abrasions, their flexibility in low temperature environments is outstanding, their oil resistance is excellent, and they are considered one of the best load bearing materials. Polyurethane thermoplastics are characterized by high tensile and tear strength, excellent abrasion resistance, resistance to fuels, oils, ozone, and oxygen, high elasticity and resilience, high load bearing capacity and hardness, high impact resistance and vibration dampening properties, and excellent low temperature properties (Nardo, 1987). TPU has been stated to bridge the gap between plastics and rubbers (see Figure 7).

The following table illustrates the properties of BASF, Elastollan® polyester type polyurethane elastomers. The TPU 45D chambers are made by mixing TPU 90A with a shore D TPU. Thus, TPU 90A and 64D properties are listed below.

Property	90A	64D
Density	1.23 g/cc	1.25 g/cc
Hardness, Shore A	92	
Hardness, Shore D	41	64.0
Tensile Strength, Ultimate	37 MPa	39.0 MPa
Tensile Strength, Yield (100% elongation)	11 MPa	27.0 MPa
Tensile Strength, Yield (300% elongation)	20 MPa	37.0 MPa
Elongation at Break	540%	380 %
Tear Strength	125 kN/m	220 kN/m
Taber Abrasion, mg/1000 Cycles	25	50.0
Tensile Set (at break)	55%	135 %

Table 1. BASF, Elastollan® TPU material properties (Matweb, 2008).

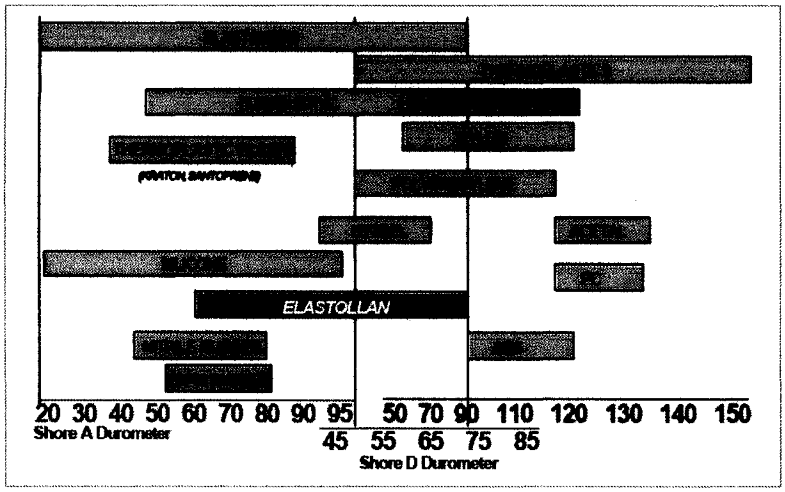

Figure 8. Hardness comparison of Elastollan® TPU and other materials (BASF, 2008a).

The chambers are manufactured using injection molding, a process in which plastic granules are softened and forced under high pressures into a cold mold through small orifices. Pressure on the plastic is then maintained once the injection is complete. The following figure illustrates an example of injection molding equipment.

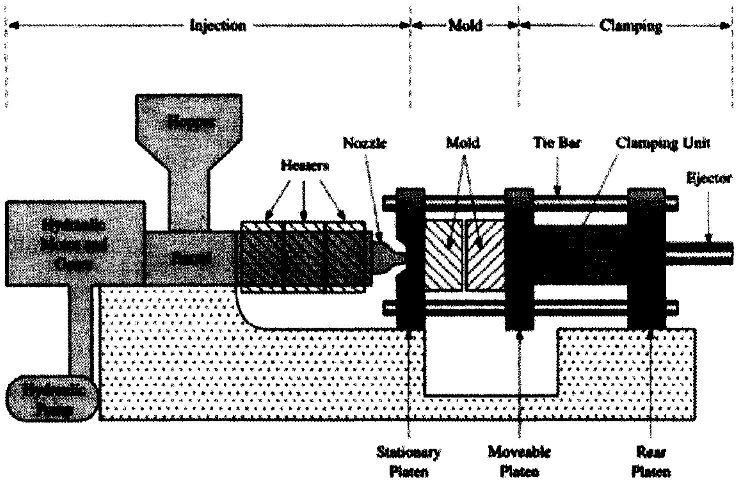

Figure 9. Injection molding machine illustrating the main three functional units (injection, mold, clamping) (Penn Plastics Inc, 1999).

To ensure consistency and quality of TPU, manufacturing temperatures, speeds, and pressures are strictly controlled throughout the process. The following table lists Elastollan® injection molding conditions for TPU 90A and 64D.

Elastollan® Grade Hardness	Barrel			Nozzle	Melt
	Feed	Compression	Metering		
	^{0}C (^{0}F)	^{0}C (^{0}F)	^{0}C (^{0}F)	^{0}C (^{0}F)	^{0}C (^{0}F)
TPU 90A	190 (380)	205 (400)	210 (415)	215 (420)	200-215 (390-420)
TPU 64D	210 (410)	220 (425)	230 (445)	230 (450)	210-225 (410-440)

Table 2. Elastollan® injection molding conditions guidelines for TPU 90A and TPU 64D (BASF, 2008b).

2.7.3.1.2. Applications

One of the first major applications of TPU was top lifts for women's shoe heels, which still consist of TPU to this day. This application demonstrates the materials' resistance to abrasion, load bearing capacity, and resistance to environmental conditions. Shopping cart wheel treads also consist of TPU, indicating their excellent abrasion, grease, and oil resistance, as well as their high load bearing characteristics. Screens for coal, iron ore, phosphates, and gravel among other substances, are also often made of TPU. In fact, screens containing TPU have been shown to outlast braided wire screens by a factor of five to one up to fifty to one (Nardo, 1987). TPU is also used for cow tags, which must last a minimum of ten years in varying environmental conditions. Further, because of their high tensile strength they are used as liners in fire hoses as opposed to rubber, and as insulation for covered wire. As well, TPU has been used extensively in the automotive industry for various purposes to absorb the forces encountered in automobile operation. TPU's are now widely used in flexible and rigid foams, durable elastomers and high performance adhesives and sealants, fibers, seals, gaskets, carpet underlay, and hard plastic parts (Nardo, 1987).

2.7.3.2. Mechanical Behaviour

The chambers require a precise balance of elastic/plastic (soft/hard) elements to effectively manage the impact energy as they collapse. Thermoplastics have moderate elastic deformation range and are able to return to its original shape once a load is removed. A structural component is said to behave elastically if its change in shape, or deformation, upon load/unloading is reversible. When the load is removed, the material returns to its original, undeformed configuration. On the contrary, if the material does not return to its initial undeformed state after unloading it is said to behave plastically. In engineering, this transition from elastic to plastic deformation is called yielding. Thus, the elastic range ends at a material's yield strength. Elastic deformation is an approximation and if a material exhibits both elastic and plastic deformation it is said to have undergone elasto-plastic deformation (Atkins & Mai, 1985).

Soft thermoplastics and ductile materials have large plastic deformation ranges whereas hard thermoplastics and brittle materials have minimal plastic deformation ranges. An example of a large plastic deformation range is wet chewing gum. Force-time curves of ductile and brittle and ductile materials are shown in Figure 10.

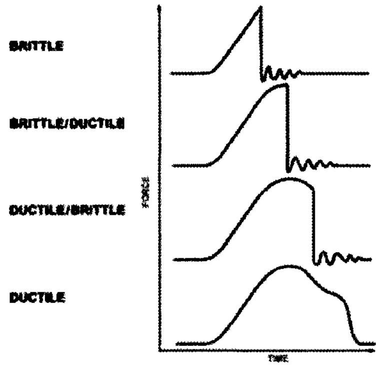

Figure 10. Brittle and ductile failure force-time curves (Greene, 2005).

A material which undergoes plastic deformation, would have already undergone elastic deformation and thus, the object will at least return partially to its original shape if the load is removed without fracturing the material. Fracturing, or breaking, occurs after the material has reached the end of the elastic, and then plastic, deformation ranges (Atkins & Mai, 1985). At this point forces accumulate until they are sufficient to cause a fracture. In some instances, plastic deformation is not necessary for material failure. After repeated deformations, fracturing can occur without plastic deformation in between, depending on the material, structure and how close to the elastic limit the material was subjected to upon deformation. All materials will eventually fracture if sufficient forces are applied. On a microscopic level, fracturing begins with crack initiation and follows with crack propagation in which the fracture progressively continues as a result of continuous applied stress. Failure occurs when the material cannot withstand the applied stress.

The total area under a force-time curve gives the impact energy for the system. This curve can be divided into two regions, as seen in Figure 11.

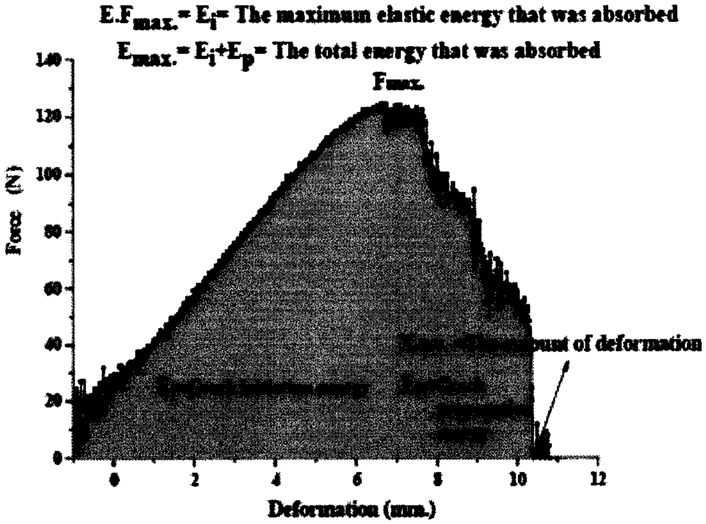

Figure 11. Force-deformation curve of a thermoplastic matrix composite under dynamic impact loading (Coban, Bora, Sinmazcelik, Curgrul & Gunay, 2008).

These regions give the energies of crack initiation and crack propagation. The first region, the crack initiation region, extends up to the peak force in the force-time curve. The second region, crack propagation, starts at the peak force and ends at the material fracture.

The following figure illustrates polystyrene impacted from various angles using a chapy pendulum hammer.

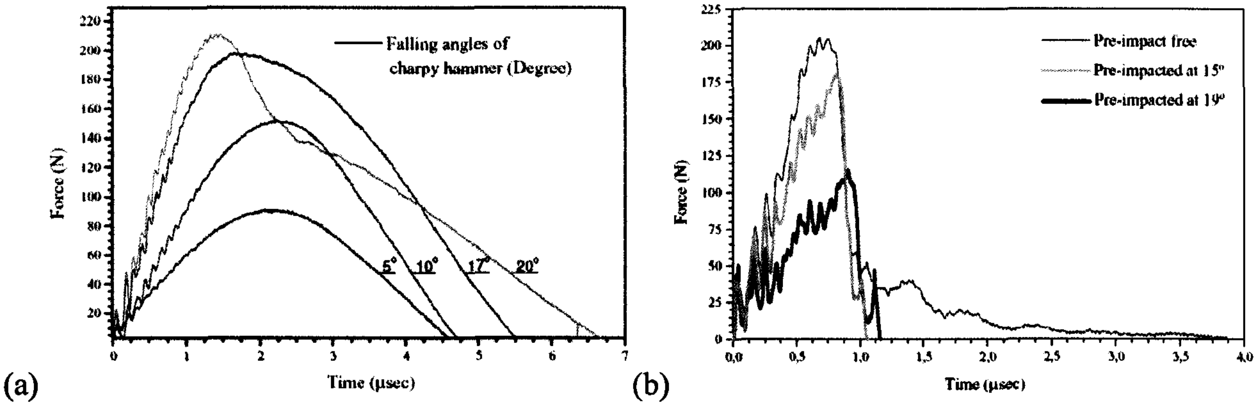

Figure 12. (a) Force-time curves of polystyrene impacted from various angles. (b) Force-time curves illustrating the amount of force required to fracture previously impacted polystyrene (Sahin, Sinmazcelik & Arici, 2004).

The impact conditions in Figure 12 (a), were not forceful enough to cause fracture of the samples, however, elasto-plastic deformation is evident by examining the force-time curves. Crack initiation in the material was not apparent in the 5° and 10° impact angles. The material therefore underwent elastic deformation at these angles. At 17°, however, crack initiation is observed by the asymmetry in the force-time curve. Following, at 20°, there was remarkable crack propagation in the samples. In comparison, Figure 12 (b) shows material fracture force-time curves. Materials which were not previously impacted required more force to fracture, while samples previously impacted from the most forceful impact condition (19°) required the least force to break. Fracture is evident by the sudden drop in the force trace due to catastrophic failure of the material, indicating lower elasticity and poor plasticity (Sahin et al., 2004).

To fully understand an air chamber's behaviour under impact, knowledge of its elastic and plastic deflection under dynamic loading is essential. Force-time curves can graphically illustrate the materials failure characteristics as referred to in the previous discussion on crack initiation and propagation. It is well known that materials with equivalent impact strengths may differ considerably in their breaking behaviour. The force-time curves illustrated in Figure 13 graphically demonstrates this behaviour.

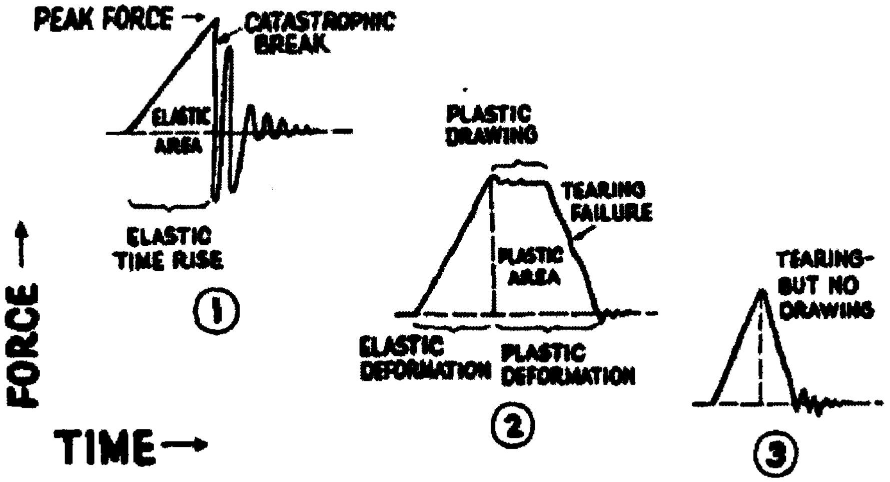

Figure 13. Types of impulse curves (Wolstenholme, 1962).

In general, there are three types of impulse curves. In the first, a sample deforms uniformly under the impact until a peak force is reached, followed by the sample yielding and breaking catastrophically, evident by the force dropping to zero. The vibrations shown in the figure after the peak rise are from the mechanical vibrations of the transducer and are referred to as "ringing" of the transducer. In the second impulse curve, the sample undergoes plastic drawing at a constant force after yielding. The sample then displays tearing, as the force drops to zero. The third type of impulse curve shows tearing after yielding without plastic drawing (Wolstenholme, 1962). This latter curve is characteristic of many conventional foams used in helmets and is a "classic" energy absorber force-time curve.

The impulse curves can be further described according to their elastic/plastic deformation characteristics. The elastic deformation region corresponds to the triangle on the left, made up of the elastic rise time (base of the right triangle), hypotenuse (force rate), and peak force. This reversible deformation occurs until the material reaches its yield strength, in which the plastic deformation begins. A purely elastic impact can be represented by a half sine wave on a force-time curve (Feraboli, 2006). Figure 14 illustrates force-time photographs of various thermoplastics.

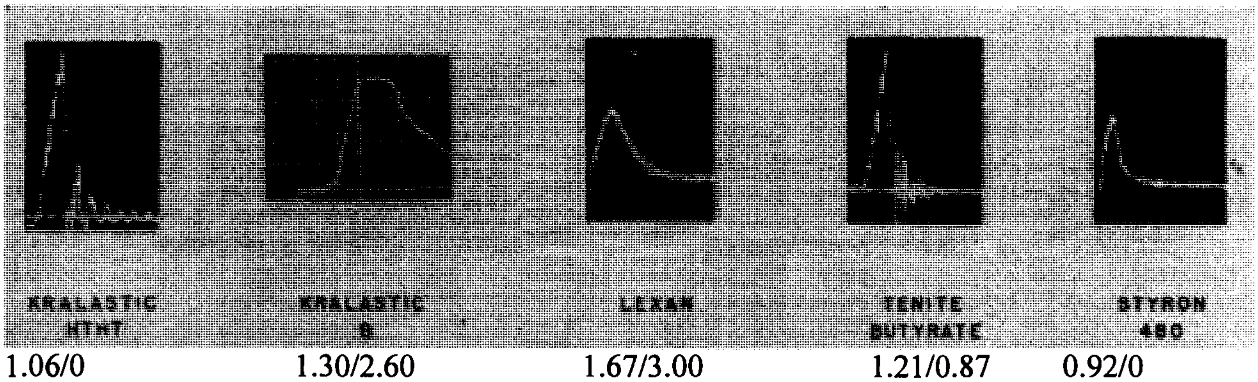

Figure 14. Force-time photographs of five thermoplastics with elastic/plastic break times (ms) listed below force-time trace (Wolstenholme, 1962).

Devices which use plastic deformation have been used extensively as a means of absorbing impact energy (Abdul-Latif & Nesnas, 2003); however, plastic deformation is irreversible. Plastic energy absorbers convert kinetic energy into permanent deformation of the structure (Aljawi et al., 2005). Thus, although a critical amount of plastic material is required in the structure, the dynamic air chambers must contain enough elasticity to regain their shape following an impact.

The plastic deformation of a tubular structure is usually attributed to axial loading, loading in which the applied force is along the axis of the object. According to Alghamdi (2001), "optimal energy absorption is obtained through progressive plastic buckling which avoids overall elastic buckling" (p.202). Thus, the energy absorption capability of the chambers is dependent on the plastic deformation which occurs as they compress. In addition, circular tubes under axial loading have been suggested to be one of the most prevalent components in energy absorbing systems and exhibit favorable plastic behaviour under axial forces (Alexander, 1960; Alghami, 2002). In comparison to lateral compression, axial compression has approximately ten times greater energy absorbing capacity for a given tube. Consequently, given the mechanics involved in the collapse of thin-walled cylindrical structures, it is important that the dynamic air chambers contain a balance between plastic and elastic elements.

2.7.4. Controlled Venting System

One key element of the dynamic air chambers is the air venting system, which can be altered by changing the chamber vent diameters. The air chamber vents are used as one mechanism to manage energy absorption of the chamber. The vents are able to help control the rate of collapse of the chambers and manage resistance to impact, decreasing the amount of force transmitted to the head.

2.7.4.1. Characteristics of Air Flow

The behaviour of air within the chamber is important to understand as it affects the air's ability to flow through the vent and thereby manage the energy of an impact. Although little research exists explaining the relationship between vent air flow rate, volume per unit time, and force, there are some general characteristics of any gas which can be applied to the dynamic air chambers. For instance, air flow only takes place when a pressure difference exists. That is, air flows from a region of high pressure to low pressure and its velocity is proportional to the magnitude of the pressure difference (Silberberg, 2000). Therefore, the greater the pressure difference, the faster the air flows. Thus, enclosed air flows out of the impacted chamber into the atmosphere since the pressure within the chamber is greater than outside the chamber.

When air flows at a high velocity, its flow tends to be fairly disorganized or chaotic, a phenomenon known as turbulent flow. A relatively large driving pressure is required for turbulent flow to persist. The pressure driving the air flow is proportional to the square of the air flow rate such that $\Delta p=kv^2$, where Δp is change in pressure or the driving force, k is a constant related to resistance to flow, and v is the air flow velocity (Ball, 1996). Thus, to double the air flow rate, the driving pressure must be quadrupled.

As opposed to turbulent flow, laminar flow exists when air flows at a low velocity, usually through a narrow tube such as an artery. Laminar flow is a more straight and streamlined flow. In contrast to turbulent flow, laminar flow is directly proportional to the driving pressure. Thus, when the driving pressure is doubled, the air flow rate is also doubled. Laminar flow is described by Poiseuille's Law: $\Delta p=8\eta lQ/\Pi r^4$, where Δp is the difference in pressure between the two points, Q is the volumetric flow rate, r is the radius of the tube, η is the gas viscosity, and l is the length of the tube. Thus, the flow through a tube is directly proportional to the radius of the tube (Salvatore & Skalak, 1993). There is also another type of air flow which exists, called transitional flow. Transitional flow is merely a combination of laminar and turbulent flow.

2.7.4.2. Air Flow Rates

Among the most important elements in air flow are deformation, friction, compressibility, and turbulence (Tavoularis, 2005). When air, at a certain temperature and pressure, flows through a restriction such as the vent in the chamber, under the conservation of mass, the air velocity must increase as it flows through the smaller cross section restriction, reducing its pressure and producing a partial vacuum. This is known as the Venturi effect, a special case of the Bernoulli Principle (NASA, 2007). The Bernoulli Principle states that when an ideal fluid flows, an increase in velocity occurs with a decrease in pressure (Guerra, Plaisted & Smith, 2005). Bernoulli's Law can be expressed by the formula $p + \frac{1}{2} \rho v^2 + \rho g h = constant$, where p is the pressure, ρ is the density of the fluid, v is the fluid velocity, g is the gravitational acceleration, and h is the height of the fluid. This equation neglects friction (in viscous fluid) and assumes there is steady and incompressible flow.

As fluids flow, they may be compressible or incompressible. Mach number, the ratio M of fluid velocity to the speed of sound (340.3 m/s), describes the effects of compressibility. Sonic flow exists when $M=1$, transonic when $0.8<M<1.2$, supersonic flow exists when $1.2<M<5$, and hypersonic when $M>5$. Flow is considered supersonic when the change in density with respect to pressure becomes zero. In general, this occurs when the Mach number approaches or exceeds 0.3. With gas flows having a $M<0.3$, the change in density with respect to pressure is negligible. In compressible flows, density variations become significant, which are related to pressure and temperature variations (Tavoularis, 2005). In contrast, with incompressible flows, compressible flow models contain, in addition to velocity and pressure, two additional unknowns, density and temperature.

According to Kawashima, Fujita & Kagawa (2000), in industry, flow rate is one of the most imperative measurements in which high accuracy and high dynamic response are of utmost importance. Nevertheless, a difficulty exists in measuring the flow rate of a compressible fluid such as air because its density is sensitive not only to pressure but also to temperature (Kawashima, Fujita & Kagawa, 2001a). In isothermal chambers, chambers in which the temperature remains constant, instantaneous flow rates can be determined only by measuring pressure (Kawashima, Fujita & Kagawa, 2001b). If the state of air remains isothermal during flow, the state equation is: $G=(V/R\theta_a)(dp/dt)$, where G is the mass flow rate (kg/s), V is the volume of the isothermal chamber (m^3), R is a gas constant (J/kg·K), θ_a is room temperature (K), p is the pressure in the isothermal chamber (Pa), and t is time (s). Thus, if the volume in the chamber and the room temperature are known, the mass flow rate can be determined by measuring the pressure. Then, the mass flow rate can be converted into volumetric flow rate (Q) using the following equation: $Q=kG$, where k is a conversion factor (m^3/kg) (Kawashima et al., 2001b).

It has been suggested that in pneumatic systems, systems containing air, the air flow rate may be nonlinear, since air is a compressible fluid (Kawashima, Ishii, Funaki & Kagawa, 2004). Further, fluid flow within a vertical cavity has been stated to be "one of the most complicated fluid dynamics problems" (Tian & Karayiannis, 2000, p.867), since flow within a vertical cavity can be laminar, transitional, and turbulent. Thus, the behaviour of air as it escapes the dynamic air chamber presents a difficult problem, as its flow characteristics are unknown. Nevertheless it is essential that these properties are established to fully understand how the venting system works, and therefore, how the chamber manages energy using the vents.

2.7.5. Research Problem

The purpose of the present study is to determine how vent diameter contributes to manage energy absorption in dynamic air chambers. That is, the main objective of the study is to determine the relationship between chamber vent diameter and peak force during an impact. To study chamber vent diameter, chamber venting rates will be examined. Therefore, the relationship between chamber vent diameter and air flow rate during an impact will be determined. The relationship between chamber vent rate and force will also be determined to see if it may be vent rate, and not vent diameter, which alters energy attenuation.

CHAPTER 3. METHODOLOGY

3.1. Research Design

To accomplish the research objectives, a series of chambers were impacted using the drop rig system (see section 3.2.2.1) in accordance with a fully crossed design. Each chamber's unique combination of material stiffness and vent diameter were tested at the three inbound velocities. Two material stiffnesses were used to confirm the robustness of the relationships under different conditions.

A pilot study was conducted using various inbound velocities to determine the range used in the study. The purpose of the pilot study was to determine a range of velocities which characterized the chambers' performance under mild and severe impact conditions, while engaging various mechanisms of energy absorption. The pilot data showed that all chambers under consideration were able to successfully sustain ten repeat impacts at 10 and 30 cm and began to fail at 50 cm. Success was defined as not transmitting more than 10 000 N of force on impact. Therefore, 1.3, 2.3, and 3.0 m/s were chosen for this study, based on 10, 30, and 50 cm impact heights. Each chamber was impacted ten times in three different sets, resulting in a total of 30 trials per chamber condition, to ensure reliability of results between the same type of chamber. Thus, a total of 900 unique impact trials were conducted. An order effect was not expected and, therefore, the order of the treatments was not randomized.

	V1	**V2**	**V3**	**V4**	**V5**	
A1	A1V1T1	A1V2T1	A1V3T1	A1V4T1	A1V5T1	**T1**
	A1V1T2	A1V2T2	A1V3T2	A1V4T2	A1V5T2	**T2**
A2	A2V1T1	A2V2T1	A2V3T1	A2V4T1	A2V5T1	**T1**
	A2V1T2	A2V2T2	A2V3T2	A2V4T2	A2V5T2	**T2**
A3	A3V1T1	A3V2T1	A3V3T1	A3V4T1	A3V5T1	**T1**
	A3V1T2	A3V2T2	A3V3T2	A3V4T2	A3V5T2	**T2**

Figure 15. Study research design for thermal anemometry procedure.

Where:
A1 – 1.3 m/s (10 cm drop height)
A2 – 2.3 m/s (30 cm drop height)
A3 – 3.0 m/s (50 cm drop height)

V1 – 1 mm biopsy punch
V2 – 2 mm biopsy punch
V3 – 3 mm biopsy punch
V4 – 4 mm biopsy punch
V5 – 5 mm biopsy punch

T1 – TPU 45D
T2 – TPU 90A

3.2. Data Collection

3.2.1. Chamber Preparation

Prior to being impacted, each chamber was inspected to ensure there were no visual differences between the samples or any abnormalities within each chamber. To confirm the characteristics of the samples, a series of chambers' vent diameters, wall thicknesses, material stiffnesses, and masses were verified prior to impact by the methods described below.

3.2.1.1. Vent Diameter

The chamber vents were created using skin biopsy punches, small pencil like objects normally used to extract thin cylindrical areas of tissue. The biopsy punches, purchased from Dormer Laboratories Inc., ensured each vent was precise and consistent. Each vent was created using a new biopsy punch. A drill press was used to center the vents in the chamber.

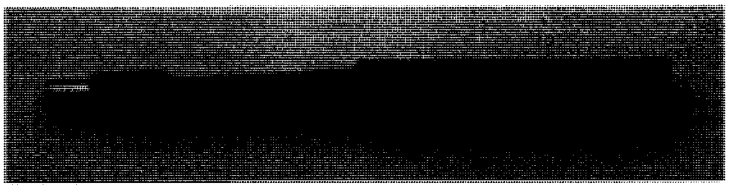

Figure 16. Skin biopsy punch used to create chamber vents (WPI, 2007).

Ten random biopsy punches of three different sizes were verified prior to use, using the Fisher Scientific electronic digital micrometer, model 06-664-16. The caliper's resolution is 0.01 mm with a measuring range of 0 - 500 mm. Its accuracy is 0.03 mm with a 0 – 200 mm measuring range, 0.04 mm with a 200 – 300 mm measuring range, and 0.05 mm with a 300 –

500 mm measuring range. The repeatability of the instrument is 0.01 mm. The caliper was calibrated (certificate number 3416-1569246) on 04/23/2007 and complies with ISO/ISC 17025 and ANSI/NCSL Z540-1 standards (Control Company, 2005). The size of the orifices created in the chambers has been reported as the diameter of the biopsy punch used (i.e. 1-5 mm).

3.2.1.2. Wall Thickness

To ensure accuracy of the chamber wall thickness, the Fisher Scientific electronic digital micrometer was used to measure the walls of ten random samples from three different bags sent from the manufacturer.

3.2.1.3. Material Stiffness

Finally, the material stiffnesses were verified using a durometer (see Figure 18). The hardness of most plastics is commonly measured by a Shore (durometer) test. A durometer, the term used to refer to the both the tool and the measurement, measures a material's resistance to permanent indentation. There are several scales of Shore hardness for materials with different properties (Instron, 2004). The most common scales for rubbers and elastomers are Shore A and Shore D, the two Shore values currently used for the chambers. Shore A and D scales are used for softer and harder plastics, respectively. Some overlap exists between Shore A and D ranges. The following figure illustrates their relationship.

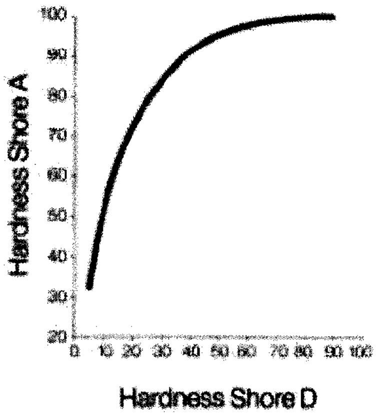

Figure 17. Relationship between Shore A and D ranges (BASF, 2008a).

In addition to A and D scales, B, C, DO, E, M, O, OO, OOO, OOO-S, and R scales exist. Each scale contains values between 0 and 100, with higher values indicating a harder material (Instron, 2004). Thus, the TPU 90A chambers are softer than the TPU 45Ds.

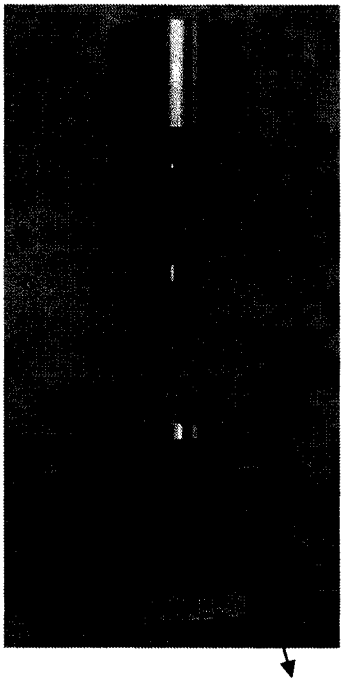

Figure 18. Pacific Transducer Corporation durometer model D shown with test stand (Pacific Transducer Corporation, 2007).

A durometer measures the depth of the indentation in the material created by a given force on a standardized presser foot. This indentation depth is dependent on the viscoelastic properties of the material, such as its hardness, as well as the shape of the presser foot and the duration of the test (National Physical Laboratory, 2007). In this study, durometer testing was performed in accordance with ASTM 2240 standards (ASTM International, 2005). Upon indentation, the maximum reading when the indentor travel ceased was taken. This was determined within one second, as specified by the maximum indicator durometer function. Five measurements on ten random TPU 45D samples, and ten random TPU 90A samples from three different bags were performed. All samples consisted of the impacting surface of the chamber, which was cut out from chambers not previously impacted. Each of the five measurements was taken on different positions on the specimen, greater than 6 mm apart, and the mean was calculated.

Two durometers were used to confirm the hardness of the TPU chambers – the Pacific Transducer Corporation (PTC) 511A digital e2000 durometer to measure the Shore A chambers and the PTC 512D digital e2000 durometer to measure the Shore D chambers. In addition, the PTC operating stand 478 was used with a 1 kg load for the Shore A chambers and a 5 kg load for the Shore D chambers. A calibration sheet was provided with each durometer, which were calibrated by the manufacturer 07/05/2007.

3.2.1.4. Mass

Ten random samples of each material stiffness from three random bags were weighed using a Denver Instruments SI 603 balance which has a capacity of 600 g and readability of 0.001 g.

3.2.2. Drop Procedure

3.2.2.1. Drop Rig

To test the energy absorbing characteristics of these chambers, the monorail drop rig was used (see Appendix E for additional photographs).

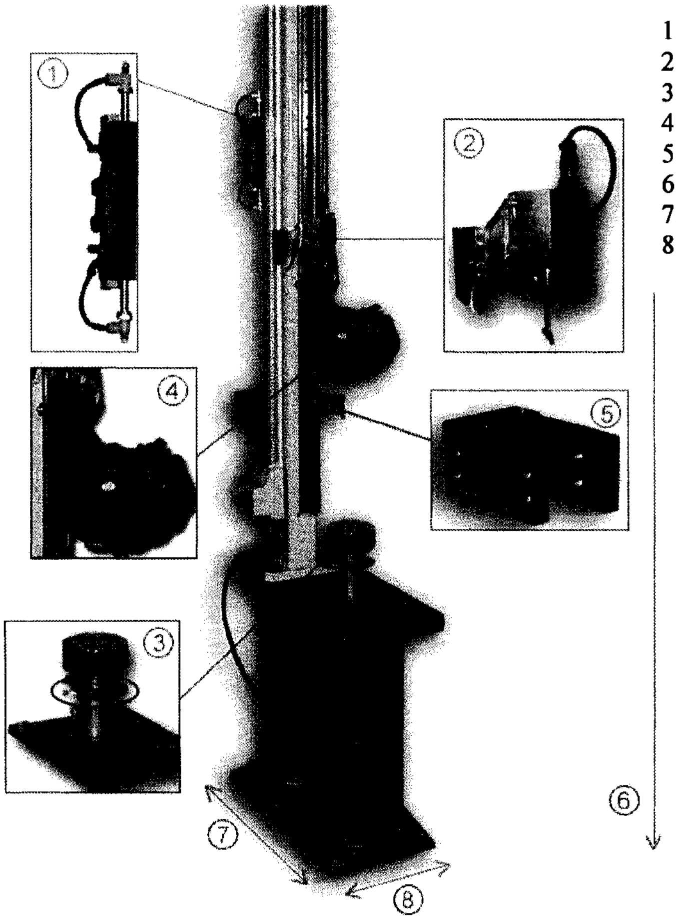

1. Tri-axial headform catch
2. Drop carriage
3. Anvil quick release support clamp
4. Half magnesium headform K1A
5. Time gate
6. Linear impactor track
7. The depth of the base: 25"
8. The width of the base: 12.5"

Figure 19. Cadex monorail drop rig used to impact chambers (Cadex Inc., 2006).

The monorail drop rig is designed to simulate an impact of a freely falling head and is currently used to certify all hockey, bicycle, industrial, equestrian, and motorized vehicle head protection devices, among several others.

This impact tower consists of a concrete pedestal, linear bearing rail, lift carriage, drop carriage, and lift motor. A headform can be mounted on the drop carriage via a universal ball.

The base of the system, 26.5” in height, 12” in width, and 15” in depth, is attached to the concrete floor via six bolts, creating a solid platform beneath the drop carriage. The block reduces unwanted background noise and vibration. The 6 m linear bearing rail is also attached to the wall to ensure there is no movement of the system.

Attached to the base of the system is an anvil consisting of 6061T6 aluminum red anodice, 1” in thickness and 7.5” in diameter. This anvil is mounted with a quick release device, allowing various anvils to be changed quickly and with ease. A metal plate is fixed to the anvil on which a force ring rests. For this study, a customized steel cylinder, 15 cm in height and 15 cm in diameter, was placed on the force ring and was attached to the metal plate using a beryllium copper stud. A chamber was then capable of being secured to the jig, ensuring it did not move upon impact and allowed appropriate space to enable air flow measurements (see Appendix E for photographs of jig).

The system contains a drop carriage assembly to which a headform is attached and this assembly is secured to the linear beam. The headforms are attached to the drop assembly via a universal ball. For the purpose of this study, a half EN 960 magnesium K1A headform was used (see Appendix E). These headforms are used for all uniaxial impacts. The magnesium headform contains a socket-like opening to which the universal ball can be secured.

There are a variety of headform weights and sizes capable of being used with the monorail drop rig. For this study, the ISO headform M was used in the crown position. The geometrical shape of the headform changes as the headform position changes. Consequently, the crown position was chosen primarily because it impacted the entire chamber symmetrically, as well as due to the ease and accuracy in positioning the headform on the ball and arm support assembly. The ISO M headform is 4.982 kg, representing the average weight of an adult human head. The entire drop carriage assembly consists of the headform (3201 g), split ring clamp (421 g), four bolts for clamp (83 g), total flying arm (677 g), accelerometer kit (11 g), aluminum ball arm (589 g). The certificate of conformity for this headform was issued on 05/01/2007 (serial number 4770). The headform size is 60 cm, measurement of round head is 600 mm, and frequency resonance is above 3000 Hz. It is made of 100% pure magnesium K1A, with an additive of 0.3% to 0.7% zirconium material and meets conformity standards ISO/DIS 6220.

The drop carriage assembly was lifted manually to an impact height based on the desired impact velocity. When the "drop" button was then pressed, the drop carriage assembly was released smoothly onto the chamber. As the headform made contact with the sample the force ring produced a signal, conditioned by a signal conditioner, which relayed the signal to a computer using a BNC cable through an analog to digital converter (ADC). The ADC converted the analog signal, a voltage varying, continuous signal, into a digital signal, a numerical representation which can be understood by digital computers (Robertson et al., 2004). This enabled a graphical representation of the impact on the computer.

The overall validity and reliability of the drop system set-up is equal to the validity and reliability of its individual parts. Each part will be considered separately in the following sections.

3.2.2.2. Force Sensor

The PCB Piezotronics Dynamic Force Sensor, Model 203B was used in this study (PCB Piezotronics, 2003). This ICP sensor has a sensitivity of 0.0539 mV/N, linearity of 0.3% FS, uncertainty of ± 1%, and bias of 10.12 VDC. It was last calibrated by the manufacturer with a 081A13 beryllium copper mounting stud on 11/15/2006 by PCB (certificate number 243175). The force sensor was preloaded to 4000 lbs (0.952 V) to ensure the sensor would perform as calibrated (PCB Piezotronics, 2003). It was validated by placing a known mass on the force plate.

The vertical force of the known mass (mass * force due to gravity – 9.81 m/s^2) was compared to the force outputted to the computer. These two values were the same and therefore, the system was considered valid. Data were collected at 20 000 Hz.

3.2.2.3. Signal Conditioner

The PCB Piezotronics Line-Powered ICP Sensor Signal Conditioner, Model 484B06 was used to process the data (PCB Piezotronics, 2004).

3.2.2.4. High Speed Camera

The Photron Fastcam 512PCI high speed camera was used to determine the headform's inbound velocity (Photron Limited, 2003). The full resolution of the camera is 512 x 512 pixels, 10 bits. Its maximum frame rate at full resolution is 2000 frames per second (FPS) and highest frame rate is 32 000 FPS (512 x 32).

A series of chambers were impacted at each inbound velocity, while using the high speed camera (2000 FPS) and Photron Motion Tools Suite, the PCI camera-operating software. Using Photron Motion Tools Analysis, impact velocity was calculated manually as distance over time. A reflective marker secured to the headform was tracked for ten frames immediately preceding the impact. When tracking was completed, all data were transferred to Excel. The displacement of the tracked marker over ten frames was determined. Thus, knowing that the time interval over ten frames equaled 0.005 s (1 s/2000 frames * 10 frames), the inbound velocity was calculated as displacement/time (m/s). The calculated inbound velocity was compared to the theoretical energy of the falling headform, determined through the equation $E=mgh$ (knowing its weight and drop height). Then, from the equation $E=\frac{1}{2}mv^2$, the headform's velocity was determined ($mgh=\frac{1}{2}mv^2$, therefore, $v=\sqrt{2gh}$).

3.2.2.5. Data Acquisition, Processing, and Analysis

Data were collected using Measurement and Automation and VI Logger configuration based data logging software, from National Instruments. Bioproc2, a data processing software program developed by Dr. Gordon Robertson, University of Ottawa, was used to process the force and air flow signals, from which the peaks and durations were identified. The beginning of contact was identified as the time at which the force was registered by the force plate at 50 N. Anemometry data were filtered using a low-pass filter at 500 Hz to remove small oscillations in the flow field.

Further, Microsoft Excel software was used to combine and graph data files while SPSS (15.0) was used for statistical evaluation of the results. Force-time curves were used substantially in data analysis, as they are critical in determining material impact characteristics (Coban et al., 2008). As stated by Chen, Xi, and Yang (2007), "the impact force history is one of the most important objectives in impact engineering. This is because the force history is usually vital in evaluating the dynamic response and failure behavior of those engineering structures (p. 41)."

3.2.2.6. Testing Conditions

Tests were conducted at laboratory temperatures ranging from 21 to 25.5°C, relative humidity's of 22 to 55%, and barometric pressures of 1004 to 1016 mb. The time between subsequent impacts of a chamber was 30 s.

3.2.2.7. Chamber Temperature

Immediately following each trial, chamber surface temperature was determined using a Fisher Scientific infrared thermometer gun, placed 10 cm away from the chamber. In total, five chambers at each inbound velocity were tested.

3.2.3. Air Flow Measurement

The behaviour of air as it escapes the air chambers was determined initially using flow visualization, followed by thermal anemometry. In the former, injection of smoke into the chambers enabled the flow to be visualized on high speed video (2000 FPS), which was useful in identifying air speed estimates, flow boundaries, and general flow characteristics. Nevertheless, the connection between visible smoke patterns and flow characteristics is somewhat uncertain (Tavoularis, 2005) and, therefore, thermal anemometry was used to identify the flow characteristics more precisely. According to Asanuma, "the importance of simultaneous visual and anemometry measurements should be emphasized" (1977, p.121).

3.2.3.1. Flow Visualization

3.2.3.1.1. Overview

Osborne Reynolds was the first to discover that differences between laminar and turbulent flow and the transition between them could be uncovered by observing the motion of a fluid, through a process called flow visualization (Goldstein, 1996). Essentially, flow visualization is the process by which the dynamic behaviour of fluid flow, such as air flow, is made visible. Using flow visualization, various flow characteristics can be seen such as fluid boundaries and internal motion patterns, without disturbing the air flow.

In this study, the marker/particle tracking technique was used to observe the flow of air out of the chamber. This allows the fluid motion patterns to be determined from the visible movement of foreign materials, also known as smoke, suspended within the fluid. Flow visualization using smoke can typically measure flow rates from 0.1 m/s (Tavoularis, 2005). The word smoke is a broad term which includes a variety of smoke-like materials such as liquid droplets (mists), vapours, fumes, and tracer gases (Goldstein 1996; Tavoularis, 2005). The suspended particles are typically less than 1 μm, small enough to follow the fluid motion.

One of the most common and cheapest methods for generating smoke is using vaporization and condensation of mineral oils, which was used in this study. To generate this type of smoke, oil flowing in a tube is heated by an electric heater and evaporates. It then mixes with a cool air stream in which it condenses, forming a mist of tiny droplets in the submicrometre range (oil mist) (Tavoularis, 2005).

Using the smoke method of fluid visualization, streamlines, streak lines, or path lines may be seen. Streamlines are curves which are tangent to the velocity vector of the flow - they are everywhere parallel to the direction of the fluid flow. Streak lines are the centres of all air particles which have passed by a particular fixed point over an interval of time. Path lines are curves crossed by a particular fluid particle during a specified interval of time (Goldstein, 1996). That is, they are the trajectory that a fluid particle makes as it travels with the flow. When flow is steady and therefore, not time dependent, the streamline, streak line, and path line that traverse a particular point are identical. On the other hand, when flow is unsteady and time dependent, the three lines are usually different (Goldstein, 1996).

Digital computers are now used extensively to obtain quantitative information from the flow visualization technique. Using the video images, particles can be identified and tracked, inferring the fluid motion. Nevertheless, some difficulties can arise during the digitizing of the data since particles may be indistinguishable from one another (Hesselink, 1988). As well, tracks can cross and fast particles may move out of the sheet of light. The accuracy of particle tracking methods is dependent upon the care given to the recording of the video and the video processing (Hesselink, 1988). Nevertheless, researchers who have focused on the error associated with particle tracking methods have found that the velocity calculated using by tracking particles was sufficient to compute vorticity (Agui & Jimenez, 1987).

The first step in processing the image is usually edge detection in which boundaries with different regions can be identified. The velocity of the air flowing can be determined by the distance between streaks in the event. That is, the velocity of air will be slow where the distance between neighboring streaks is large and will be fast where the streaks are closer together (Goldstein, 1996). In addition, if a vortex of air occurs, it will be distinct from the flow. The streaks of the steady state flow will maintain nearly fixed positions upstream, whereas the streaks in the vortex will fluctuate continually as the air moves downstream, indicating unsteady flow (Goldstein, 1996).

3.2.3.1.2. Flow Visualization Procedure

The Nutem Integrated Smoke Generator System E was used in the present study, to determine the chamber's range of air flow velocities on impact and general flow characteristics. It can be used for applications involving flow rates less than 8 m/s (Nutem Limited, 1986). This generator forms the oil mist by atomizing the heated mineral oil in an air stream (see Figure 19).

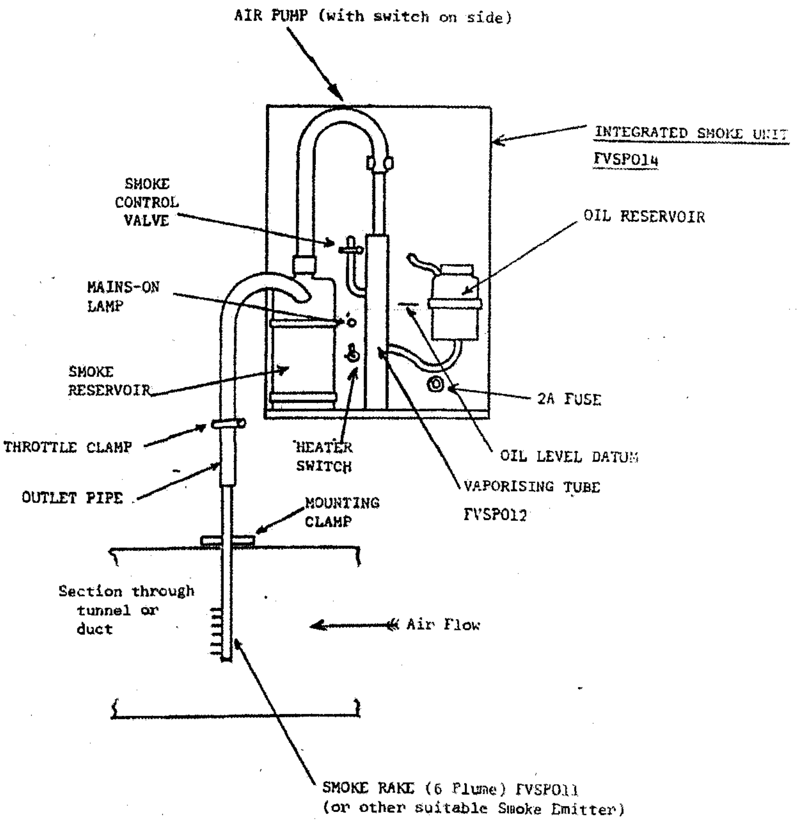

Figure 20. Diagram of a Nutem Integrated smoke generator (Nutem, 1986).

The resultant vapour consists of a suspension of fine liquid droplets which forms the smoke suitable for photography or videography, as it is highly visible. The oil is gravity-fed from an oil reservoir to a Pyrex vaporizing tube which includes an electrical heater. Using a diaphragm pump, the vapour then passes to a flexible smoke reservoir which smoothes out the flow. To control the smoke generation, a valve is situated next to the vaporizing tube. The contents of the smoke reservoir can then be discharged through an outlet pipe which is connected to the smoke reservoir (Nutem Limited, 1986).

The smoke was injected into the chambers through the small orifice used for the vent. Immediately after injection, the chamber was placed on a custom jig (see Appendix E) and impacted. The steel jig contained an open space to visualize the flow as well as an opening for the anemometer. The Fastcam high speed camera, triggered in sync with the event, was used to record the image.

3.2.3.2. Thermal Anemometry

3.2.3.2.1. Overview

In addition to flow visualization, a hot-wire anemometer was used to collect more precise data on the air flow characteristics of the impacted chamber. Thermal anemometers measure fluid flow velocity by sensing changes in heat transfer from a small, electrically heated metallic sensor, such as a hot wire, which is exposed to the fluid (Tavoularis, 2005). The electrical current increases the temperature of a resistor on the substrate. When air flows past the wire, temperature is reduced and the cooling effect is directly proportional to the mass flow and therefore to the air velocity and inversely proportional to the air temperature (Tavoularis, 2005).

A thermal anemometer consists of a sensor, usually a wire or a film, forming the heating element, prongs (sensor supports) carrying the sensor and leading the current to it, a probe body carrying the sensor supports, and a connector providing the electrical connection to the probe support or probe cable. For research thermal anemometry, traditional sensors have been thin wires suspended between two prongs. Wire sensors are typically used for gases and non-conducting liquids, particularly for measurements at very low velocities (a few cm/s) (Dantec Dynamics, 2000b). For flow of very low turbulence, the smaller the wire is, the better the results (TSI, 2006). Wire sensors have high flow sensitivity and the highest frequency response as well as the best signal to noise ratios (TSI, 2006). Nevertheless, the mechanical strength is limited and they are sensitive to particle contamination (Tavoularis, 2005).

In the past, platinum, nickel, and other alloys were used as sensors; however, today platinum alloys are almost exclusively used, usually containing 20% iridium or 10% rhodium, and tungsten (Tavoularis, 2005). Although weaker, platinum wires can withstand high temperatures in an oxidizing atmosphere such as air and can be manufactured very small. Fiber-films are more rugged than wire sensors and are less sensitive to contamination.

The sensors are typically 0.5 to 1.5 mm long, and their diameter ranges from 5-200 μm. Thicker sensors are used for higher strength turbulent flows, whereas thinner sensors are used for low turbulent flows (Tavoularis, 2005). At its two end regions, the sensor is mounted on thin metallic prongs. Fiber-film sensors are quartz fibers, covered by a nickel film approximately 0.1 μm. The ends are copper and gold plated. The ends of the fiber are soldered to the prongs.

One disadvantage of the spot welded sensors is that they are active over their entire length which enables temperature non-uniformity due to heat conduction of the prongs. To overcome this problem, a sensor which is active only in the middle region can be used. That is, its two end portions are much thicker than the active sensor region and therefore not subjected to significant heating. This is done by gold plating the ends of the wire (Tavoularis, 2005).

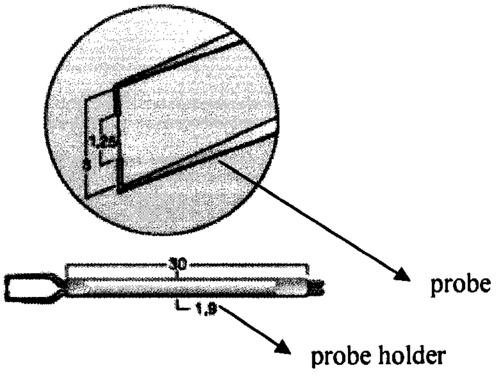

Figure 21. A fiber-film sensor with a diameter of 70 μm, gold plated at the ends, and an active sensor length of 1.25 mm. All measurements shown in mm (Dantec Dynamics, 2000b).

Hot wire anemometers are typically calibrated by inserting the sensor into a low-turbulence calibration facility which contains a free jet tunnel and requires air from a pressurized air supply (Tavoularis, 2005). The sensor is placed at the jet exit and its output is recorded for a full range of velocities, while the flow temperature is closely monitored. In particular, high velocity flows, such as in this study, can be easily calculated from pressure differences obtained.

3.2.3.2.2. Thermal Anemometry Procedure

The Miniature CTA was used from Dantec Dynamics (Dantec Dynamics, 2000a). It is mounted in a small box containing BNC connectors and operates from a 12 VDC power adaptor or by a battery. The bandwidth (maximum of 10 000 Hz) is optimized for wire probes and the signal conditioner is contained within the box. The anemometer was inserted into an opening on the customized jig. This allowed the sensor to be positioned directly under the vent.

For the purposes of this study, the platinum, spot welded wire was attempted; however, it was too weak to withstand the impact conditions. Therefore, a fiber-film sensor made of nickel was used, measuring one-dimensional flow. The sensor measured 1.25 mm in length and 70 μm in diameter and was designed to measure velocities from 0.20 m/s to 350 m/s (Dantec Dynamics, 2000b). The anemometer was calibrated using the technique described below and was used immediately after calibration.

3.2.3.2.3. Calibration of Anemometer

The Type 55D41/42 Calibration Equipment, a small subsonic miniature wind tunnel was used to calibrate the anemometer.

Figure 22. Photograph of a mini wind tunnel used for calibration of a hot wire anemometer.

This equipment provided a turbulence free, variable velocity air source for static calibration of the thermal anemometer (DISA). The calibrator, accurate within ± 0.5% generates air speeds from 1 to 200 m/s, with background turbulence less than 0.15% at 100 m/s.

To calibrate, the anemometer probe was mounted onto the probe support. The flow velocity was derived from the static pressure differences between the measuring section and the reservoir, using a pressure transducer. Variations in the line voltage corresponded to velocity variations.

More specifically, Bernoulli's Principle and the Conservation of Mass (continuity for fluid mechanics) were applied to the anemometer calibration. The following form of Bernoulli's principle was used: $\frac{1}{2}v^2 + p/\rho + gh = constant$. Since energy is conserved along a streamline, Bernoulli's Law can be written as $p_1 + \frac{1}{2}\rho v_1^2 = p_2 + \frac{1}{2}\rho v_2^2 = constant$. The equation of the Conservation of Mass (continuity in fluid dynamics) states that matter cannot be created nor destroyed. Therefore, the mass entering the system is equal to the mass leaving the system plus the increase of mass in the control volume. When flow is steady, there is no increase in control volume mass. Therefore, mass flow rate (kg/s)=$\rho_1 v_1 A_1 t_1 = \rho_2 v_2 A_2 t_2$, where ρ is the density (kg/m^3), v is the velocity (m/s), A is the area (m^2), $\rho_1 = \rho_2$ in incompressible flows and $t_1 = t_2$.

Thus, when the air flows through the orifice, the Bernoulli equation was adapted as $g{*}D_1 + p_1/\rho + v_1^2/2 = g{*}D_2 + p_2/\rho + v_2^2/2$, where D_1 is the diameter of the reservoir and D_2 is the diameter of the measuring section. From this equation, $V_2 = \sqrt{2(p_1 - p_2)/\rho(1-(D_2/D_1)^4)}$.

Calibration Procedure:

The calibration consisted of four instruments: (1) a water manometer, (2) a pressure transducer connected to a (3) wind tunnel and (4) the anemometer (S.M. Guellouz, personal communication, July 2007).

Pressure Transducer versus Liquid Manometer

First, the pressure transducer was calibrated using a water manometer - a pressure measurement instrument used to determine the pressure difference in a gas. A liquid column, U shaped manometer was used, partially filled with water. One side of the manometer was connected to the pressure transducer, the other open to atmospheric pressure. The pressure transducer was connected to the wind tunnel, which when turned on, caused the liquid in one side of the U tube to rise/fall with respect to the other, in proportion to the pressure change. The pressure transducer was also connected to a voltmeter. Thus, the input was related to the difference in heights of the two liquid columns (outputs) by Pascal's Law: $\Delta p=\rho g\Delta h$, where Δp is the hydrostatic pressure (Pa), ρ is the liquid density (water=1000 kg/m^3), g is the acceleration due to gravity, and Δh is the difference in elevation of two points in the column (m). The input was correlated to the electric voltage output by the expression $\Delta p = a(v-v_0) + b$, where a and b are constants determined by the calibration of the transducer versus the liquid manometer, v is the output of the pressure sensor, and v_o is the zero offset of the voltmeter due to sensor drift. The step by step procedure is outlined below.

Step 1: $v_{0\ \mathrm{transducer}}$ was recorded before air velocity was turned on.

Step 2: Air was turned on to a given velocity. $v_{\mathrm{transducer}}$ and Δh of the water were recorded. This was repeated for various velocities.

Step 3: Δp was then calculated, as $\rho g\Delta h$ was known.

Step 4: Plotted pressure difference Δp versus transducer voltage $(v-v_0)$ to get calibration curve, where $R^2>0.99$. Subsequent tests of the slope of the pressure transducer output did not change and, therefore, the linear regression equation was valid for all tests.

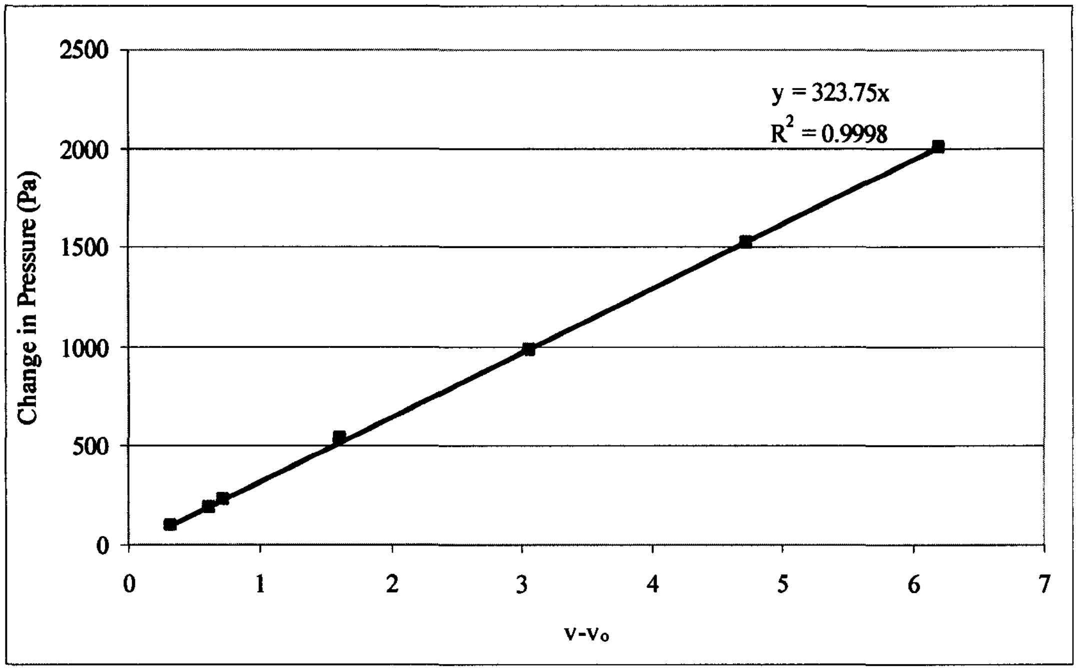

Figure 23. Example of pressure transducer calibration graph.

Anemometer versus Wind Tunnel

To calibrate the anemometer it was first necessary to determine the velocity of air in the wind tunnel for various pressure differences which were manually changed. To accomplish this, the step by step procedure is outlined below.

Step 1: Connected voltmeter to pressure transducer which indicates voltage based on pressure difference between reservoir and measuring section in the wind tunnel) and recorded $V_{0\ \mathrm{transducer}}$ (no air flow in tunnel).

Step 2: Connected anemometer to Measurement and Automation (collected at 20 000 Hz).

Step 3: Air flow turned on to a given velocity. $v_{\mathrm{transducer}}$ was recorded and E of the anemometer was also recorded using Measurement and Automation. Repeated for various velocities.

Step 4: From this information, the air flow velocity in the tunnel was calculated using Bernoulli's Principle: $U_{\mathrm{wind\ tunnel}} = \sqrt{(\Delta p)/\rho_{\mathrm{air}}(1-(D_{2\ \mathrm{measuring}}/D_{1\ \mathrm{reservoir}})^4)}$, where the change in pressure is related to the air flow velocity inside the wind tunnel. That is, the change in pressure is equal to the voltage reading minus the reference velocity (voltage when zero air flow velocity) multiplied by the slope of the pressure transducer calibration. Thus, $\Delta p=(v_{\text{given velocity}} - v_0)^*$(slope of calibration curve), ρ_{air} is the density of air in the wind tunnel (1.2 kg/m^3 at sea level and 20°C), D_2 is the diameter of the wind tunnel's measuring section (14 mm) and D_1 is the diameter of the reservoir section (61 mm).

Step 5: Plotted $E^2_{\text{anemometer}}$ versus $U_{\text{(wind tunnel)}}{}^n$, to obtain calibration curve.

Step 6: Determined the value of n, a constant between 0.4 and 0.55, which resulted in the highest R^2 value (most linear line). If the correlation coefficient for the data was less than 0.999, the calibration was repeated.

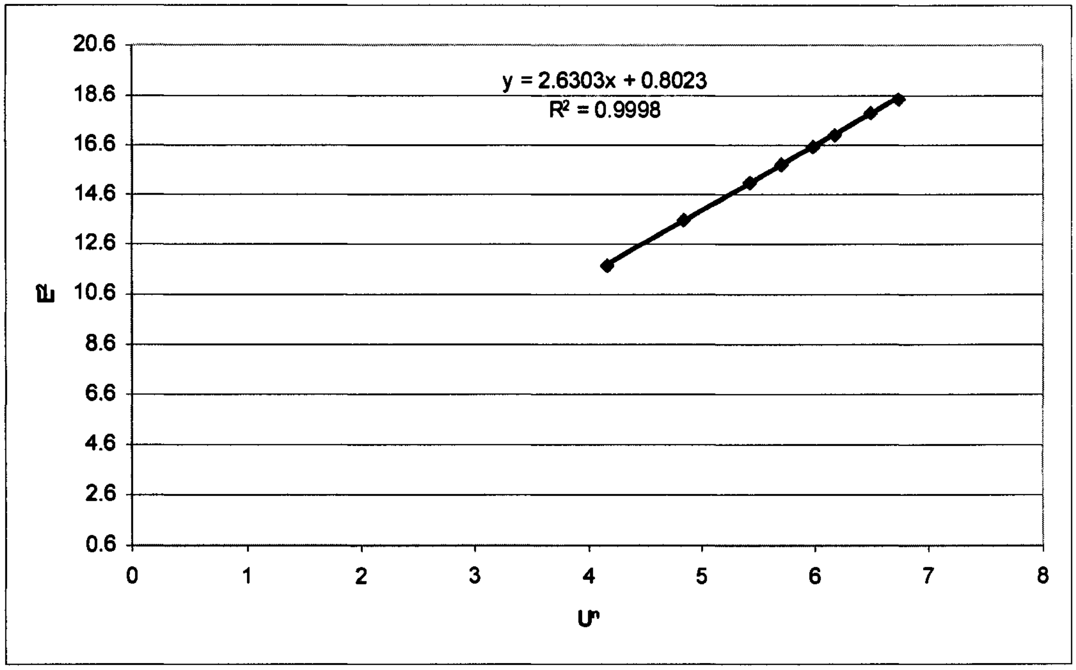

Figure 24. Example of anemometer calibration graph.

King's Law, $E^2=A + BU^n$, was then applied, to determine the air flow velocity past the sensor at a given velocity. That is, A=intercept of anemometer calibration curve, B=slope of calibration curve, n=constant from calibration curve, E=anemometer output voltage, and U=air flow velocity past hot wire.

CHAPTER 4. RESULTS

4.1. Flow Visualization

Analysis of flow visualization results revealed the air flow velocities were much greater than anticipated. Originally, it was hypothesized that the air was escaping the chambers on impact at less than 5 m/s. Upon manual digitization of video images, it was discovered the air speed was upwards of 50+ m/s. Therefore, flow visualization was not used to determine air flow velocities. Nevertheless, flow visualization enabled a qualitative description of the motion of air as it left the chambers.

Similar air flow patterns existed between all chambers. At the beginning of the event, when air initially escaped the chamber, the flow appeared turbulent near the chamber orifice. This turbulent flow then became more laminar and streamlined at the orifice and downstream, as the impact continued. The first particles expelled from the chamber eventually became turbulent downstream, as can be seen in the following series of photographs.

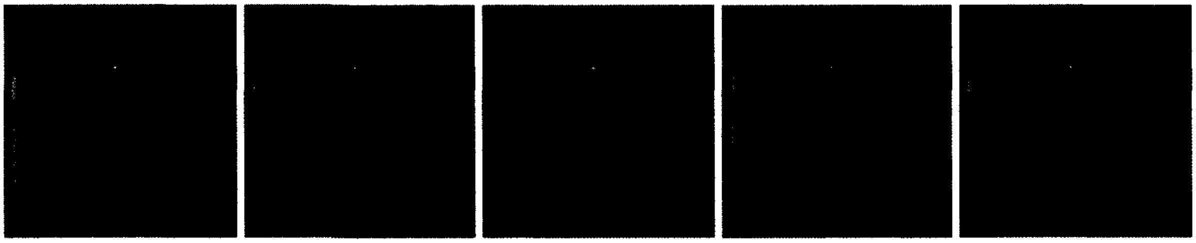

Figure 25. Air flow pattern as it escapes a TPU 90A chamber with a 5 mm vent diameter impacted from 30 cm.

4.2. Thermal Anemometry

4.2.1. Part A

Two three-way ANOVAs were used to determine if significant relationships existed between vent diameter, material stiffness, inbound velocity and force as well as the independent variables and air flow rate. When significant main effects were found, pairwise comparisons were computed for all levels of the independent variable using the Bonferroni *post hoc* multiple comparison analysis tool - one of the most conservative *post hoc* tests (George & Mallery, 2007). In addition, a Pearson's correlation was performed to determine the relationship between air flow (peak vent rate and duration) and peak force to establish if vent rate or duration had an effect on the energy attenuation ability of the chambers.

A between subjects design was used to examine the mean peak force (N) and air flow rate (m/s) values for all combinations of material stiffness (hard – TPU 45D and soft – TPU 90A), vent diameter (1-5 mm) and inbound velocity (1.3, 2.3, 3.0 m/s). The mean peak force and air flow rate values are shown in Table 3.

Material Stiffness	Vent Diameter (mm)	Inbound Velocity (m/s)	Mean Force (SD) (N)	n	Mean Air Flow Rate (SD) (m/s)	n
TPU 45D	1	1.3	965.41(30.30)	30	70.90 (17.11)	30
	2		976.43 (56.49)	30	104.70 (16.33)	29
	3		935.69 (23.15)	30	127.71 (5.56)	30
	4		905.15 (40.38)	30	118.18 (4.30)	30
	5		922.86 (27.59)	30	98.06 (2.25)	30
TPU 45D	1	2.3	1466.13 (182.36)	30	80.98 (14.40)	30
	2		1329.93 (36.92)	30	148.70 (22.82)	30
	3		1224.62 (62.13)	30	172.72 (28.29)	28
	4		1387.01 (322.87)	30	144.63 (35.96)	30
	5		1493.44 (197.36)	30	149.89 (43.27)	29
TPU 45D	1	3.0	8018.54 (1540.16)	30	107.87 (20.61)	30
	2		8453.00 (1690.70)	30	118.80 (19.31)	30
	3		8700.12 (1397.67)	30	129.64 (15.26)	30
	4		10481.86 (1189.34)	30	135.18 (16.69)	30
	5		11767.84 (1091.89)	30	146.18 (29.05)	30
TPU 90A	1	1.3	755.69 (14.84)	30	78.00 (14.15)	30
	2		720.39 (12.22)	30	128.03 (6.48)	30
	3		688.63 (24.02)	30	117.03 (14.97)	30
	4		676.81 (30.49)	30	123.78 (1.49)	30
	5		637.90 (21.17)	30	109.70 (2.34)	30
TPU 90A	1	2.3	2098.80 (437.20)	30	120.22 (30.51)	30
	2		2077.62 (547.50)	30	168.85 (17.81)	30
	3		3780.48 (1104.82)	30	170.80 (17.58)	30
	4		5487.58 (1175.95)	30	182.74 (22.20)	30
	5		6049.72 (1693.03)	30	169.52 (20.53)	30
TPU 90A	1	3.0	10794.69 (623.45)	30	116.76 (44.70)	30

2	11271.51 (741.17)	30	99.55 (47.53)	30
3	13435.57 (703.89)	30	130.96 (16.22)	30
4	12253.11 (680.04)	30	139.91 (21.92)	30
5	13029.07 (820.69)	30	145.68 (24.23)	30

Table 3. Comparison of mean peak force (N) and air flow rate (m/s) values (with standard deviations) for TPU 45D and TPU 90A chambers with various vent diameters (1-5 mm), impacted from 3 inbound velocities (1.3, 2.3, 3.0 m/s), where N=900 (force) and N=896 (air flow rate).

Data were analyzed using a 3-way ANOVA - 2 x 5 x 3 design (material stiffness by vent diameter by inbound velocity). Analysis of variance assumes the error variances of the dependent variables are equal across the groups investigated. Levene's test for homogeneity revealed the assumption of equality of error variance was violated for force, $F(9, 290)=16.751$, $p<0.05$, and air flow, $F(29, 866)=29.74$, $p<0.05$. Nevertheless, further analysis indicated skewness and kurtosis values of 0.707 and -1.170 respectively for force and -0.051 and -0.221 for air flow. Thus, since both skewness and kurtosis were both within ± 1.96, normality in the distribution of the data was assumed. According to SPSS, upon seeing a violation in the equality of error variance, most researchers confirm the measures of normality and if nothing is unusual, the ANOVA analysis is accepted as valid (George & Mallery, 2007). The measures of homogeneity of variance act more as a warning than as a disqualifier. Consequently, the statistical analysis was continued in this study.

Analysis indicated there were very significant main effects of material stiffness on peak force, $F(1, 870)=990.97$, $p<0.001$, partial $\eta^2=0.533$, and peak air flow rate, $F(1, 866)=40.70$, $p<0.001$, partial $\eta^2=0.045$; vent diameter on peak force, $F(4, 870)=140.39$, $p<0.001$, partial $\eta^2=0.392$, and peak air flow rate, $F(4, 186)=122.81$, $p<0.001$, partial $\eta^2=0.362$; and inbound velocity on peak force, $F(2, 870)=13798.25$, $p<0.001$, partial $\eta^2=0.969$, and peak air flow rate, $F(2, 186)=263.62$, $p<0.001$ partial $\eta^2=0.378$. In addition, significant two-way interactions were found between material stiffness and vent diameter on peak force, $F(4, 870)=22.21$, $p<0.001$, partial η^2=0.093, and peak air flow rate, F(4, 186)=6.6338, $p<0.001$, partial η^2=0.028; material stiffness and inbound velocity on peak force, F(2, 870)=327.65, $p<0.001$, partial η^2=0.430, and peak air flow rate , F(2, 186)=20.83, $p<0.001$, partial η^2=0.046; and vent diameter and inbound velocity on peak force, F(8, 870)=43.07, $p<0.001$, partial η^2=0.284, and peak air flow rate, F(8, 186)=21.29, $p<0.001$, partial η^2=0.164. Finally, a significant three-way interaction existed between material stiffness, vent diameter, and inbound velocity on peak force, F(8, 870)= 51.01, $p<0.001$, partial η^2=0.319, and peak air flow rate F(8, 186)=4.55, $p<0.01$, partial η^2=0.040.

The ANOVAs revealed the observed power for all main effects and interactions for peak force was 1.0, except for the interaction between material stiffness and vent diameter (0.990) on peak air flow rate and material, vent diameter, and inbound velocity (0.997) on peak air flow rate. This indicated that, with the exceptions stated previously, there was a 100% chance of finding significant differences between each group in any particular sample with the same sample size. Each main effect and interaction of the independent variables on peak force and air flow rate was further analyzed and will be considered separately in the following analysis.

4.2.1.1. Main Effects

Material Stiffness

Results revealed that 450 impacts of TPU 45D resulted in a lower mean peak force transmission than TPU 90A. As well, air expelled from the TPU 90A chambers traveled at a faster rate than from the TPU 45D chambers (see Table 4). The effect size indicated that 53.3% of the variance in peak force and 4.5% of the variance in peak air flow was accounted for by material stiffness.

Material Stiffness	Vent Diameter (mm)	Inbound Velocity (m/s)	Mean Force (SD) (N)	n	Mean Air Flow Rate (SD) (m/s)	n
TPU 45D	Total	Total	3935.27 (4096.55)	450	123.37 (34.51)	446
TPU 90A			5583.84 (5016.88)	450	133.44 (36.97)	450

Table 4. Comparison of mean peak force (N) and air flow rate (m/s) values (with standard deviations) for TPU 45D and TPU 90A chambers, across all vent diameters (1-5 mm) and inbound velocities (1.3, 2.3, 3.0 m/s), where N=900 (force) and N=896 (air flow rate).

Vent Diameter

Further, 180 impacts of chambers impacted with the smallest vent diameter, 1 mm, transmitted the least force followed by 2, 3, 4, then 5 mm vents (see Table 5). Further analysis using the Bonferroni *post hoc* test confirmed significant differences in force transmission between all vent diameters, $p<0.001$, except for between 1, 2 mm vents. Analysis also revealed the air expelled from the 1 mm orifice traveled the slowest followed by 2, 5, 4, then 3 mm vent diameters (see Table 5). Subsequent analysis using the Bonferroni *post hoc* test was used to determine where significant differences existed in the peak air flow rate transmitted by chambers with different vent diameters, where $p<0.01$. Significant differences were found between all vents with the exception of between 3, 4, 5 mm vent diameters. This suggests the smallest vents had the lowest air flow rates while the larger vents (3, 4, 5 mm) had faster air flow rates. The effect size indicated that 39.2% of the variance in peak force and 36.2% of the variance in peak air flow was accounted for by the chamber's vent diameter.

Material Stiffness	Vent Diameter (mm)	Inbound Velocity (m/s)	Mean Force (SD) (N)	n	Mean Air Flow Rate (SD) (m/s)	n
Total	1	Total	4016.54 (3989.60)	180	95.790 (32.38)	180
	2		4138.31 (4232.94)	180	128.24 (34.74)	179
	3		4794.19 (4826.51)	180	141.13 (27.78)	178
	4		5198.59 (4746.51)	180	140.74 (29.20)	180
	5		5650.14 (5200.92)	180	136.43 (34.80)	179

Table 5. Comparison of mean peak force (N) and air flow rate (m/s) values (with standard deviations) for chambers with vent diameters ranging from 1-5 mm, across both material stiffnesses (TPU 45D and TPU 90A) and inbound velocities (1.3, 2.3, 3.0 m/s), where N=900 (force) and N=896 (air flow rate).

Inbound Velocity

Analysis indicated that 300 impacts of the chambers impacted from the lowest inbound velocity, 1.3 m/s, transmitted the least force, followed by those impacted at 2.3 m/s, then 3.0 m/s (see Table 6). Further analysis using the Bonferroni *post hoc* test confirmed significance between all inbound velocities, p<0.001. Results also indicated that air flow out of the chambers impacted at 1.3 m/s was the slowest, followed by 3.0 m/s, and 2.3 m/s (see Table 6). *Post hoc* testing using the Bonferroni method confirmed significance between all inbound velocities. The effect size indicated that 96.9% of the variance in peak force and 37.8% of the variance in peak air flow was accounted for by the inbound velocity.

Material Stiffness	Vent Diameter (mm)	Inbound Velocity (m/s)	Mean Force (SD) (N)	n	Mean Air Flow Rate (SD) (m/s)	n
Total	Total	1.3	818.50 (130.92)	300	107.62 (21.64)	299
		2.3	2639.53 (1889.01)	300	150.76 (39.26)	297
		3.0	10820.63 (2122.04)	300	127.05 (31.27)	300

Table 6. Comparison of mean peak force (N) and air flow rate (m/s) values (with standard deviations) for chambers impacted at 1.3, 2.3, and 3.0 m/s, across all vent diameters (1-5mm) and material stiffnesses (TPU 45D and TPU 90A), where N=900 (force) and N=896 (air flow rate).

4.2.1.2. Two-Way Interactions

Material Stiffness by Vent Diameter

For both material stiffnesses, it was determined that the 1 mm vent transmitted the least force, followed by 2, 3, 4, and 5 mm vent diameters (see Table 7). Separate Bonferroni *post hoc* tests were conducted for each material stiffness to determine where significant differences existed in the peak force for each vent diameter. For the TPU 45D material, significance existed between all vent diameters, p<0.01, except for between 1, 2 mm; 1, 3 mm; and 2, 3 mm. For the TPU 90A chambers, significant differences existed between all vent diameters, p<0.01, except for between 1, 2 mm; 3, 4 mm; and 4, 5 mm.

Analysis of the TPU 45D chamber results indicated that the 1 mm vent had the slowest air flow, followed by 2, 5, 4, and 3 mm vent diameters. For the TPU 90A chambers, the slowest air flow was expelled by the 1 mm vent, followed by 2, 3, 5, and 4 mm vents. Separate Bonferroni *post hoc* tests were also conducted for each material stiffness. For the TPU 45D material, significance existed between all vent diameters, $p<0.05$, except for between 2, 4 mm; 2, 5 mm, and 4, 5 mm. For the TPU 90A material stiffness, significant differences existed between vents, $p<0.01$, except for between 2, 3 mm; 2, 5 mm; 3, 5 mm; and 4, 5 mm vent diameters.

Material Stiffness	Vent Diameter (mm)	Inbound Velocity (m/s)	Mean Force (SD) (N)	n	Mean Air Flow Rate (SD) (m/s)	n
TPU 45D	1	Total	3483.36 (3350.49)	90	86.58 (23.40)	90
	2		3586.79 (3596.10)	90	124.29 (26.82)	89
	3		3620.15 (3701.36)	90	142.69 (27.62)	88
	4		4258.01 (4485.57)	90	132.66 (25.28)	90
	5		4728.05 (5051.15)	90	131.17 (37.97)	89
TPU 90A	1	Total	4549.73 (4495.77)	90	105.00 (37.28)	90
	2		4689.84 (4742.33)	90	132.14 (40.88)	90
	3		5968.23 (5510.39)	90	139.60 (28.01)	90
	4		6139.17 (4837.59)	90	148.81 (30.72)	90
	5		6572.23 (5212.42)	90	141.63 (30.69)	90

Table 7. Comparison of mean peak force (N) and air flow rate (m/s) values (with standard deviations) for TPU 45D and TPU 90A chambers with vent diameters ranging from 1-5 mm, across all inbound velocities (1.3, 2.3, 3.0 m/s), where N=900 and N=896.

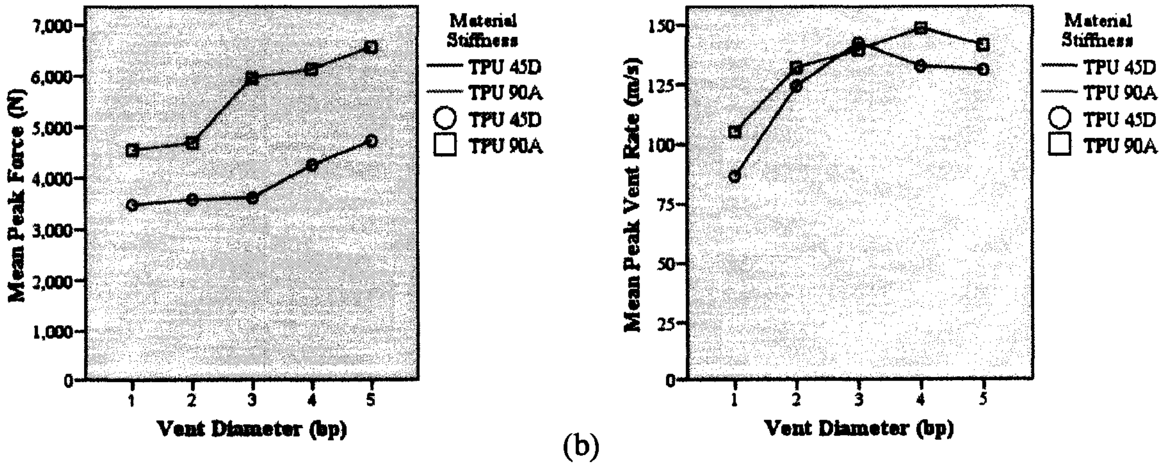

(a) (b)

Figure 26. Comparison of mean peak force (N) (a) and air flow rate (m/s) (b) values for TPU 45D and TPU 90A chambers with vent diameters ranging from 1-5 mm, across all inbound velocities (1.3, 2.3, 3.0 m/s).

Material Stiffness by Inbound Velocity

As shown in Table 8, both TPU 45D and TPU 90A chambers impacted at the lowest inbound velocity, 1.3 m/s, transmitted the least force, followed by chambers impacted at 2.3 m/s, then 3.0 m/s. Thus, at 1.3 m/s the TPU 90A outperformed TPU 45D, however at 2.3 m/s and 3.0 m/s, this relationship reversed. Both the TPU 90A and TPU 45D chambers impacted at 1.3 m/s had the lowest air flow rates, followed by those impacted at 3.0 m/s, then 2.3 m/s, as shown in Table 8. Separate Bonferroni *post hoc* tests were conducted for each material stiffness to determine where significant differences existed in peak force and air flow rates for each vent diameter. Analysis confirmed significance between all inbound velocities for both materials, $p<0.001$.

Material Stiffness	Vent Diameter (mm)	Inbound Velocity (m/s)	Mean Force (SD) (N)	n	Mean Air Flow Rate (SD) (m/s)	n
TPU 45D	Total	1.3	941.11 (45.53)	150	103.91 (22.42)	149
		2.3	1380.23 (211.71)	150	138.86 (43.22)	147
		3.0	9484.47 (1981.41)	150	127.53 (24.39)	150
TPU 90A	Total	1.3	695.88 (45.32)	150	111.31 (20.26)	150
		2.3	3898.84 (1980.61)	150	162.43 (30.91)	150
		3.0	12156.79 (1231.16)	150	126.57 (36.98)	150

Table 8. Comparison of mean peak force (N) and air flow rate (m/s) values (with standard deviations) for TPU 45D and TPU 90A chambers impacted at 1.3, 2.3, and 3.0 m/s, across all vent diameters (1-5 mm), where N=900 (force) and N=896 (air flow rate).

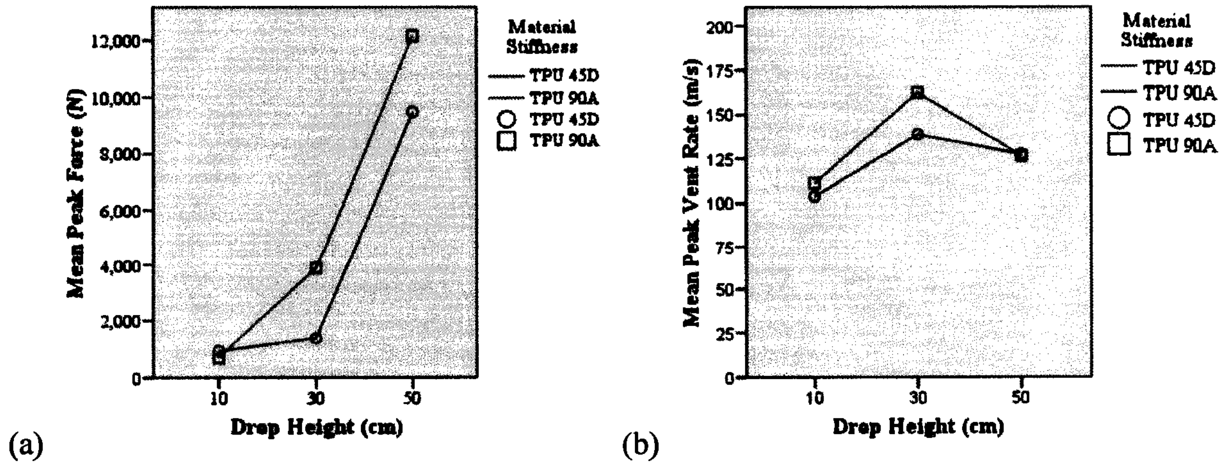

Figure 27. Comparison of mean peak force (N) (a) and air flow rate (m/s) (b) values for TPU 45D and TPU 90A chambers impacted at 1.3, 2.3, and 3.0 m/s, across all vent diameters (1-5 mm).

Vent Diameter by Inbound Velocity

As shown in Table 9, at 1.3 m/s, it was determined that the 1 mm vent diameter transmitted the most force followed by 2, 3, 4 , then 5 mm vents. At 2.3 m/s, it was determined that the 2 mm vent transmitted the least amount of force, followed by 1, 3, 4, then 5 mm. At 3.0 m/s, it was determined that the 1 mm vent transmitted the least force followed by 2, 3, 4, 5 mm. Separate Bonferroni *post hoc* tests were conducted for each of the three inbound velocities which revealed that at 1.3 m/s, significant differences in peak force occurred between all vents, $p<0.01$, except between 1, 2 mm and 4, 5 mm vents. Thus, at 1.3 m/s, the smallest vent resulted in the highest peak force measurement, while the largest vent resulted in the lowest peak force measurement. At 2.3 m/s, all differences were significant at $p<0.001$, with the exception of between 1, 2 mm and 4, 5 mm vents. At 3.0 m/s, all differences were significant at $p<0.001$, with the exception of between 1, 2 mm and 3, 4 mm. Thus, at 3.0 m/s, the smallest force transmitted the least amount of force, while the largest vent transmitted the most.

As shown in Table 9, at an inbound velocity of 1.3 m/s it was determined that the 1 mm vent had the lowest air flow rate, followed by 5, then 2, 4, and 3 mm vent diameters. At 2.3 m/s, it was determined that the 1 mm had the lowest air flow rate, followed by 2, 5, 4, then 3 mm. At 3.0 m/s, the 2 mm had the lowest air flow rate followed by 1, 3, 4, 5 mm. Separate Bonferroni *post hoc* tests were conducted for each of the three inbound velocities, to determine where significant differences existed in the peak air flow rate for each vent diameter of both material stiffnesses. At 1.3 m/s all differences were significant at $p<0.05$, except between 2, 4 mm and 3, 4 mm. At 2.3 m/s, differences were only significant between 1 and 2, 3, 4, 5 mm at $p<0.001$. All other differences were not significant. At 3.0 m/s, differences were significant at $p<0.01$, except for between 1, 2 mm; 3, 4 mm; and 4, 5 mm.

Material stiffness	Vent Diameter (mm)	Inbound Velocity (m/s)	Mean Force (SD) (N)	n	Mean Air Flow Rate (SD) (m/s)	n
Total	1	1.3	860.549 (180.36)	60	74.45 (15.97)	60
	2		848.410 (135.31)	60	116.56 (16.97)	59
	3		812.160 (126.75)	60	122.37 (12.42)	60
	4		790.984 (120.47)	60	120.98 (4.26)	60
	5		780.379 (145.74)	60	103.88 (6.30)	60
Total	1	2.3	1782.468 (460.50)	60	100.60 (30.84)	60
	2		1703.777 (538.64)	60	158.78 (22.69)	60
	3		2502.552 (1504.21)	60	171.73 (23.18)	58
	4		3437.294 (2237.38)	60	163.68 (35.31)	60
	5		3771.578 (2589.58)	60	159.87 (34.83)	59
Total	1	3.0	9406.615 (1821.01)	60	112.32 (34.80)	60
	2		9862.753 (1921.78)	60	109.18 (37.25)	60
	3		11067.847 (2627.71)	60	130.30 (15.63)	60
	4		11367.484 (1311.57)	60	137.55 (19.46)	60
	5		12398.457 (1149.56)	60	145.93 (26.52)	60

Table 9. Comparison of mean peak force (N) and air flow rate (m/s) values (with standard deviations) for chambers with vent diameters ranging from 1-5 mm impacted at 1.3, 2.3, and 3.0 m/s, across both material stiffnesses (TPU 45D and TPU 90A), where N=900 (force) and N=896 (air flow rate).

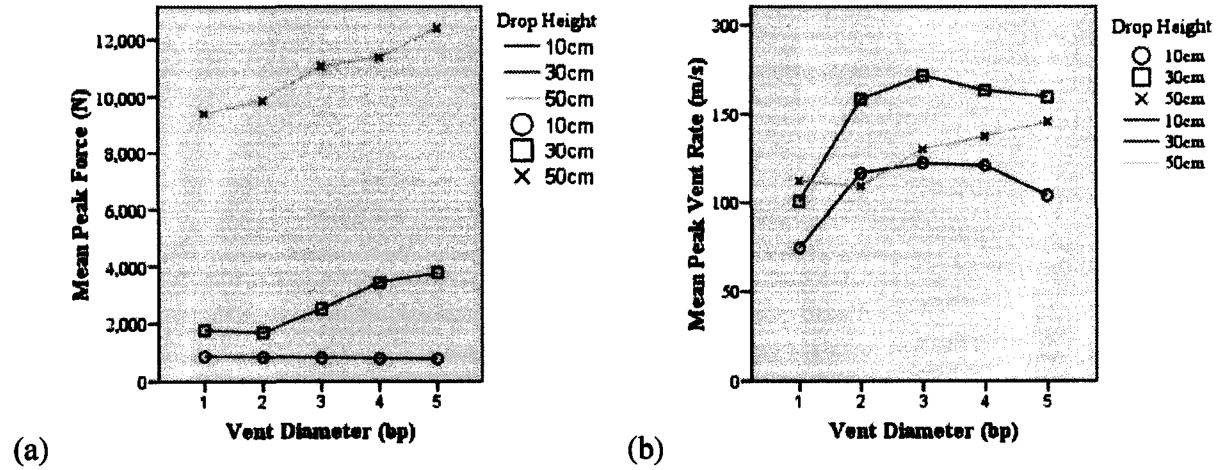

Figure 28. Comparison of mean peak force (N) (a) and air flow rate (m/s) (b) values for chambers with vent diameters ranging from 1-5 mm impacted from 1.3, 2.3, and 3.0 m/s, across both material stiffnesses (TPU 45D and TPU 90A).

4.2.1.3. Three-Way Interactions

Material Stiffness by Vent Diameter by Inbound Velocity

As is evident in Figure 29 and Figure 30, significant three-way interactions existed between the independent variables and peak force and peak air flow rates. The lines on the graph deviate from parallel, supporting the statistical finding that a significant three-way interaction existed between material stiffness, vent diameter, and inbound velocity (George & Mallery, 2007). The effect size indicated that 31.9% of the variance in peak force and that 4.0% of the variation in air flow rates was accounted for by these two three-way interactions.

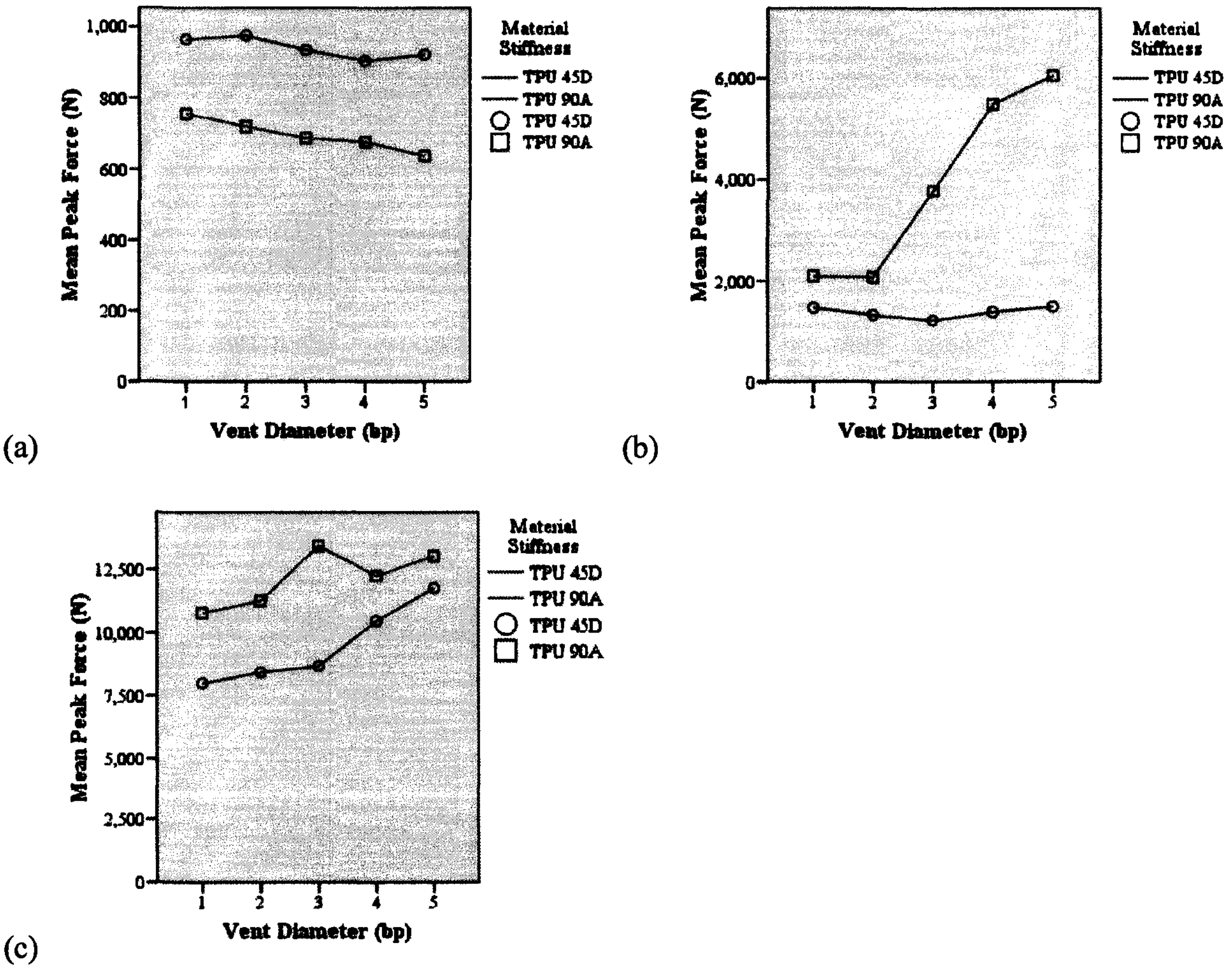

Figure 29. Comparison of mean peak force values (N) for TPU 45D and TPU 90A chambers with vent diameters ranging from 1-5 mm impacted from (a) 1.3 m/s, (b) 2.3 m/s, and (c) 3.0 m/s.

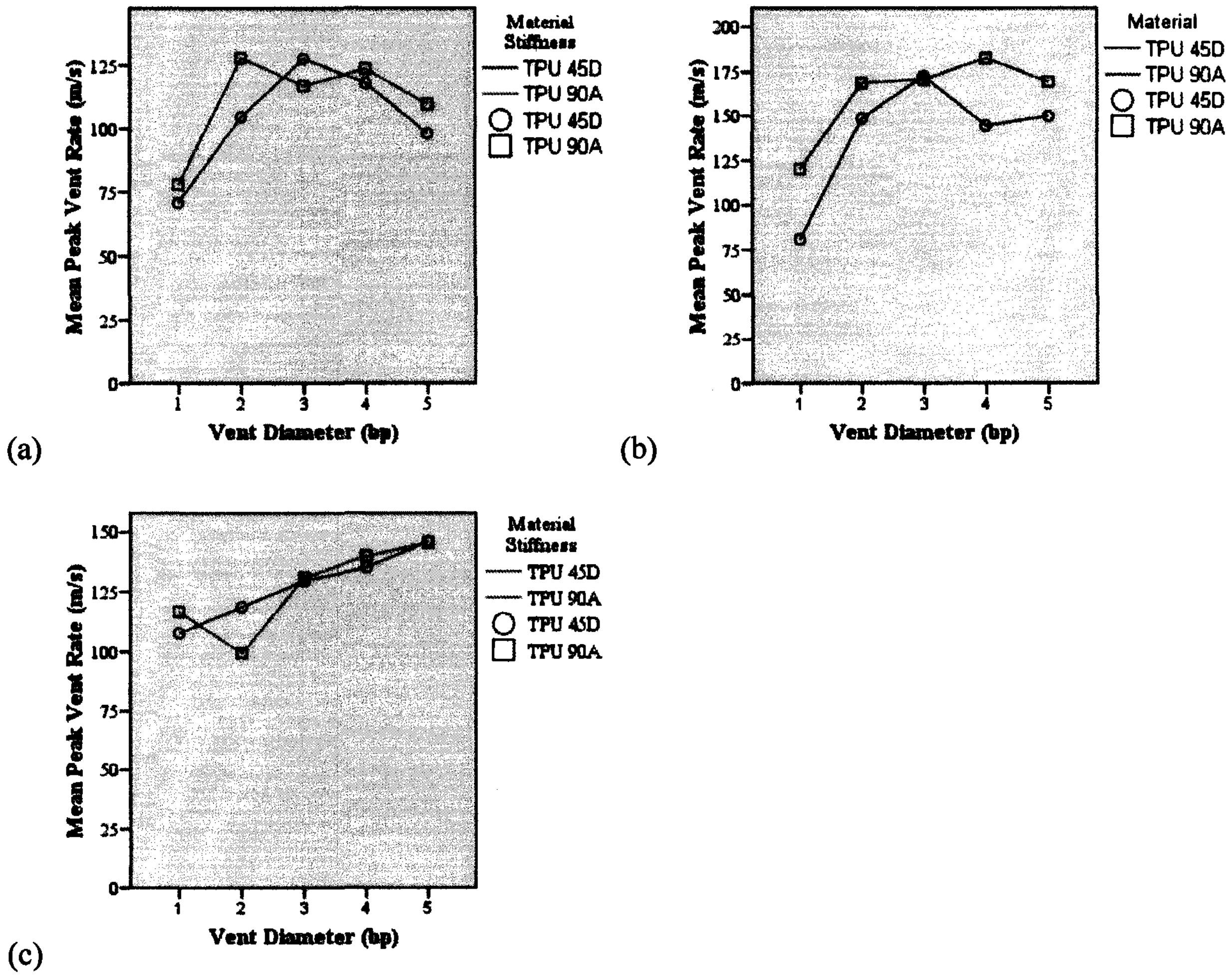

Figure 30. Comparison of mean air flow rate values (m/s) for TPU 45D and TPU 90A chambers with vent diameters ranging from 1-5 mm impacted from (a) 1.3 m/s, (b) 2.3 m/s, and (c) 3.0 m/s.

4.2.2. Part B

Upon analysis of the above data, it was determined that the small vents performed significantly better than the large vents at high inbound velocities. Upon these findings, a no-venting condition was added to the study to determine if non-vented chambers perform better than vented chambers at high velocities. It was hypothesized that the non-vented chambers would outperform chambers with vents when impacted at high inbound velocities and this relationship would reverse at low inbound velocities.

Originally, the no-venting condition was to be added to the study and compared to the Part A data. Upon impacting a pilot series of chambers and comparing the results to Part A data, slight differences in the force traces appeared, possibly due to variations in chamber performance under different lab conditions (heat and humidity variations). Since the influence of environmental conditions on chambers has yet to be studied, a new series of chambers was tested. This data collection consisted of three sets of TPU 45D and TPU 90A; 1.3, 2.3, and 3.0 m/s inbound velocities; 0 to 5 mm vent diameters; five trials per chamber. It was felt that only five trials were needed to establish the relationship under investigation. Air flow was not measured.

A between subjects design was used to examine the mean peak force (N) values for all possible combinations of material stiffness (hard – TPU 45D and soft – TPU 90A), vent diameter (1-5 mm) and impact inbound velocity (1.3, 2.3, 3.0 m/s). The mean peak force values are shown in Table 10.

Material Stiffness	Vent Diameter (mm)	Inbound Velocity (m/s)	Mean (SD) (N)	n
TPU 45D	0	1.3	911.01 (112.05)	15
	1		887.72 (112.13)	15
	2		885.20 (125.01)	15
	3		885.77 (143.44)	15
	4		858.07 (145.41)	15
	5		881.03 (17.71)	15
TPU 45D	0	2.3	1772.45 (455.60)	15
	1		1755.13 (452.52)	15
	2		1682.11 (587.18)	14
	3		2072.61 (1270.90)	15
	4		2581.88 (1424.54)	15
	5		1327.73 (55.95)	15
TPU 45D	0	3.0	8068.78 (2025.20)	15
	1		8309.54 (1752.49)	15
	2		8289.00 (2315.54)	15
	3		9165.95 (2237.74)	15
	4		9678.60 (1415.21)	15
	5		9358.80 (1376.66)	15
TPU 90A	0	1.3	833.26 (118.21)	15
	1		837.00 (116.59)	15
	2		761.63 (81.59)	14

	3		774.95 (146.11)	15
	4		723.95 (114.79)	15
	5		635.47 (19.12)	15
TPU 90A	0	2.3	2062.22 (490.48)	15
	1		2016.53 (322.58)	15
	2		2205.44 (727.03)	15
	3		2651.10 (1135.85)	15
	4		4517.05 (644.95)	15
	5		4665.07(610.92)	15
TPU 90A	0	3.0	8578.87 (2090.97)	15
	1		9041.66 (1873.95)	15
	2		9218.09 (1823.51)	15
	3		10909.69 (1653.12)	15
	4		12319.03 (1062.62)	15
	5		12999.38 (1098.78)	15

Table 10. Comparison of mean peak force values (N) (with standard deviations) for TPU 45D and TPU 90A chambers with various vent diameters (0-5 mm), impacted from 3 inbound velocities (1.3, 2.3, 3.0 m/s), where N=538.

Data were analyzed using a 3-way ANOVA - 2 x 6 x 3 design (material stiffness by vent diameter by inbound velocity). Levene's test of equality of error variance indicated F(35, 502)=15.90, $p<0.05$; however, upon analysis it was determined that skewness and kurtosis were 0.847 and -0.790 respectively. Since both skewness and kurtosis were within ± 1.96, normality of the data was assumed.

Results showed very significant main effects of material stiffness, F(1, 502)=88.31, $p<0.001$, partial η^2=0.150, vent diameter, F(5, 502)=27.63 $p<0.001$, partial η^2=0.216, and inbound velocity, F(2, 502)=3155.13, $p<0.001$, partial η^2=0.926, on peak force. In addition, there were very significant interactions between material stiffness and vent diameter, F(5, 502)=11.25, $p<0.001$, partial η^2=0.101, material stiffness and inbound velocity, F(2, 502)=31.14, $p<0.001$, partial η^2=0.110, vent diameter and inbound velocity, F(10, 502)=10.40, $p<0.001$, partial η^2=0.172, and material stiffness, vent diameter, and inbound velocity, F(10, 502)=3.448, $p<0.001$, partial η^2=0.064.

The observed power for all main effects and interactions for peak force was 1.0, except for the interaction between material stiffness, vent diameter, and inbound velocity (0.993). Each main effect of the independent variables on peak force and the interaction between the independent variables on peak force was further analyzed and will be considered separately in the following analysis.

4.2.2.1. Main Effects

Material Stiffness

Analysis revealed that 269 impacts of TPU 45D resulted in lower peak force transmission than TPU 90A (see Table 11).

Material Stiffness	Vent Diameter (mm)	Inbound Velocity (m/s)	Mean (SD) (N)	n
TPU 45D	Total	Total	3862.10 (3749.08)	269
TPU 90A			4778.79 (4453.75)	269

Table 11. Comparison of mean peak force values (N) (with standard deviations) for TPU 45D and TPU 90A chambers, across all vent diameters (1-5 mm) and inbound velocities (1.3, 2.3, 3.0 m/s), where N=538.

Vent Diameter

Results indicated the 0 mm vent diameter transmitted the least force, followed by 1, 2, 3, 5, and 4 mm vents (see Table 12). Further analysis using the Bonferroni *post hoc* test, $p<0.05$, was used to determine where significant differences existed in the force transmitted by chambers with different vent diameters. Significant differences were found between all vent diameters except between 0, 1, 2 mm vents as well as between 4, 5 mm vents. Thus, the smaller vents (0, 1, 2 mm) transmitted significantly less force than the larger vents (4, 5 mm).

Material Stiffness	Vent Diameter (mm)	Inbound Velocity (m/s)	Mean (SD) (N)	n
Total	0	Total	3704.44 (3522.85)	90
	1		3807.93 (3646.38)	90
	2		3899.93 (3765.06)	88
	3		4410.01 (4286.73)	90
	4		5113.10 (4537.09)	90
	5		4977.91 (4784.92)	90

Table 12. Comparison of mean peak force values (N) (with standard deviations) for chambers with vent diameters ranging from 1-5 mm, across both material stiffnesses (TPU 45D and TPU 90A) and inbound velocities (1.3, 2.3, 3.0 m/s), where N=538.

Inbound Velocity

As indicated in Table 13, chambers impacted at 1.3 m/s transmitted the least force, followed by chambers impacted at 2.3 m/s, then 3.0 m/s. Further analysis using the Bonferroni *post hoc* test, $p<0.001$, confirmed significance between all inbound velocities.

Material Stiffness	Vent Diameter (mm)	Inbound Velocity (m/s)	Mean (SD) (N)	n
Total	Total	1.3	823.27 (135.16)	179
		2.3	2446.69 (1277.72)	179
		3.0	9661.53 (2303.17)	180

Table 13. Comparison of mean peak force values (N) (with standard deviations) for chambers impacted at 1.3, 2.3, and 3.0 m/s, across all vent diameters (1-5mm) and material stiffnesses (TPU 45D and TPU 90A), where N=538.

4.2.2.2. Two-Way Interactions

Material Stiffness by Vent Diameter

As shown in Table 14, both material stiffnesses resulted in the 0 mm vent transmitting the least force, followed by 1, 2, 3, 4, and 5 mm vent diameters. Separate Bonferroni *post hoc* tests were conducted for each material stiffness to determine where significant differences existed in the peak force transmitted by each vent diameter. For the TPU 45D material, significant differences occurred only between 0, 4 mm vent diameters, $p<0.05$. For the TPU 90A, significant differences existed at $p<0.01$ between all vent combinations with the exception of 0, 1, 2 mm; 2, 3 mm; and 4, 5 mm.

Material Stiffness	Vent Diameter (mm)	Inbound Velocity (m/s)	Mean (SD) (N)	n
TPU 45D	0	Total	3584.09 (3433.11)	45
	1		3650.80 (3503.31)	45
	2		3663.13 (3645.89)	44
	3		4041.44 (3972.73)	45
	4		4372.85 (4023.87)	45
	5		3855.85 (4015.40)	45
TPU 90A	0	Total	3824.78 (3645.14)	45
	1		3965.06 (3817.16)	45
	2		4136.72 (3908.15)	44
	3		4778.58 (4594.48)	45
	4		5853.34 (4932.12)	45
	5		6099.97 (5254.77)	45

Table 14. Comparison of mean peak force values (N) (with standard deviations) for TPU 45D and TPU 90A chambers with vent diameters ranging from 1-5 mm, across all inbound velocities (1.3, 2.3, 3.0 m/s), where N=538.

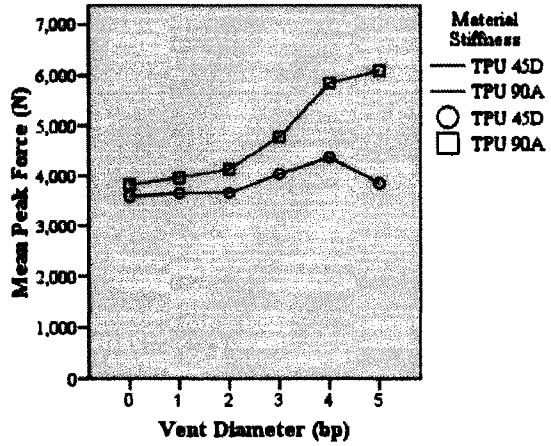

Figure 31. Comparison of mean peak force values (N) for TPU 45D and TPU 90A chambers with vent diameters ranging from 1-5 mm, across all inbound velocities (1.3, 2.3, 3.0 m/s).

Material Stiffness by Inbound Velocity

Analysis of the interaction between material stiffness and inbound velocity indicated chambers impacted at 1.3 m/s transmitted the least force followed by 2.3 m/s and 3.0 m/s, for both materials (see Table 15). Further analysis using a Bonferroni *post hoc* test, $p<0.001$, confirmed significance between all inbound velocities.

Material Stiffness	Vent Diameter (mm)	Inbound Velocity (m/s)	Mean (SD) (N)	n
TPU 45D	Total	1.3	884.81 (115.17)	90
		2.3	1867.38 (921.86)	89
		3.0	8811.94 (1937.06)	90
TPU 90A	Total	1.3	761.04 (125.49)	89
		2.3	3019.57 (1325.66)	90
		3.0	10511.12 (2335.97)	90

Table 15. Comparison of mean peak force values (N) (with standard deviations) for TPU 45D and TPU 90A chambers impacted at 1.3, 2.3, and 3.0 m/s, across all vent diameters (1-5 mm), where N=538.

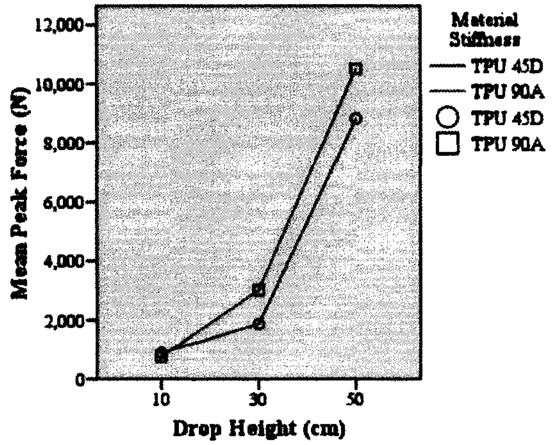

Figure 32. Comparison of mean peak force values (N) for TPU 45D and TPU 90A chambers impacted at 1.3, 2.3, and 3.0 m/s, across all vent diameters (1-5 mm).

Vent Diameter by Inbound Velocity

Analysis revealed at 1.3 m/s, the chamber containing a 5 mm vent transmitted the least peak force followed by 4, 2, 3, 1, and 0 mm vents. At 2.3 m/s, the 1 mm transmitted the least force, followed by 0, 2, 3, 5, and 4 mm. At 3.0 m/s, the 0 mm transmitted the least force followed by 1, 2, 3, 4, 5 mm vent diameters. Separate Bonferroni *post hoc* tests were conducted for each of the three inbound velocities which revealed that at 1.3 m/s, significant differences existed only between 0, 5 mm and 1, 5 mm , $p<0.01$. At 2.3 m/s, significant differences existed between all vent combinations except between 0, 1, 2, 3 mm and 4, 5 mm, $p<0.05$. At 3.0 m/s, significant differences also existed between all vent combinations except between 0, 1, 2 mm and 4, 5 mm, $p<0.05$.

Material stiffness	Vent Diameter (mm)	Inbound Velocity (m/s)	Mean (SD) (N)	n
Total	0	1.3	872.16	30
	1		862.36	30
	2		825.55	29
	3		830.36	30
	4		791.01	30
	5		758.25	30
Total	0	2.3	1917.33	30
	1		1885.83	30
	2		1952.80	29
	3		2361.85	30
	4		3549.47	30
	5		2996.40	30
Total	0	3.0	8323.82	30
	1		8675.60	30
	2		8754.04	30
	3		10037.82	30
	4		10998.81	30
	5		11179.09	30

Table 16. Comparison of mean peak force values (N) (with standard deviations) for chambers with vent diameters ranging from 1-5 mm impacted at 1.3, 2.3, and 3.0 m/s, across both material stiffnesses (TPU 45D and TPU 90A), where N=538.

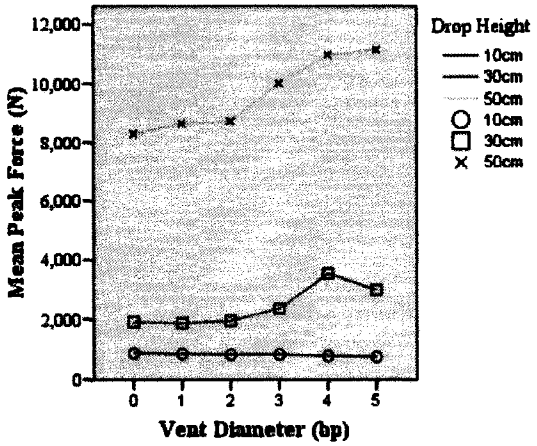

Figure 33. Comparison of mean peak force values (N) for chambers with vent diameters ranging from 1-5 mm impacted at 1.3, 2.3, and 3.0 m/s, across both material stiffnesses (TPU 45D and TPU 90A).

4.2.2.3. Three-Way Interactions

Material Stiffness by Vent Diameter by Inbound Velocity

As is evident in Figure 34, a significant three-way interaction existed between the independent variables. The effect size indicated that 6.2% of the variance in peak force is accounted for by this three-way interaction.

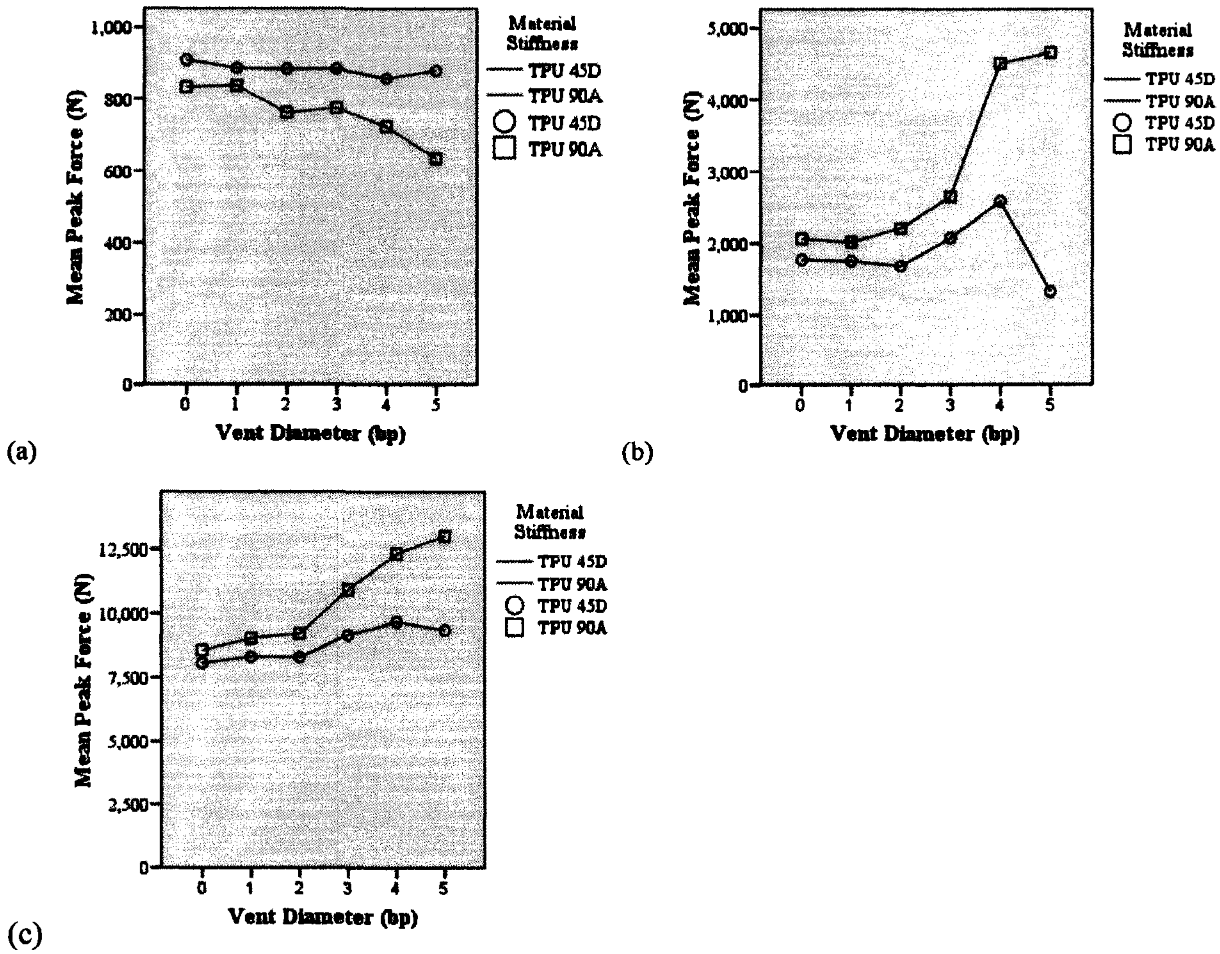

Figure 34. Comparison of mean peak force values (N) for TPU 45D and TPU 90A chambers with vent diameters ranging from 1-5 mm impacted at (a) 1.3 m/s, (b) 2.3 m/s, and (c) 3.0 m/s.

4.2.3. Part A & B Chamber Performance Comparison

	Part A	Part B
Material Stiffness	TPU 45D, TPU 90A	TPU 45D, TPU 90A
Vent Diameter	1, 2, 3, 4, 5 mm	0, 1, 2, 3, 5, 4 mm
Inbound Velocity	1.3, 2.3, 3.0 m/s	1.3, 2.3, 3.0 m/s
Material by Vent Diameter	TPU 45D: 1, 2, 3, 4, 5 mm TPU 90A: 1, 2, 3, 4, 5 p	TPU 45D: 0, 1, 2, 5, 3, 4 mm TPU 90A: 0, 1, 2, 3, 4, 5 mm
Material by Inbound Velocity	1.3 m/s, 2.3 m/s, 3.0 m/s	1.3 m/s, 2.3 m/s, 3.0 m/s
Vent Diameter by Inbound Velocity	1.3 m/s: 5, 4, 3, 2, 1 mm 2.3 m/s: 2, 1, 3, 4, 5 mm 3.0 m/s: 1, 2, 3, 4, 5 mm	1.3 m/s: 5, 4, 2, 3, 1, 0 mm 2.3 m/s: 1, 0, 2, 3, 5, 4 mm 3.0 m/s: 0, 1, 2, 3, 4, 5 mm

Table 17. Comparison of chamber performance (lowest, highest mean peak force), in Parts A and B.

	Part A	Part B
Material Stiffness	All Significant	All significant
Vent Diameter	1, 2 mm	0, 1, 2 mm 4, 5 mm
Inbound Velocity	All significant	All significant
Material by Vent Diameter	TPU 45D: 1, 2 mm 1, 3 mm 2, 3 mm TPU 90A: 1, 2 mm 3, 4 mm 4, 5 mm	TPU 45D: Only – 0, 4 mm significant TPU 90A: 0, 1, 2 mm 2, 3 mm 4, 5 mm
Material by Inbound Velocity	All significant	All significant
Vent Diameter by Inbound Velocity	1.3 m/s: 1, 2 mm 4, 5 mm 2.3 m/s: 1, 2 mm 4, 5 mm 3.0 m/s: 1, 2 mm 3, 4 mm	1.3 m/s: Only 0, 5 mm 1, 5 mm 2.3 m/s: 0, 1, 2, 3 mm 4, 5 mm 3.0 m/s: 0, 1, 2 mm 4, 5 mm

Table 18. Comparison of significance findings in Parts A and B. Chambers listed are the non-significant findings unless otherwise indicated.

4.2.4. Multiple Impact Performance

Results of the trial effect analysis using Part A data, indicated that there was a very significant main effect of trial number on peak force, F(9, 600)=53.71, $p<0.001$, a very significant two-way interaction between trial number and inbound velocity, F(18, 600) = 19.649, $p<0.001$, and a very significant three-way interaction between trial number, inbound velocity, and material stiffness, F(18, 600)=11.026, $p<0.001$. Mean peak force values for each trial, across all material stiffnesses and inbound velocities, are presented in Table 19.

Trial	Mean Force (SD) (N)	n
1	3756.38 (3874.43)	90
2	4364.23 (4414.81)	90
3	4597.49(4563.68)	90
4	4757.92(4664.95)	90
5	4858.78(4731.38)	90
6	4951.21(4785.87)	90
7	4996.84(4816.13)	90
8	5045.98(4863.50)	90
9	5135.23(4883.47)	90
10	5131.48(4874.42)	90

Table 19. Comparison of mean peak force values (N) (with standard deviations) for each trial (1-10) across both material stiffnesses (TPU 45D and TPU 90A), all vent diameters (1-5 mm), and inbound velocities (1.3, 2.3, 3.0 m/s), where N=900.

These results indicated the energy attenuation ability of the chambers was significantly reduced with each impact, across all material stiffnesses, vent diameters, and inbound velocities.

Trial by Inbound Velocity

Analysis of the two-way interaction between trial and inbound velocity indicated at 1.3 m/s, energy attenuation improved with subsequent impacts, whereas at 2.3 and 3.0 m/s, energy attenuation ability decreased with each impact.

Material Stiffness	Vent Diameter (mm)	Inbound Velocity (m/s)	Trial	Mean Force (SD) (N)	n
Total	Total	1.3	1	839.53 (131.00)	30
			2	833.35 (132.93)	30

			3	825.26 (131.95)	30
			4	820.75 (131.52)	30
			5	816.27 (132.16)	30
			6	814.38 (132.41)	30
			7	811.68 (132.42)	30
			8	809.70 (130.86)	30
			9	808.72 (134.83)	30
			10	805.33 (134.85)	30
Total	Total	2.3	1	1778.14 (1069.07)	30
			2	2113.32 (1293.07)	30
			3	2374.09 (1580.51)	30
			4	2572.39 (1777.80)	30
			5	2693.31 (1912.57)	30
			6	2827.28 (2027.88)	30
			7	2870.64 (2039.82)	30
			8	2926.82 (2186.11)	30
			9	3097.40 (2204.01)	30
			10	3141.95 (2227.07)	30
Total	Total	3.0	1	8651.48 (2696.45)	30
			2	10146.02 (2325.05)	30
			3	10593.13 (2093.00)	30
			4	10880.62 (1962.42)	30
			5	11066.74 (1844.55)	30
			6	11211.97 (1801.30)	30
			7	11308.21 (1733.05)	30
			8	11401.42 (1673.65)	30
			9	11499.58 (1658.95	30
			10	11447.15 (1794.88)	30

Table 20. Comparison of mean peak force values (N) (with standard deviations) for each trial (1-10) at 1.3, 2.3, and 3.0 m/s, across all vent diameters (1-5 mm) and both material stiffnesses (TPU 45D and TPU 90A), where N=900.

Further analysis of the significant three-way interaction between trial number, inbound velocity, and material showed that for both TPU 45D and TPU 90A materials, peak force decreased with increased impacts at 1.3 m/s. At 2.3 m/s and 3.0 m/s, peak force increased with subsequent impacts for both materials. *Post hoc* analysis using the Bonferroni test, $p<0.05$, indicated that significant differences existed between all trial numbers with the exception of vent combinations: 2 and 3 mm; 2 and 4-6 mm; 3 and 4-7 mm; 4 and 3, 4-7 mm; 5 and 3-8 mm; 6 and 4-10 mm; 7 and 4-10 mm; 8 and 5-10 mm; 9 and 6-10 mm; 10 and 6-9 mm. Separate

Bonferroni *post hoc* tests were also conducted for each inbound velocity and testing showed significant differences existed between all trials except those shown in Table 21.

1.3 m/s	2.3 m/s	3.0 m/s
Only between	1 and 2	2 and 3
1 and 8-10	2 and 1, 3-4	3 and 4-6
	3 and 2, 4-6	4 and 3-10
	4 and 2-8	5 and 3-10
	5 and 3-10	6 and 3-10
	6 and 3-10	7 and 4-10
	7 and 4-10	8 and 4-10
	8 and 4-10	9 and 4-10
	9 and 5-10	10 and 4-9
	10 and 5-9	

Table 21. Non-significant differences, unless otherwise indicated, in mean peak force values (N) for TPU 45D and TPU 90A impacted at 1.3, 2.3, and 3.0 m/s.

4.2.5. Force and Air Flow Velocity Curves

4.2.5.1. Part A

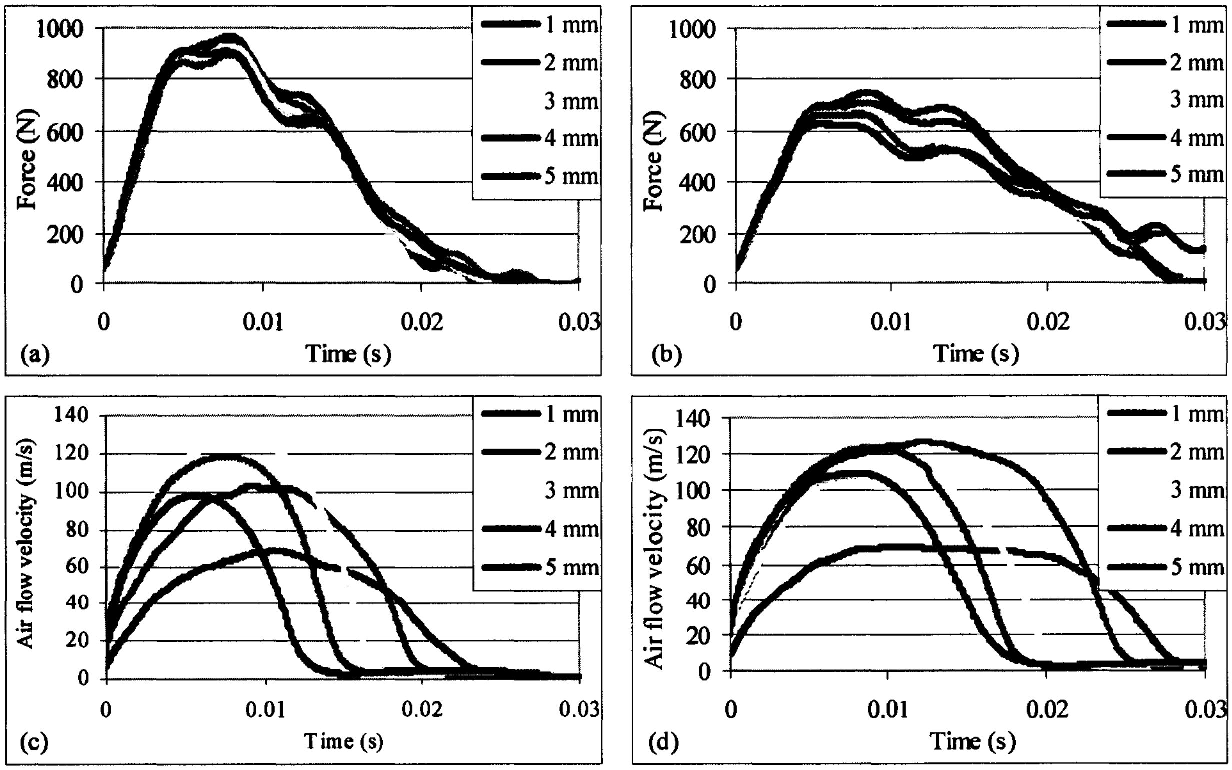

Figure 35. TPU 45D (a, c) and TPU 90A (b, d) force-time curves of chambers with vent diameters ranging from 1-5 mm, impacted at 1.3 m/s with corresponding air flow velocity curves.

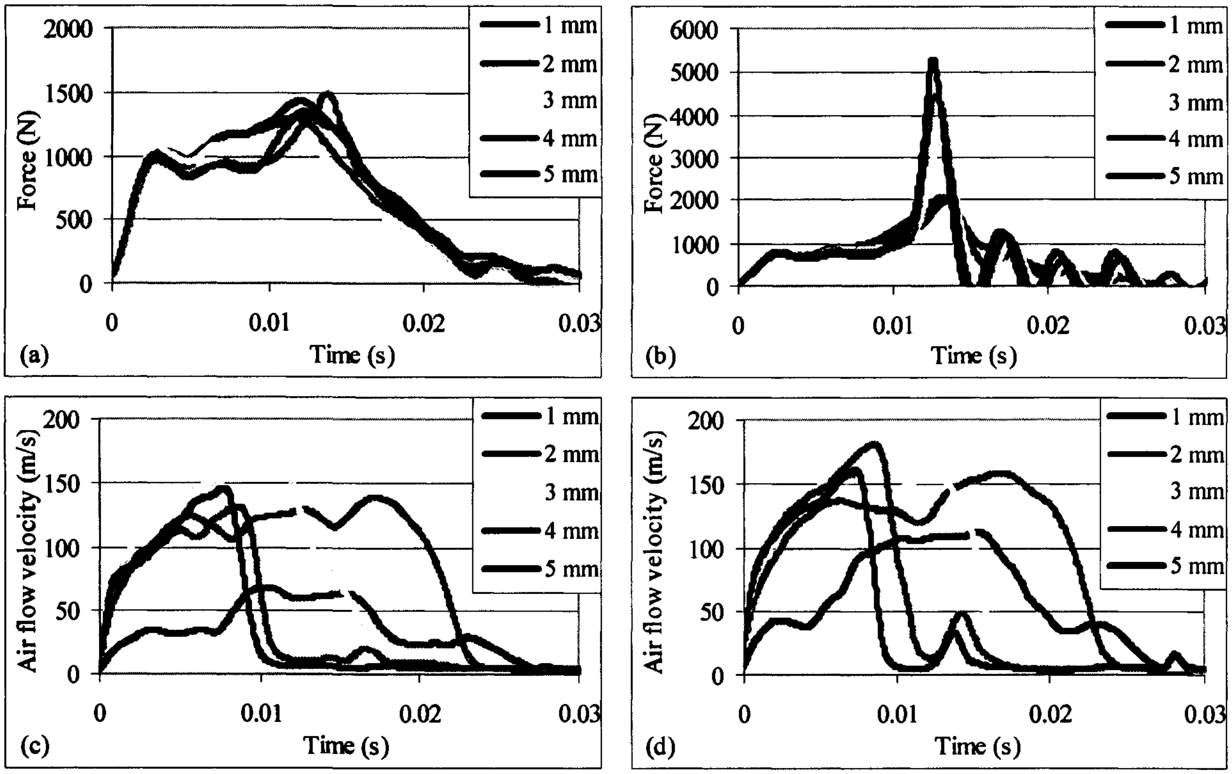

Figure 36. TPU 45D (a, c) and TPU 90A (b, d) force-time curves of chambers with vent diameters ranging from 1-5 mm, impacted at 2.3 m/s with corresponding air flow velocity curves.

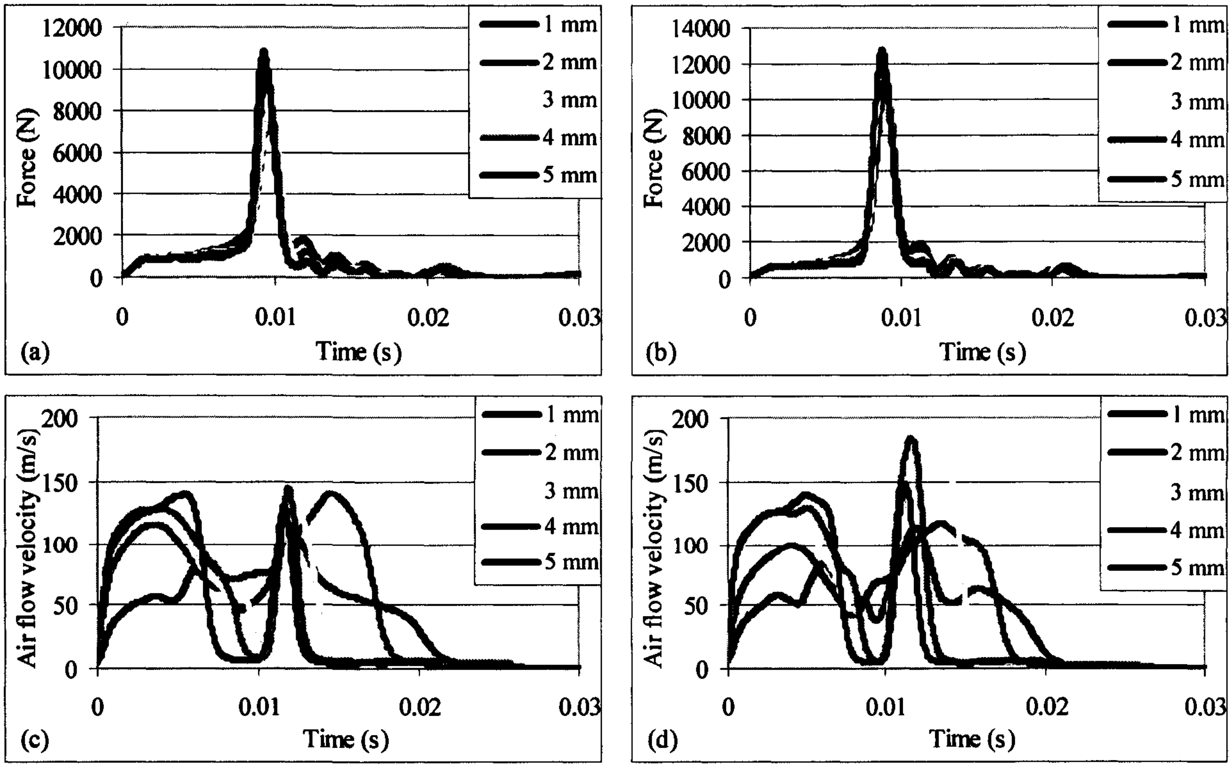

Figure 37. TPU 45D (a, c) and TPU 90A (b, d) force-time curves of chambers with vent diameters ranging from 1-5 mm, impacted at 3.0 m/s with corresponding air flow velocity curves.

4.2.5.2. Part B

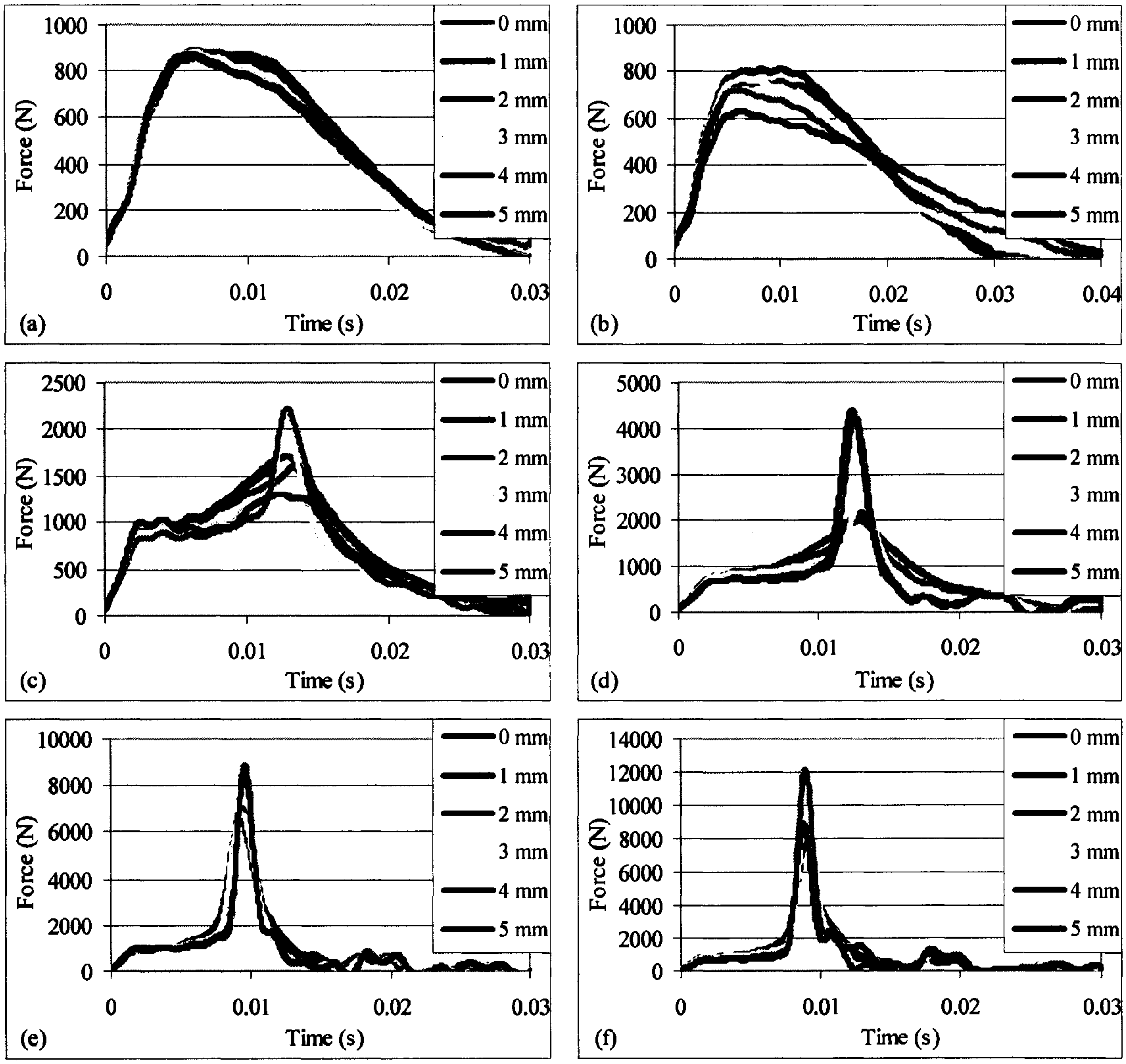

Figure 38. TPU 45D (a, c, e) and TPU 90A (b, d, f) force-time curves of chambers with vent diameters ranging from 1-5 mm, impacted at 1.3 m/s (a, b), 2.3 m/s (c, d) and 3.0 m/s (e, f).

4.2.6. Correlational Analysis

Pearson's correlational analysis was performed to determine the relationship between peak force and peak air flow rate as well as peak force and air flow duration. All correlation results are summarized in Table 22. Analysis at each inbound velocity separately yielded a strong, negative correlation between peak force and peak air flow rate at 1.3 m/s for TPU 45D, r(149)=-0.517, $p<0.001$, and TPU 90A, r(150)=-0.424, $p<0.001$. A significant relationship existed between peak force and vent rate at 2.3 m/s for TPU 45D, r(147)=-.324, $p<0.001$, and TPU 90A, r(150)=0.309, $p<0.001$. At 3.0 m/s, a small positive relationship for peak force and vent rate existed for both materials: TPU 45D, r(150)=0.185, $p<0.05$, TPU 90A, r(150)=0.198, $p<0.05$. Thus, at 1.3 m/s, as air flow rates decreased for both material stiffnesses, peak force increased. At 2.3 m/s, for TPU 45D, as vent rate decreased, peak force increased, whereas for TPU 90A, as vent rate increased, peak force increased. At 3.0 m/s, as vent rate increased for both material stiffnesses, peak force also increased.

Further analysis of air flow results yielded a significant, strong, positive correlation between peak force and air flow duration at 1.3 m/s for TPU 45D, r(150)=0.451, $p<0.01$, and TPU 90A, r(150)=0.818, $p<0.001$. A significant, strong negative correlation existed between peak force and air flow duration at 2.3 m/s for TPU 90A, r(150)=-0.809, $p<0.001$. No significant correlation existed between peak force and air flow duration for TPU 45D at 2.3 m/s. At 3.0 m/s, a significant, strong, negative correlation existed between peak force and air flow duration for TPU 45D, r(150)=-0.619, $p<0.001$, and TPU 90A, r(150)=-0.794, $p<0.001$. Thus, at 1.3 m/s, for both material stiffnesses, as air flow duration increased, peak force also increased. At 2.3 m/s, as air flow duration decreased for the TPU 90A chambers, peak force increased. At 3.0 m/s, as air flow duration decreased for both material stiffnesses, peak force also increased.

Inbound Velocity	Material Stiffness	Peak Air Flow Rate	Air Flow Duration
1.3 m/s	TPU 45D	-0.517	+0.421
	TPU 90A	-0.424	+0.818
2.3 m/s	TPU 45D	-0.324	none
	TPU 90A	+0.309	-0.809
3.0 m/s	TPU 45D	+0.185	-0.619
	TPU 90A	+0.198	-0.794

Table 22. Summary of the relationship between vent rate/air flow duration and peak force, using Pearson's correlation.

4.2.7. Chamber Testing

4.2.7.1. Chamber Characteristics

All biopsy punches were confirmed to be the diameter indicated by the manufacturer and all chamber wall thicknesses were 2.0 mm. Results of durometer testing indicated that the "TPU 45D" chambers, as indicated by the manufacturer, ranged in hardness from 39.40 to 46.40D, with an average of 42.00D and the "TPU 90A" chambers ranged in hardness from 76.10 to 89.40A, with an average of 83.98A. Thus, despite manufacturing claims that the durometer of the chambers were within ± 3, this was not supported by the TPU 90A findings. As well, the TPU 45D chambers ranged in mass from 17.08 to 17.70 g, with an average of 17.47 g, while the TPU 90A chambers ranged in mass from 17.24 to 17.51 g, with an average of 17.34 g. Therefore, the mean mass of the chambers was 17.41 g.

4.2.7.2. Temperature

Upon impact, the chambers' temperature changed minimally between trials, with temperatures varying from 21.6°C to 22.3°C.

CHAPTER 5. DISCUSSION

From the results presented in Chapter 4, it is apparent that all main factors (material stiffness, vent diameter and inbound velocity) had a significant influence on the mechanical response of energy attenuation and resulting force-time curves. Consequently, to define the chambers' ability to manage impact energy these factors will all be considered. It should be noted that durometer testing indicated the composition of the chambers was not entirely consistent. Thus, slight differences in energy absorption *may* be accounted for by the material composition.

5.1. Vent Diameter

Across all inbound velocities and material stiffnesses, the chambers with the smallest vent diameters (1-2 mm in Part A and 0-3 mm in Part B) absorbed significantly more energy than those with larger vents. By minimizing the air expelled from within, the chambers were able to engage both the material and air as energy absorber mechanisms. In contrast to the smaller vents, the larger vents resulted in more air expulsion, decreasing the amount of air left within the chamber to act as an energy absorber, thereby transmitting more force.

Vent by Inbound Velocity

Similar trends were found between both TPU material stiffnesses at each inbound velocity, however, the peak force differences between vent diameters were much smaller at 1.3 m/s. Under low impact velocities, 1.3 m/s, the chambers with the largest vent diameters outperformed the chambers with the smaller vents. In Part A of the study, the largest vents (4, 5 mm) transmitted the lowest amount of force under low impact velocities, while the smallest vents (1, 2 mm) transmitted the most force. This effect was more pronounced with the TPU 90A material, as the TPU 45D material was too hard to see large differences in energy absorption ability when the vent diameters were altered. This trend continued in Part B of the study, where the chambers with the 5 mm vent diameter transmitted the least force, and the chambers with 0 mm vent diameter transmitted the most. These results confirmed the hypothesis and reasoning for Part B of the study, that under low impact velocities, non-vented chambers transmit more force than vented chambers.

Under low impact velocities, the air chambers performed better with larger vents as they allowed a greater volume of air to be expelled, enabling the chamber to ride down more and engage the TPU material's ability to manage energy. Thus, the chambers were deformed elastically with some plastic drawing. The TPU 90A material underwent more plastic drawing than the TPU 45D material, as it is softer than TPU 45D, and therefore compressed more than the TPU 45D chambers, engaging more of the material's plasticity, evident by the shapes of the TPU 90A and TPU 45D force-time curves in Figure 35 and Figure 38.

Further, analysis using Pearson's correlation at 1.3 m/s, indicated that as air flow rates decreased and air flow duration increased, peak force for both materials increased, shown in Figure 35 (c, d). The smaller the vent, the longer the air flow duration and lower the vent rate. This increased duration and the lower vent rate did not allow the material to expel enough air to activate plastic drawing of the material, which is highly desirable in helmets, where a "sharp fracture" should not take place (Wolstenholme, 1968). As a result, the smaller vents transmitted more force at low inbound velocities.

The overall force-time curves of both materials (all vent diameters) were not entirely symmetrical which occurs in completely elastic deformations (Coban et al., 2008). The first part of the force-time curve (until peak force) was directly related to damage/crack initiation. There was an identical linear increase in force with time at the start of the impact for all vent diameters of a given material, indicating the material's linear elastic phase. No damage would have occurred at this point if loading was terminated (Zhang & Richardson, 2007). The second part of the curve, however, was associated with some damage propagation, in which force decreased with increasing time. In general, at 1.3 m/s, the chambers appeared to be deformed primarily by elastic deflection. Both TPU 45D and TPU 90A exhibited some plastic drawing and crack initiation, however, TPU 90A experienced less due to its highly elastic composition.

Once the material's elastic capacity to absorb energy was compromised, only the plasticity of the chambers remained to absorb energy. Thus, once the material reached its yield strength, a first peak in the graph occurred, followed by a second peak when the plastic's ability to manage energy was compromised.

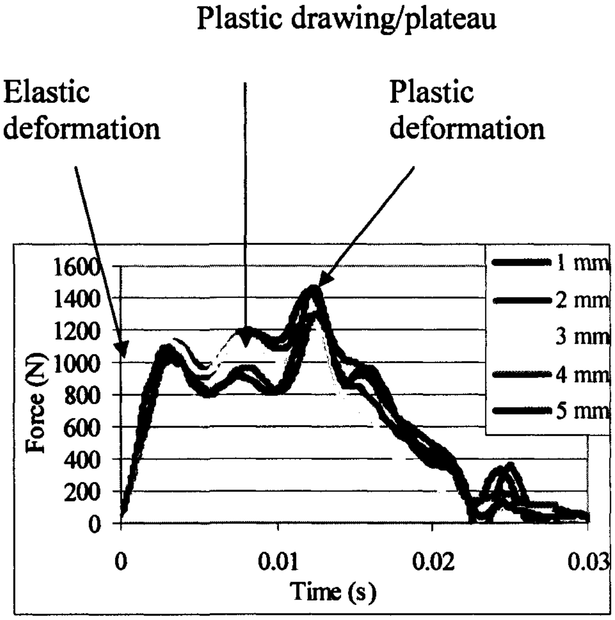

Figure 39. Force-time curve of TPU 45D with various vent diameters (1-5 mm), impacted at 2.3 m/s, set 3.

As inbound velocity was progressively increased, the chambers underwent predominantly plastic deformation – tearing with no drawing, resulting in a shape change of the force-time curve. This occurred when the TPU 45D and TPU 90A chambers were impacted at 3.0 m/s (and the TPU 90A chambers at 2.3 m/s with the large vents). When the chambers were impacted with a high inbound velocity, the chamber's ability to manage the energy through plastic deflection was compromised and a fairly sharp increase to peak force occurred. This increase in peak force was correlated with a high vent rate and short air flow duration. When this happened, the small vent diameters (1, 2 mm) transmitted significantly less force than the larger vent diameters. Thus, at 3.0 m/s, the effect of vent diameter on peak reaction force reversed. This trend occurred in Part B of the study, where the largest vent transmitted the most force and the non-vented chamber transmitted the least.

At high inbound velocities, the small vents did not allow the air to escape quickly and thus the air was able to attenuate more of the impacting energy, as the material was compromised. When a large vent was used, both the chamber's energy absorption mechanisms, material and air, were compromised early and the chamber was not able to adequately manage the impact energy. This is evident when looking at the chamber's force-time curves combined with the air velocity curves. The larger vents resulted in a shorter air flow duration (and high venting rates overall), when compared to the smaller vents.

At 2.3 m/s, the transition between low and high impact velocity characteristics occurred. Analysis of the force-time curves showed all TPU 45D chambers (1-5 mm) performed similarly with respect to elastic/plastic deformation, while the TPU 90A chambers with the smallest vents performed much better than the larger vents. This difference can be accounted for by the differences in material composition. The TPU 90A chambers are softer and bottomed out earlier than the TPU 45D chambers. With TPU 90A chambers, the higher the venting rate and shorter the duration of air flow, the higher the peak force. This was opposite with TPU 45D. This difference in air flow characteristics suggests that high venting rates and short air flow durations are correlated with peak force when chambers undergo predominantly plastic deformation. In contrast, for chambers deformed primarily through elastic deflection peak force is correlated with long air flow durations and slower air flow rates.

This study has proven that a chamber's vent diameter has a significant effect on the peak reaction force when it is impacted. Consequently, the hypothesis stating a significant difference exists in peak force during an impact for chambers with various vent diameters and material stiffnesses was accepted. This study also confirmed the hypothesis suggesting a significant relationship exists between peak force and peak air flow rate as well as peak force and air flow duration.

5.2. Material Stiffness

Across all inbound velocities and vent diameters the TPU 45D chambers transmitted significantly less force than the TPU 90A chambers. The TPU 90A chambers were too soft to withstand the range of inbound velocities to which they were subjected, in comparison to the TPU 45D.

At the lowest inbound velocity, the TPU 90A chambers performed significantly better than the TPU 45D chambers as they consist of more soft elements and are therefore more elastic. The TPU 90A chambers were able to undergo more plastic drawing than the TPU 45D chambers which enhanced their energy attenuation ability. However, due to this highly elastic composition, they underwent plastic deformation earlier than the TPU 45D chambers, as inbound velocity increased. This resulted in a spike in the peak force for the larger vent diameters, as less air was present to assist in absorbing energy.

5.3. Inbound Velocity

The ability of the air chambers to attenuate impact energy decreased as inbound velocity was increased. The effectiveness of the chambers was therefore decreased, as they transferred more energy and absorbed less. The air chambers demonstrated excellent energy attenuation properties at all inbound velocities, when vent diameter was optimized.

5.4. Flow Visualization

Results from the flow visualization suggested that upon initial exiting of the chamber, the air appeared turbulent. This may initially have restricted, or reduced air emission on impact, resulting in a decreased ride-down ability of the chamber immediately on impact. The resistance was then overcome and the air became laminar. The turbulence was consistent with research which suggests that as air flows at high velocities, it displays chaotic behaviour (Ball, 1996).

Flow visualization also initially revealed the high speeds at which air was expelled by the chamber. Upon examination of the thermal anemometry results, it was determined that the air flow speeds ranged from approximately 40 m/s to 210 m/s, indicating compressible flow (>102.9 m/s) occurred on some impacts and, therefore, may not have followed Bernoulli's Law. The compressibility of air also may explain why the vent rate did not consistently increase with increasing vent diameter. Further, Bernoulli's Law assumes flow is steady, which may not have occurred because of the chamber collapse mechanisms explained previously.

5.5. Trial Effect

Analysis of a trial effect for the three inbound velocities indicated differences in multi-impact performance at each velocity. At 1.3 m/s, with each subsequent impact, chamber performance increased. This occurred because with each subsequent impact, the amount of plastic deformation increased as the hard segments in TPU became progressively compromised, leading to more plastic drawing. Nevertheless, *post hoc* testing indicated no significant differences existed between trials with the exception of between 1 and 8-10. Since elastic deformation is reversible and the chambers underwent *predominantly* elastic deflection at 1.3 m/s, it can be assumed that under low impact velocities the chambers are multi-impact. Delamination, however, may have occurred, which is not always visible to the naked eye. Delamination is a mode of failure which can occur in composite materials, such as thermoplastic matrix composites, under low velocity impacts (Coban et. al, 2008).

At 2.3 and 3.0 m/s, however, chamber performance decreased with increasing impacts. This occurred because of progressively increased plastic deformation with increased velocity. At 2.3 m/s, significant differences existed between the first/second impacts and the remaining (a difference of 595 N existed between the first and third trials). At 3.0 m/s, large, significant differences existed between the first impacts and the rest (1494 N between first and second trials). See Figure 40 below for an example. Thus, decreases in performance occurred with subsequent impacts at high inbound velocities because of the crack propagation in the material. Nevertheless, the chambers were able to deflect elastically on impact and the air was still present to participate in energy absorption. Thus, these chambers were still able to absorb a significant amount of energy with multiple impacts due to the elasticity of the chambers and the air contained within.

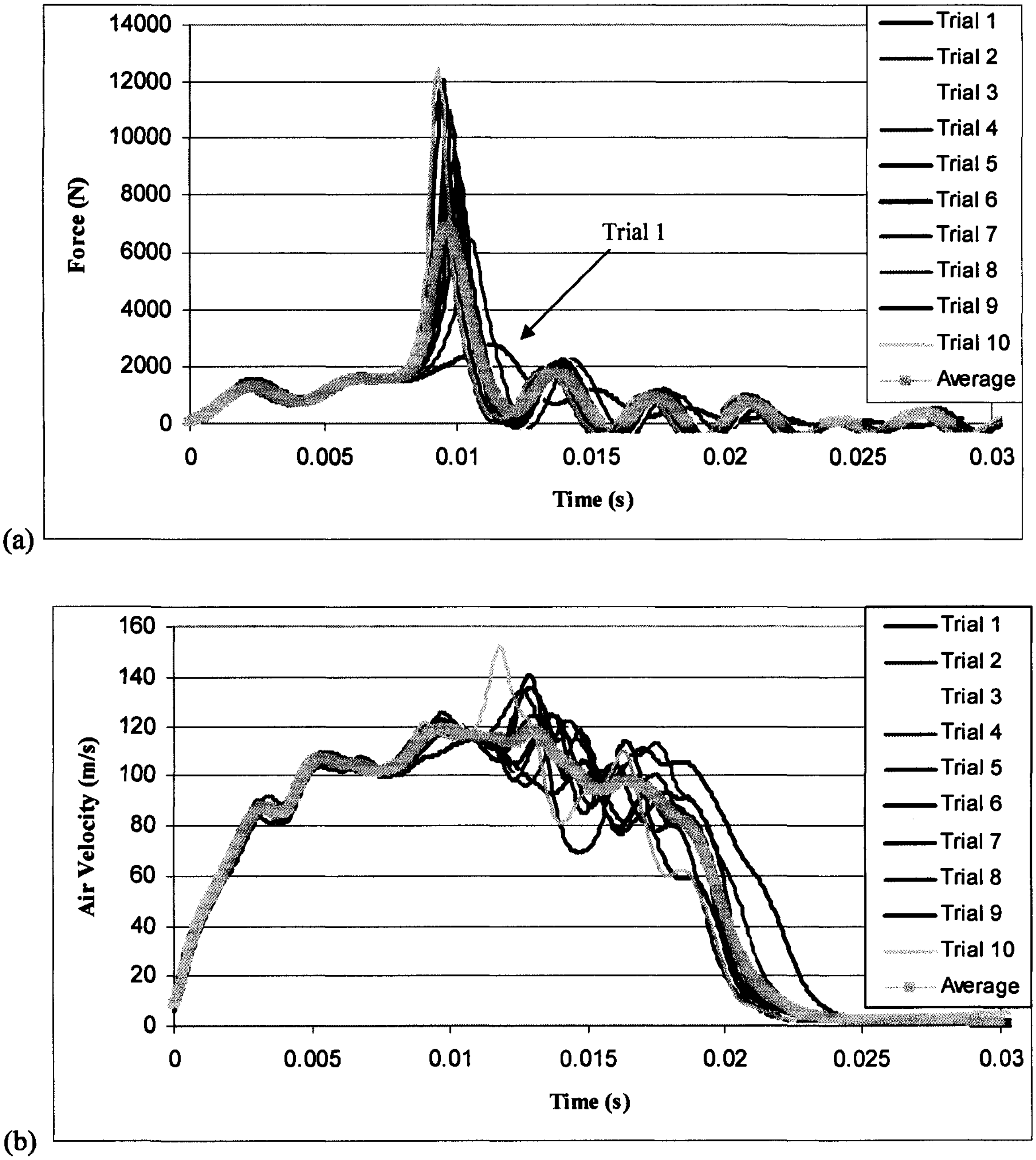

Figure 40. Force-time curve (a) and air velocity curve (b) of TPU 45D, 1 mm, impacted ten times at 3.0 m/s, set 1.

5.6. Optimal Energy Absorber

The force-time curves of the chambers impacted in this study, demonstrate the chambers' ability to achieve an optimal energy absorber force-time curve. As evident in the 1.3 and 2.3 m/s impacts, the force trace was broad and flat, demonstrating a "soft landing." When optimal venting was used, such as a 5 mm vent shown in Figure 38b, venting was able to "shape" the force-time curve, reducing the peak force and increasing the duration of impact.

The findings in this study can ultimately be explained by the energy absorption mechanisms of the air chamber. Although the chambers consist of four engineering elements, they essentially consist of only two energy absorption elements – the TPU material and the air contained within the chamber. The geometry of the chamber, although critical to its performance, is a function of the material. If the material fails, the structure will follow suit. The concertina mode of collapse due to the geometry is a way to engage certain material characteristics, such as plastic deformation at the hinges. Thus, the concertina mode of collapse allows the material and structure to undergo plastic drawing better. Similarly, the venting of the chambers is a way to manipulate the air contained within to engage certain material characteristics. The performance of chambers in this study, therefore, depended on the material's ability to withstand an impact which was altered based on air dissipation through the venting system.

CHAPTER 6. CONCLUSION

6.1. Summary

Both mild and severe head injuries have been associated with poor cognitive, psychological, and neurocognitive outcomes, demonstrating the importance of protecting the brain under a range of impact conditions (Barth et al., 2002). The neurocognitive deficits for specific impact conditions has yet to be established and therefore, it is essential that head protection devices adequately protect the brain from a variety of impact energies, ensuring the preservation of its pre-injury ability and function. Designing for impact resistance under a range of conditions is a difficult task, requiring the engineer to understand the strengths and limitations of the energy absorber's structure failure and the mechanisms by which these structures dissipate inputted energy.

This study assisted in such understanding and demonstrated the ability of air chambers to absorb a large amount of impacting force under low and high impact velocities by manipulating one of its engineering opportunities – vent diameter. When vent diameter was manipulated, the chambers' energy absorption characteristics were altered. Results from the series of tests in this study showed an increase in chamber performance with large vent diameters under low impact velocities and no orifice under high impact velocities. The venting system appeared to manage the material characteristics. Venting dictated the elastic/plastic deflection of the material and consequently the structures ability to manage energy on impact.

Moreover, the findings of this study showed that the air chambers were able to be impacted multiple times under low inbound velocities due to the reversibility of the elastic components of TPU and the presence of air contained within the chamber. Under high velocity conditions, TPU's plasticity became compromised and the chamber showed a gradual decrease in performance with ten impacts. Nevertheless because of its elastic components and air within, the chambers were still capable of performing adequately. In regards to the hypotheses presented at the beginning of the study, it was determined that there was a significant difference in peak force and air flow rates during an impact for the chambers' vent diameters, as well as a significant relationship between peak air flow rate and peak force and between air flow duration and peak force.

This study suggests that manufacturers should consider manipulating the venting system of the air chambers to improve their performance within helmets and ultimately to help better protect the brain. This study also demonstrated the ability of air chambers to achieve the optimal energy absorber force-time curve, increasing the duration of impact and reducing the spike of energy transferred to the head, thereby reducing insult to the brain. Data taken from this study can serve as a basis for the science behind air chamber technology and implementation in head protection devices.

Safety standards committees, manufacturers, and national sporting associations all need to consider their role in improving the level of protection which helmets provide. With the development of this novel design, it is hoped that safety standards committees will now improve existing standards, manufacturers will consider replacing conventional helmet materials with air chambers, and national sporting agencies will recognize the improved level of performance air chambers provide and encourage players to wear air chamber containing helmets.

6.2. Future Work

Based on the results of the study, manufacturers should focus on optimizing the release of air from the chambers to improve their performance under a broad range of impact velocities. A system capable of expelling a large amount of air on impact from low velocities while conserving the air volume within for high velocities should be considered in such designs.

To fully investigate chamber performance, it was essential that single chambers were isolated and tested. Future studies should consider examining the generalizability of the results to a full helmet design containing an array of multiple chambers. Further, future studies should consider examining the material microscopically upon impact, to fully characterize the chambers' morphological response under dynamic loading. Additional research should also carefully examine the influence of the other engineering parameters on chamber performance, establish methods for evaluating air flow inside of the chamber under axial and oblique impacts, analyze pressure distributions inside the chamber and how that affects its performance.

Currently, knowledge of impact vectors through head protection devices can be easily and accurately tested. By altering the energy absorbing capability of helmets through various technologies such as air chambers, this impact vector can be altered/reduced with the goal of decreasing insult to the head. However, a large gap in the literature presently exists defining how that impact vector affects the brain. Therefore, future research should ultimately characterize the brain's response to a variety of impacts, so head protection devices can be guaranteed to protect the brain from injury.

REFERENCES

Abdul-Latif, A. & Nesnas, K. (2003). Plastic collapse of cylinders under constrained conditions. *Journal of Engineering Materials and Technology, 125,* 215-221.

Abramowicz, W. (2003). Thin-walled structures as impact energy absorbers. *Thin-Walled Structures, 41,* 91-107.

Agui, J.C. & Jimenez, J. (1987). On the performance of particle tracking. *Journal of Fluid Mechanics, 185,* 447-468.

Alexander, J.M. (1960). An approximate analysis of the collapse of thin cylindrical shells under axial loading. *The Quarterly Journal of Mechanics and Applied Mathematics, 13,* 10-15.

Alghamdi, A.A.A. (2001). Collapsible impact energy absorbers: an overview. *Thin-Walled Structures, 39,* 189-213.

Aljawi, A.A.N., Alghamdi, A.A.A., Abu-Mansour, T.M.N. & Akyurt, M. (2005). Inward inversion of capped-end frustra as impact energy absorbers. *Thin-Walled Structures, 43,* 647-664.

American Association for Automotive Medicine. (1980). *The abbreviated injury scale: AIS-80. Committee on injury scaling.* Morton Groove: American Association for Automotive Medicine.

Andrews, K.R.F., England, G.L. & Ghani, E. (1983). Classification of the axial collapse of cylindrical tubes under quasi-static loading. *International Journal of Mechanical Sciences, 25* (9-10), 687-696.

Asanuma, T. (1977). *Flow visualization.* Washington: Hemisphere Publishing Corporation.

ASTM International. (2005). Standard test method for rubber property – durometer hardness: D 2240-05. West Conshohocken, PA.

Atkins, A.G. & Mai, Y.W. (1985). *Elastic and plastic fracture: Metals, polymers, composites, biological materials.* New York: Ellis Horwood Limited.

Ball, W.C. (1996). Air flow. *John Hopkins School of Medicine.* Retrieved 12/24/2006 from: http://oac.med.jhmi.edu/res_phys/Encyclopedia/AirFlow/AirFlow.html.

Bank, H.W., Sardanopoli, A.A., Ulrich, H. & Sayigh, A.A.R. (1971). Pellethane®: A new generation of polyurethane thermoplastic elastomers. *Journal of Elastoplastics, 3,* 157.

Barth, J.T., Freeman, J.R., Broshek, D.K. & Varney, R.N. (2001). Acceleration-deceleration sport-related concussion: the gravity of it all. *Journal of Athletic Training, 36* (3), 253-256.

BASF. (2008a). *BASF material properties.* From Jeff Miller, BASF employee.

BASF. (2008b). *Injection molding.* From BASF, The Chemical Company.

Bayly, P.V., Cohen, T.S., Leister, Ajo, D., Lauthardt, E.C. & Genin, G.M. (2005). Deformation of the human brain induced by mild acceleration. *Journal of Neurotrauma, 22* (8), 845-856.

Brain Injury Association of Alberta. (2008). Facts about brain injuries. Retrieved 05/20/2008 from: http://www.biaa.ab.ca/.

Cadex Inc. (2006). Impact machine uni axle. Retrieved 08/15/2007 from: http://www.cadexinc.com/Impact/impactMachineUniAxle.html.

Camacho, D.L., Nightingdale, R.W. & Myers, B.S. (2001). The influence of surface padding on head and neck injury risk. *Journal of Biomechanical Engineering, 123,* 432-439.

Canadian Institue for Health Information. (2006). Head injuries in Canada: A decade of change (1994-1995 to 2003-2004). Retrieved 08/17/2007 from: http://secure.cihi.ca/cihiweb/en/downloads/analysis_ntr_2006_e.pdf.

Cantu, R.C. (2000). Overview of concussion. In R.C Cantu (Ed.), *Neurologic athletic head and spine injuries* (76-79). Philadelphia: W.B. Saunders Co.

Chen, L.B., Xi, F. & Yang, J.L. (2007). Elastic-plastic force history and response characteristics of circular plate subjected to impact by a projectile. *Acta Mechanica Sinica, 23,* 415-425.

Coban, O., Bora, M.O., Sinmazeclik, T., Curgul, I. & Gunay, V. (2008). Fracture morphology and deformation characteristics of repeatedly impacted thermoplastic matrix composites. *Materials and Design,* Manuscript draft.

Control Company. (2005). *Traceable certificate of calibration for digital calipers.* Texas: Control Company.

Dantec Dynamics. (2000a). *Miniature CTA 54T30.* Denmark: Dantec Measurement Technology A/S.

Dantec Dynamics. (2000b). *Probes for hot wire anemometry.* Retrieved 05/14//2006 from: http://www.dantecdynamics.com/Admin/Public/Download.aspx?file=/Files/filer/Products%20and%20Services/General%20literature/238-2-probekatalog.pdf.

Di Landro, L., Sala, G. & Olivieri, D. (2002). Deformation mechanisms and energy absorption of polystyrene foams for protective helmets. *Polymer Testing, 21* (2), 217-228.

Ehrlich, B.S., Farrissey, W.J., Goldwasser, D.J., Oertel, R.W. & Onder, K. (1984). A high-impact polyurethane engineering thermoplastic. *Journal of Elastomers and Plastics, 16,* 136-146.

Feraboli, P. (2006). Modified SDOF models for improved representation of the impact response of composite plates. *Journal of Composite Materials, 24* (40), 2235-2255.

Finkelstein, E., Corso, P. & Miller, T. (2006). *The incidence and economic burden of injuries in the United States.* New York: Oxford University Press.

Gadd, C.W. (1966). Use of weight-impulse criterion for establishing injury hazard. In *Proceedings of the tenth Stapp car crash conference: Holloman air force base, New Mexico, November, 1966* (146). New York: Society of Automotive Engineers.

Gaetz, M. (2004). The neurophysiology of brain injury. *Clinical Neurophysiology, 115,* 4-18.

Gennarelli, T.A. & Wodzin, E. (2006). AIS 2005: A contemporary injury scale. *Injury. International Journal of the Care of the Injured, 37,* 1083-1091.

George, D. & Mallery, P. (2007). SPSS for Windows step by step. A simple guide and reference 14.0 update. 7th ed. Boston: Pearson Education Inc.

Gilchrist, A. & Mills, N.J. (1994). Modeling of the impact response of motorcycle helmets. *International Journal of Impact Engineering, 15,* 201-218.

Gimbel, G. & Hoshizaki, T.B. (2008). Comparison between polymeric foams used in ice hockey helmets and venting air chambers on attenuating impact forces. *Fifth International Symposium on Safety in Ice Hockey, Denver, CO, ASTM International,* West Conshohocken, PA.

Goldsmith, W. & Plunkett, J. (2004). A biomechanical analysis of the causes of traumatic brain injury in infants and children. *The American Journal of Forensic Medicine and Pathology, 25* (2), 89-100.

Goldstein, R.J. (1996). *Fluid mechanics measurements (2nd ed).* Washington: Taylor & Francis.

Great Little Box Company. (2006). Box structure. Retrieved 11/30/2006 from: http://www.greatlittlebox.com/pack101_structure.php

Greene, J. (2005). Mechanical engineering, mechatronic engineering and manufacturing technology class cotes: Mechanical behaviour. California State University. Retrieved 06/01/2008 from: www.csuchico.edu/~jpgreene/.

Guerra, D., Plaisted, A. & Smith, M. (2005). A Bernoulli's law lab in a bottle. *The Physics Teacher, 43,* 456-459.

Harte, A.M., Fleck, N.A. & Ashby, M.F. (2000). Energy absorption of foam-filled circular tubes with braided composite walls. *European Journal of Mechanical Alloys and Solids, 19,* 31-50.

Hesselink, L. (1988). Digital image processing in flow visualization. *Annual Review of Fluid Mechanics, 20,* 421-485.

Hoshizaki, T.B. & Brien, S.E. (2004). The science and design of head protection in sport. *Neurosurgery, 55* (4), 956-967.

Hwang, I.K. & Kim, K.J. (2006). Biomechanical efficiency of wrist guards as shock absorbers. *Journal of Biomechanical Engineering, 128,* 229-234.

Instron. (2004). Shore durometer. Retrieved 06/30/2007 from: http://www.instron.us/wa/library/default.aspx

Kawashima, K., Fujita, T. & Kagawa, T. (2000). Instantaneous flow rate measurement of ideal gases. *Journal of Dynamic Systems, Measurement, and Control, 122* (1), 174-178.

Kawahima, K., Fujita, T. & Kagawa, T. (2001a). Flow rate measurement of compressible fluid using pressure change in the chamber. *Transactions of the Society of Instrument and Control Engineers, E-1* (1, 1/7), 1-7.

Kawashima, K., Fujita, T. & Kagawa, T. (2001b). Unsteady flow rate measurement of air using isothermal chamber. *Transactions of the Society of Instrument and Control Engineers, E-1* (1, 1/6), 1-7.

Kawashima, K., Ishii, Y., Funaki, T. & Kagawa, T. (2004). Determination of flow rate characteristics of pneumatic solenoid valves using an isothermal chamber. *Journal of Fluids Engineering, 126,* 173-279.

Kim, K.J., Alian, A.M., Morris, W.S. & Lee, Y.H. (2006). Shock attenuation of various protective devices for prevention of fall-related injuries of the forearm/hand complex. *The American Journal of Sports Medicine, 34* (4), 637-643.

Kramer, C.F., Barancik, J.I. & Thode, H.C. (1990). Improving the sensitivity and specificity of the Abbreviated Injury Scale coding system. *Public Health Reports, 105* (4), 334-340.

Kraus, J.F. & McArthur, D.L. (1996). Epidemiologic aspects of brain injury. *Neurologic Clinics, 14* (2), 435-450.

Liu, D., Chang, C.Y., Fan, C.M. & Hsu, S.L. (2003). Influence of environmental factors on energy absorption degradation of polystyrene foam in protective helmets. *Engineering Failure Analysis, 10,* 581-591.

Mamalis, A.G., Manolakos, D.E., Saigal, S., Viegelahn, G. & Johnson, W. (1986). Extensible plastic collapse of thin-wall frustra as energy absorbers. *International Journal of Mechanical Sciences, 28* (4), 219-229

Marieb, E.N. (2001). *Human anatomy & physiology (5th ed).* New York: Benjamin Cummings.

Matweb. (2008a). BASF Ellastollan® S90A polyester type polyurethane elastomer. From Xenith, LLC.

McElhaney, J. (1976). Head injury critera. *Mechanics of Composite Materials, 12* (3), 411-429.

McHenry, B.G. (2004). *Head injury criterion and the ATB.* McHenry Software Inc.

McIntosh, A. & McCrory, P. (2000). Impact energy attenuation performance of football headgear. *British Journal of Sports Medicine, 34,* 337-341.

McIntosh, A., McCrory, P. & Finch, C.F. (2004). Performance enhanced headgear: a scientific approach to the development of protective headgear. *British Journal of Sports Medicine, 38,* 46-49.

McLean, A.J. & Anderson, R.W.G. (1997). Biomechanics of closed head injury. In P. Reilly & R. Bullock (Eds.). *Head injury: Pathophysiology and management* (25-37). London: Chapman & Hall.

Mills, N. (2007). *Polymer foams handbook. Engineering and biomechanics applications and design guide.* Amsterdam: Elsevier Ltd.

Mills, N.J. & Gilchrist, A. (1991). The effectiveness of foams in bicycle and motorcycle helmets. *Accident Analysis and Prevention, 23,* 153-163.

Mills, N.J. & Masso-Moreu, Y. (2005). Finite element analysis (FEA) applied to polyethylene foam cushions in package drop tests. *Packaging Technology and Science, 18,* 29-38.

Naganathan, P., He, J. & Kirkpatrick, J. (1999). The effect of compression of enclosed air on the cushioning properties of corrugated fibreboard. *Packaging Technology and Science, 12,* 81-91.

Nardo, N.R. (1987). End use applications for thermoplastic elastomers. *Journal of Elastomers and Plastics, 19*, 59-76.

NASA. (2007). Educational resources. Retrieved 01/30/2007 from: http://www.nas.nasa.gov/About/Education/Racecar/glossary.html

National Physical Laboratory. (2007). The UK's National Measurement Laboratory. Retrieved 05/28/2007 from: http://www.npl.co.uk/force/guidance/hardness/rubber.html

Newman, J.A. (1993). Biomechanics of human trauma: Head protection. In A.M. Nahum & J.W. Melvin (Eds.), *Accidental injury biomechanics and prevention* (292-310). New York: Springer-Verlag.

Newman, J.A. (2002). Biomechanics of head trauma: Head protection (2nd ed.). In A.M. Nahum & J.W. Melvin (Eds.). *Accidental injury* (303-323). New York: Springer-Verlag.

Newman, J.A. (2006). A proposal for ASTM F08-53's consideration – A new severity index NSI for helmet impact assessment. ASTM F08-53 submission.

Newman, J.A., Beusenberg, M., Fournier, E., Shewchenko, N., Withnall, C., King, A.,Yang, K., Zhang, L., McElhaney, J., Tibault, L. & McGinnis, G. (1999). A new biomechanical assessment of mild traumatic brain injury. Part 1-methodology. In *Proceedings of the international IRCOBI conference in biomechanics of impacts, Barcelona, Spain, 1999.* Barcelona: IRCOBI Secretariat.

Newman, J.A., Beusenberg, M., Shewchenko, N., Withnall, C. & Fournier, E. (2005). Verification of biomechanical methods employed in a comprehensive study of mild traumatic brain injury and the effectiveness of American football helmets. *Journal of Biomechanics, 38,* 1469-1481.

Nolan, C. (2005) Traumatic brain injury. A review. *Critical Care Nursing, 28* (2), 188-194.

Nordin, M. & Frankel, V.H. (2001). *Basic biomechanics of the musculoskeletal system (3rd ed).* New York: Lippincott Williams & Wilkins.

Nutem Limited. (1986). Flow visualization equipment. Integrated smoke generator system (internal vaporization). *Nutem Limited Operation Instructions.*

Omaya, M. (2002). Neuropathological investigation of cerebral white matter lesions caused by closed head injury. *Neuropathology, 22,* 243-251.

Pacific Transducer Corporation. (2007). Model 478 and 479 Deadweight Test Stand for PTC's e2000® Style Durometer. Retrieved 06/01/2007 from: http://www.ptc1.com/durometers_acc_478-479.html

Patrick, L.M. & Grime, G. (1970). Applications of human tolerance data to protective systems: Requirements for soft tissue bone and organ protective devices. In E.S. Gurdjian (Ed.), *Impact injury and crash protection* (444-473). Springfield: Thomas.

PCB Piezotronics. (2004). *Model 484B06. Line-powered ICP sensor signal conditioner. Installation and operating manual.* New York: PCB Piezotronics Electronics Division.

PCB Piezotronics. (2003). *Model 203B. ICP dynamic force sensor. Installation and operating manual.* New York: PCB Piezotronics Force/Torque Division.

Pellman, E.J. Viano, D.C., Tucker, A.M., Casson, I.R. & Waeckerie, J.F. (2003). Concession in professional football: Reconstruction of game impacts and injuries. *Neurosurgery, 53,* 799-812.

Penn Plastics Inc. (2003). *FAQ on plastic injection molding.* Retrieved 09/5/2008 from: http://www.pennplastics.com/faq.htm

Photron Limited. (2003). *Fastcam-512 PCI hardware manual.* San Diego: Photron USA Inc.

Prasad, P. & Mertz, H.J. (1985). The position of the United States delegates to the ISO working group 6 on the use of HIC in the automotive environment. SAL paper 941056.

Robertson, D.G.E. (1997). Introduction to biomechanics for human motion analysis. Waterloo: Waterloo Biomechanics.

Robertson, D.G.E., Caldwell, G.E., Hamill, J., Kamen, G. & Whittlesey, S.N. (2004). *Research methods in biomechanics*. Champaign, Il: Human Kinetics.

Sahin, T., Sinmazcelik, T., Arici, A. (2004). Investigation about the effect of previous impacts on the impact behavior of high impact polystyrene (HIPS). *Journal of Materials Science, 39,* 2543-2546.

Salvatore, S.P. & Skalak, R. (1993). The history of Poiseuille's law. *Annual Review of Fluid Mechanics*, 25, 1-19

Sasaki, H., Saito, K. & Abe, K. (1999). Development of an air cushioning material based on a novel idea. *Packaging Technology and Science, 12,* 143-150.

Silberberg, M.S. (2000). *Chemistry: The molecular nature of matter and change*. Boston: McGraw Hill Companies Inc.

Simmonds, J.G. (1996). Analytic functions, ideal fluid flow, and Bernoulli's equation. *SIAM Review, 38* (4), 666-667.

Singace, A.A., El-Sobky, H. & Petsios, M. (2001). Influence of end constraints on the collapse of axially impacted frustra. *Thin-Walled Structures, 39,* 415-428.

Spyrou, E. & Hoshizaki, T.B. (2001). Shock absorbing effectiveness of hockey helmet liner foams after exposure to repeated impacts. In F.H. Froes & S.J. Haake (Eds.), *Materials and science in sports* (199-209). Warrendale: Minerals, Metals, & Materials Society.

Strich, S. (1961). Shearing of nerve fibers as a cause for brain damage due to head injury. *Lancet, 2,* 443-448.

Tavoularis, S. (2005). *Measurement in fluid dynamics.* New York: Cambridge University Press.

Tian, Y.S. & Karayiannis, T.G. (2000). Low turbulence natural convection in an air filled square cavity. Part II: the turbulence quantities. *International Journal of Heat and Mass Transfer, 43,* 867-884.

TSI. (2006). *TSI Thermal anemometry probes*. Retrieved 04/30/2007 from: http://www.tsi.com/Product.aspx?Pid=197

United States' National Center for Injury Prevention and Control. (2006). What is traumatic brain injury? Retrieved 11/5/2006 from: http://www.cdc.gov/ncipc/tbi/TBI.htm

Varney, N.R. & Roberts, R.J. (1999). Forces and accelerations in car accidents and resultant brain injuries. In N.R. Varney & R.J. Roberts (Eds.), *The evaluation and treatment of mild traumatic brain injury* (39-48). Mahwah, NJ: Lawrence Erlbaum Associates.

Viano, D.C., King, A.I., Melvin, J.W., Weber, K. (1989). Injury biomechanics research: an essential element in the prevention of trauma. *Journal of Biomechanics, 22* (5), 403-417.

Wolstenholme, W.E. (1962). Characterizing impact behavior of thermoplastics. *Journal of Applied Polymer Science, I* (21), 332-337.

WPI. (2007). Punches. Retrieved 05/25/2007 from: http://www.wpi-europe.com/products/ microdissection/punches.htm

Yu-Hallada, C., Kuczynski E.T. & Weierstall, M. (1998). Polyurethane: The material choice for occupant protection and energy management. *Journal of Cellular Plastics, 34*, 272-267.

Zhang, H., Chen, Y., Zhang, Y., Sun, X., Ye, H. & Li, W. (2008). Synthesis and characterization of polyurethane elastomers. *Journal of Elastomers and Plastics, 40,* 161-177.

Zhang, L., Yang, K.H. & King, A.I. (2004). A proposed injury threshold for mild traumatic brain injury. *Journal of Biomechanical Engineering, 126,* 226-236.

Zhang, Z.Y. & Richardson, M.O.W. (2007). Low velocity impact induced damage evaluation and its effect on the residual flexural properties of pultruded GRP composites. *Composite Structures, 81,* 195-201.

APPENDIX

Appendix A

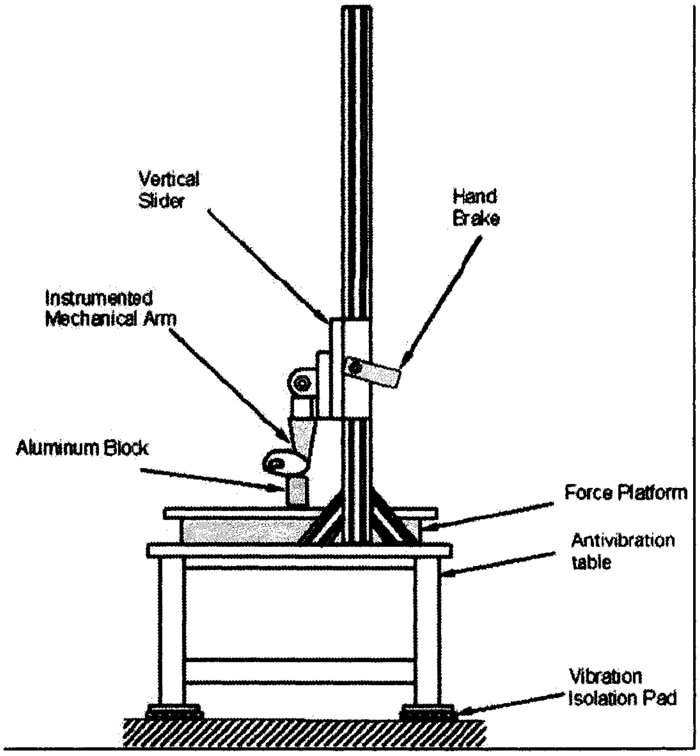

Figure 41. Free falling device which simulated a fall, using a mechanical surrogate arm (Kim et al., 2006).

Appendix B

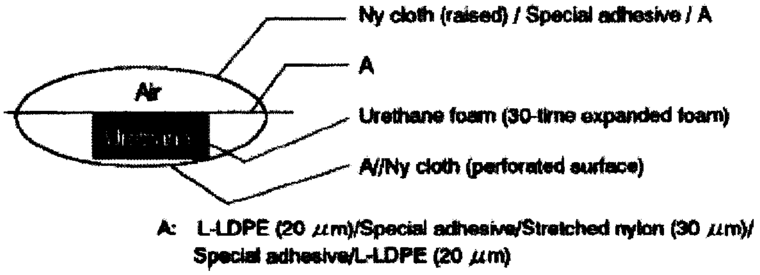

Figure 42. Diagram of the novel air cushioning material (NACM) (Sasaki et al., 1999).

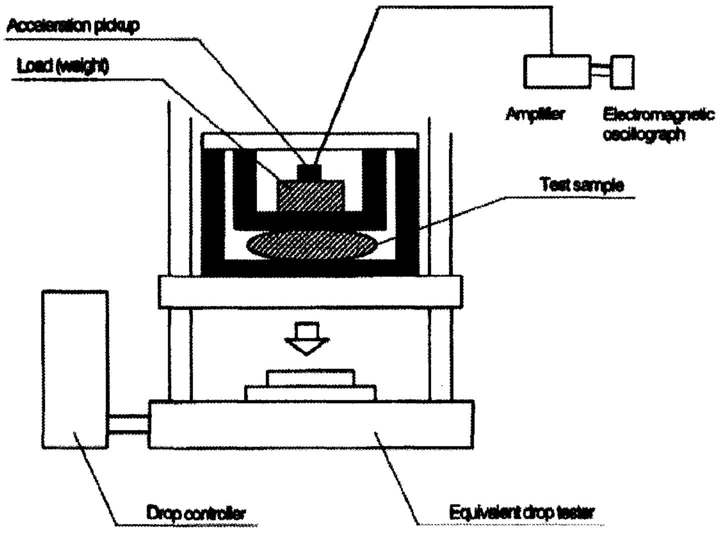

Figure 43. Drop test rig used to determine the energy absorption characteristics of the NACM (Sasaki et al., 1999).

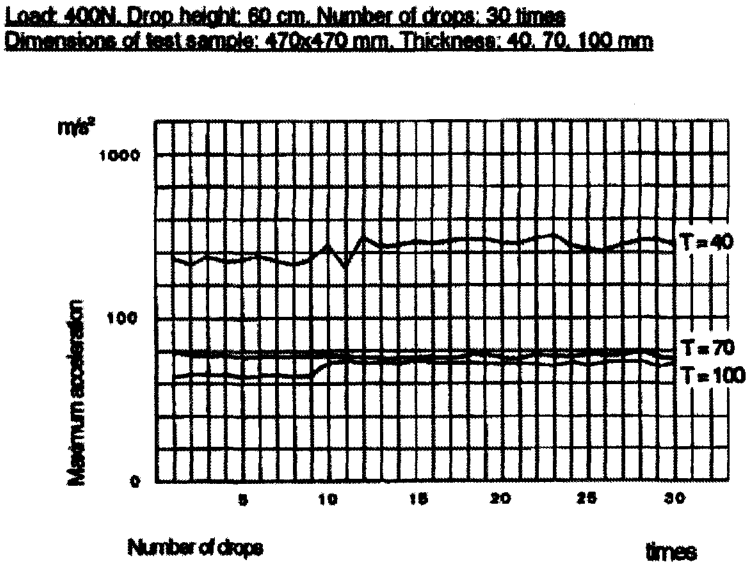

Figure 44. Changes in shock absorption of NACM with several drops (Sasaki, 1999).

Appendix C

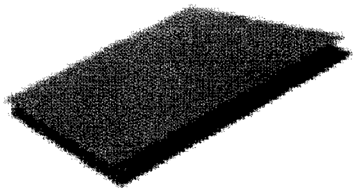

Figure 45. Photograph of a typical piece of corrugated fibreboard (Great Little Box Company, 2006).

Appendix D

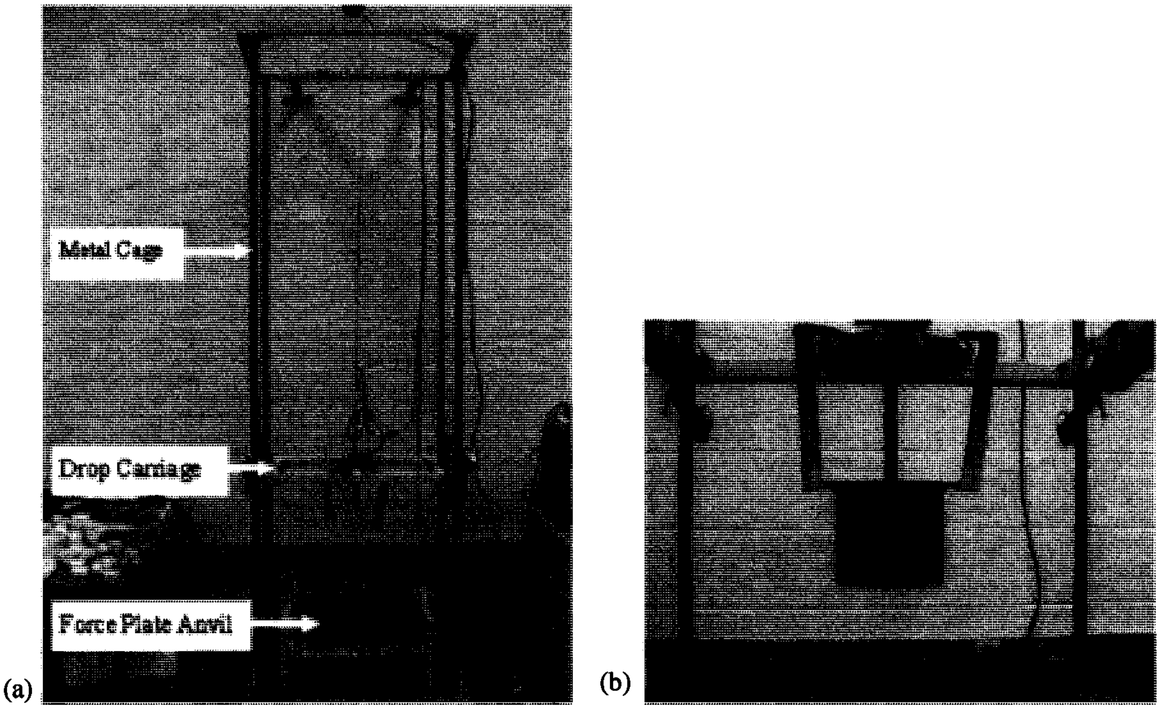

Figure 46. (a) Free drop test rig assembly used in determine energy absorption characteristics of air chambers and foam. (b) Flat impactor resting freely inside drop carriage assembly (Gimbel & Hoshizaki, 2008).

Appendix E

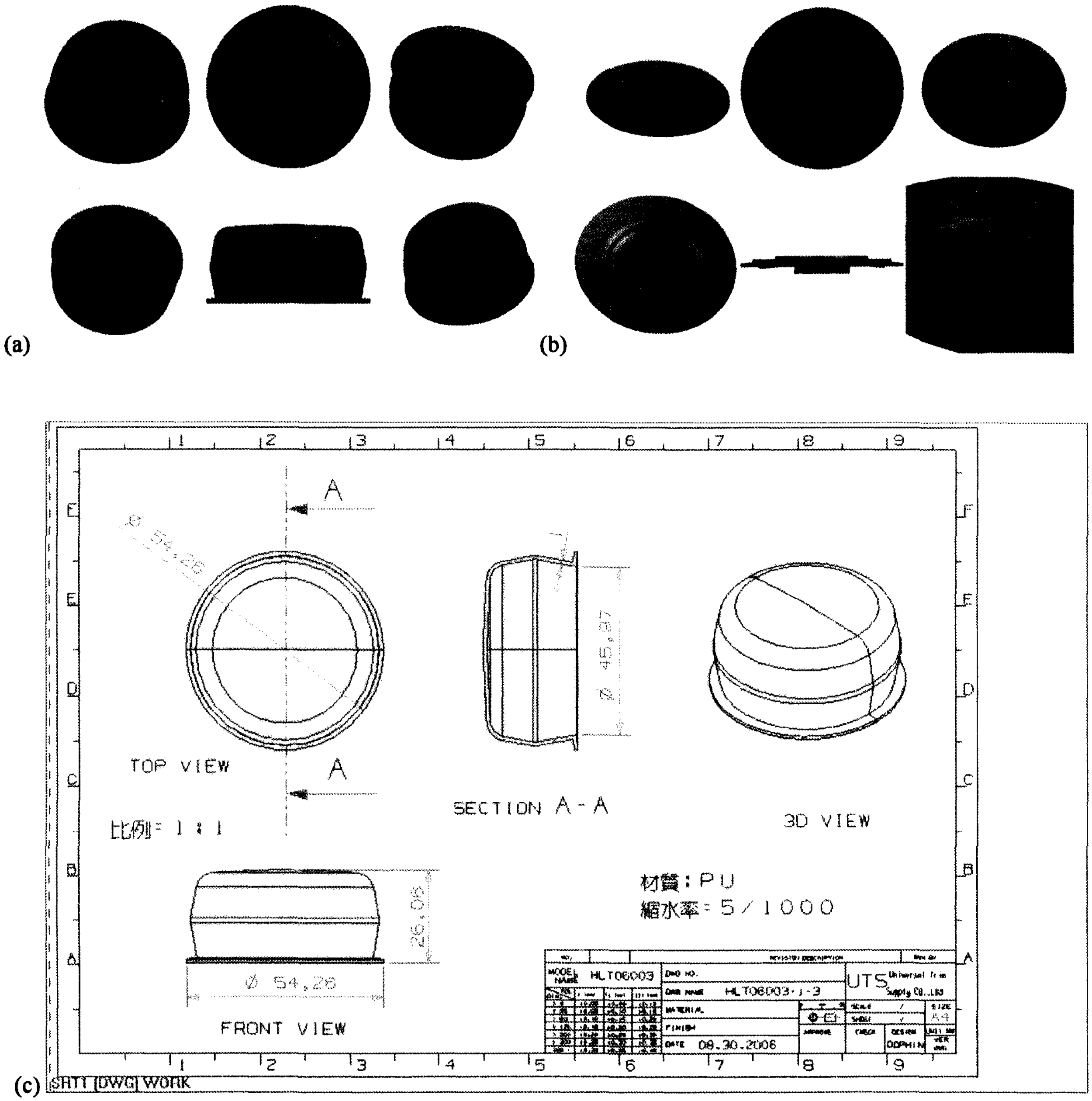

Figure 47. (a) Pictures of an air chamber from various angles. (b) Pictures of chamber base plate, in which orifice is made, from various angles. (c) CAD drawing of an air chamber, supplied by Xenith, LLC.

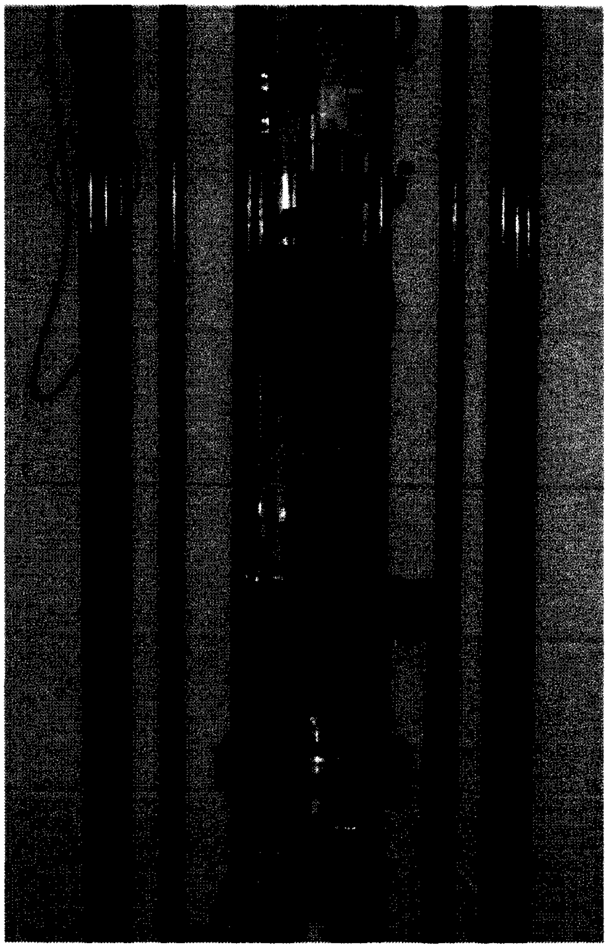

Figure 48. Photograph of the monorail drop test rig.

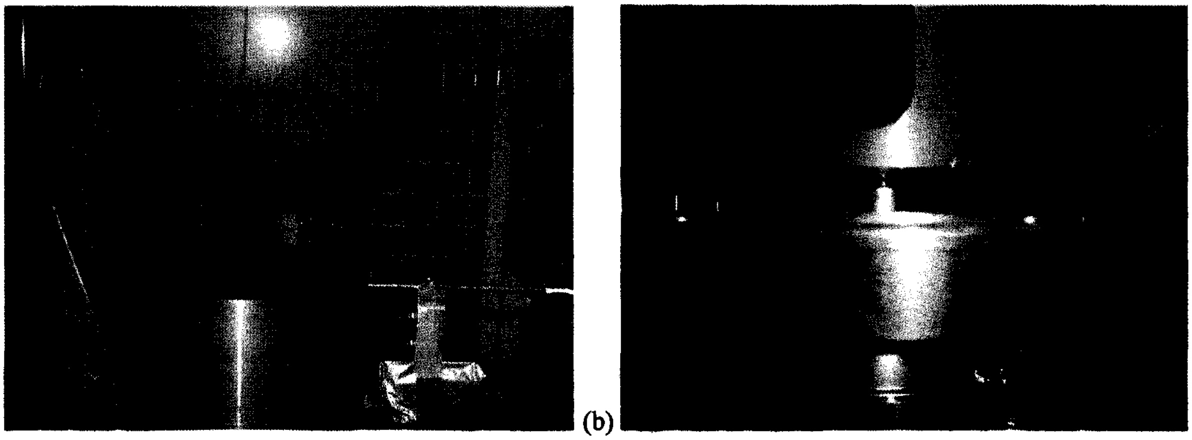

Figure 49. Photographs showing (a) anemometer sensor placement in jig and (b) base plate and force sensor placement.

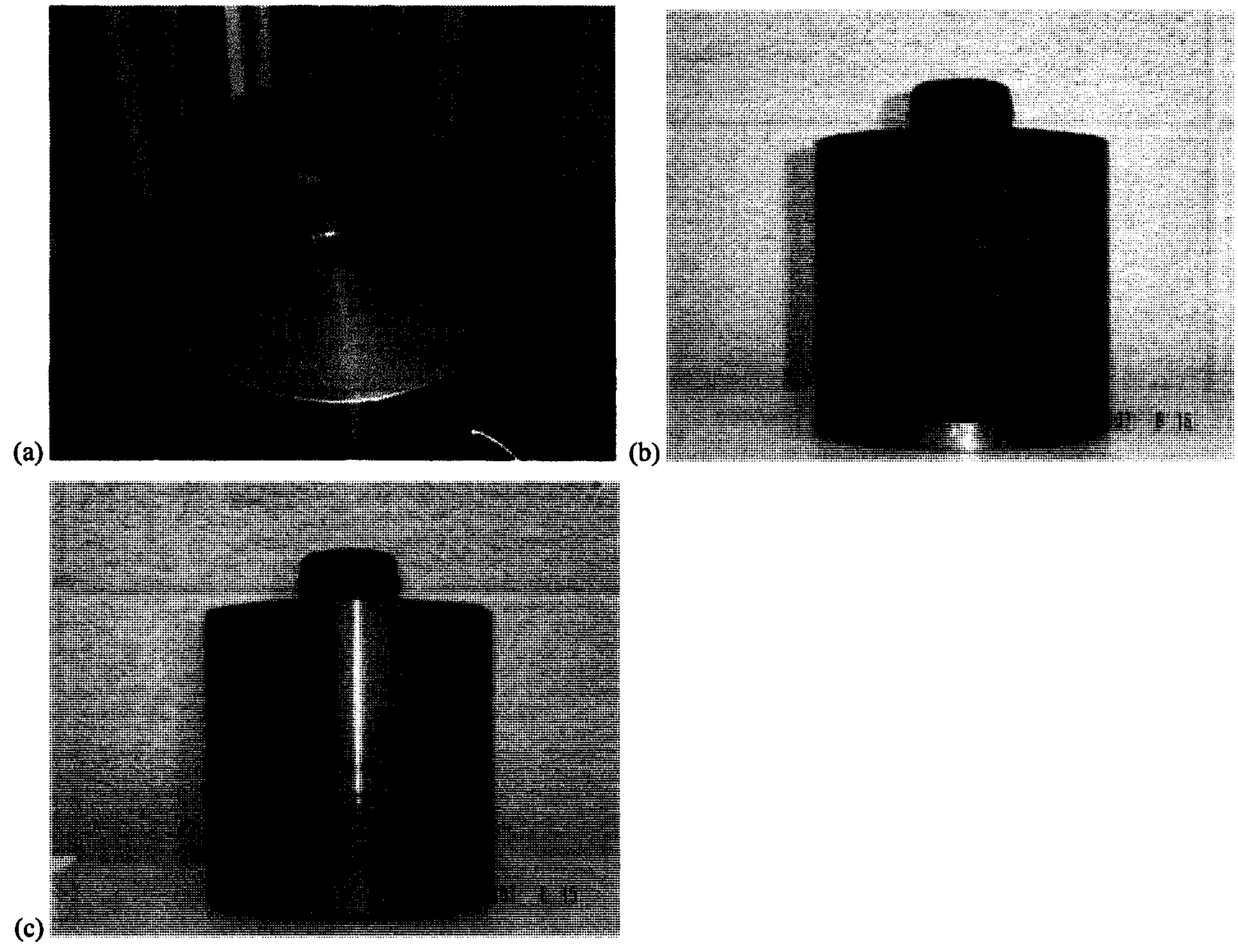

Figure 50. Photographs of jig used to visualize flow and for all data collection – (a) top view with vented chamber, (b) front view, (c) side view.

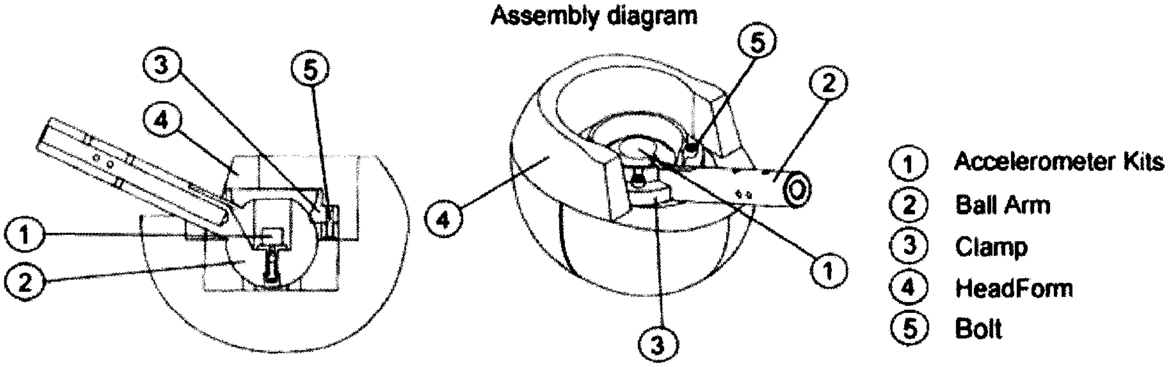

Figure 51. The Half Magnesium K1Aa headform showing the ball arm, clamp, and attachment bolts used in the present study (Cadex Inc, 2006).

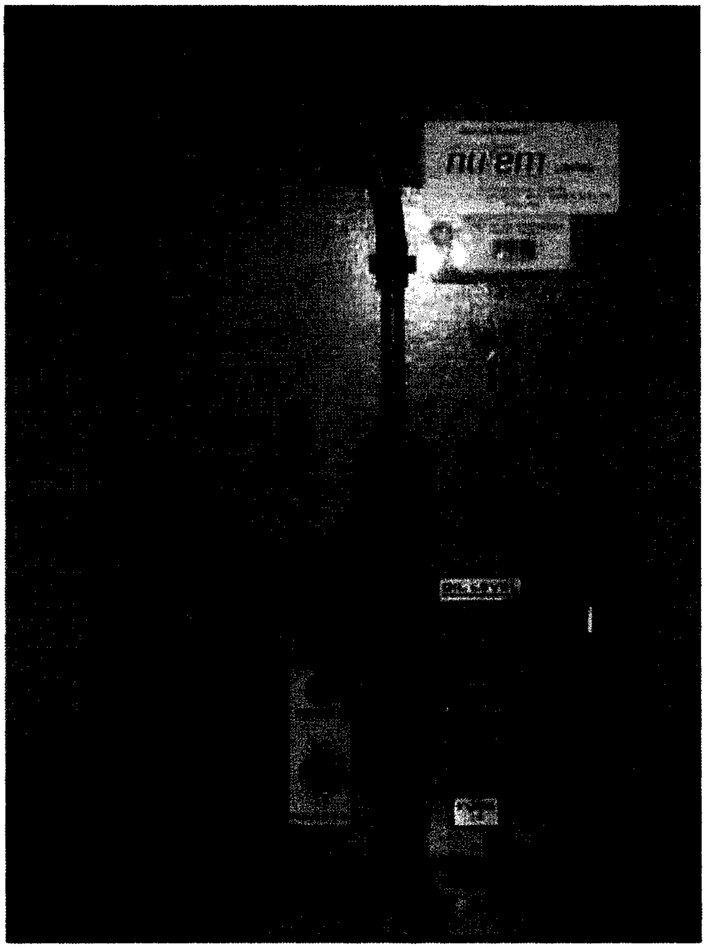

Figure 52. Nutem Integrated Smoke Generator System E.

Appendix F

Vent Diameter (mm)	Vent Diameter	Mean difference at 1.3 m/s	Mean difference at 2.3 m/s	Mean difference at 3.0 m/s
1	2 mm	12.1394	78.6905	-456.1374
	3 mm	48.3892(*)	-720.0846(*)	-1661.2311(*)
	4 mm	69.5652(*)	-1654.8257(*)	-1960.8687(*)
	5 mm	80.1697(*)	-1989.1105(*)	-2991.8414(*)
2	1 mm	-12.1394	-78.6905	456.1374
	3 mm	36.2498(*)	-798.7750(*)	-1205.0937(*)
	4 mm	57.4258(*)	-1733.5162(*)	-1504.7313(*)
	5 mm	68.0303(*)	-2067.8009(*)	-2535.7040(*)
3	1 mm	-48.3892(*)	720.0846(*)	1661.2311(*)
	2 mm	-36.2498(*)	798.7750(*)	1205.0937(*)
	4 mm	21.1760(*)	-934.7412(*)	-299.6376
	5 mm	31.7806(*)	-1269.0259(*)	-1330.6103(*)
4	1 mm	-69.5652(*)	1654.8257(*)	1960.8687(*)
	2 mm	-57.4258(*)	1733.5162(*)	1504.7313(*)
	3 mm	-21.1760(*)	934.7412(*)	299.6376
	5 mm	10.6046	-334.2847	-1030.9727(*)
5	1 mm	-80.1697(*)	1989.1105(*)	2991.8414(*)
	2 mm	-68.0303(*)	2067.8009(*)	2535.7040(*)
	3 mm	-31.7806(*)	1269.0259(*)	1330.6103(*)
	4 mm	-10.6046	334.2847	1030.9727(*)

Table 23. Mean difference in Part A mean peak force values (N) at 1.3, 2.3, and 3.0 m/s for each vent diameter (1-5 mm) across both material stiffnesses (TPU 45D and TPU 90A) – Part A. * indicates significance at $p<0.01$.

Vent Diameter (mm)	Vent Diameter (mm)	Mean difference at 1.3 m/s	Mean difference at 2.3 m/s	Mean difference at 3.0 m/s
1	2	-42.1114(*)	-58.1757(*)	3.1378
	3	-47.9158(*)	-71.1279(*)	-17.9825(*)
	4	-46.5278(*)	-63.0819(*)	-25.2316(*)
	5	-29.4273(*)	-59.2700(*)	-33.6164(*)
2	1	42.1114(*)	58.1757(*)	-3.1378
	3	-5.8044(*)	-12.9521	-21.1204(*)
	4	-4.4164	-4.9062	-28.3694(*)
	5	12.6842(*)	-1.0943	-36.7543(*)
3	1	47.9158(*)	71.1279(*)	17.9825(*)
	2	5.8044(*)	12.9521	21.1204(*)
	4	1.3880	8.0459	-7.2491
	5	18.4886(*)	11.8579	-15.6339(*)
4	1	46.5278(*)	63.0819(*)	25.2316(*)
	2	4.4164	4.9062	28.3694(*)
	3	-1.3880	-8.0459	7.2491
	5	17.1005(*)	3.8119	-8.3848
5	1	29.4273(*)	59.2700(*)	33.6164(*)
	2	-12.6842(*)	1.0943	36.7543(*)
	3	-18.4886(*)	-11.8579	15.6339(*)
	4	-17.1005(*)	-3.8119	8.3848

Table 24. Mean difference in Part A mean peak air flow rate values (m/s) at 1.3, 2.3, and 3.0 m/s for each vent diameter (1-5 mm) across both material stiffnesses (TPU 45D and TPU 90A). * indicates significance at $p<0.05$.

Vent	Vent diameter	Mean difference at 1.3 m/s	Mean difference at 2.3 m/s	Mean difference at 3.0 m/s
0	1 mm	9.7967	31.5014	-351.7760
	2 mm	46.6087	-35.4698	-430.2192
	3 mm	41.7957	-444.5223	-1713.9992(*)
	4 mm	81.1480	-1632.1380(*)	-2674.9890(*)
	5 mm	113.9061(*)	-1079.0705(*)	-2855.2657(*)
1	0 mm	-9.7967	-31.5014	351.7760
	2 mm	36.8120	-66.9712	-78.4432
	3 mm	31.9990	-476.0237	-1362.2232(*)
	4 mm	71.3513	-1663.6394(*)	-2323.2130(*)
	5 mm	104.1094(*)	-1110.5719(*)	-2503.4897(*)
2	0 mm	-46.6087	35.4698	430.2192
	1 mm	-36.8120	66.9712	78.4432
	3 mm	-4.8129	-409.0525	-1283.7799(*)
	4 mm	34.5393	-1596.6682(*)	-2244.7697(*)
	5 mm	67.2974	-1043.6007(*)	-2425.0464(*)
3	0 mm	-41.7957	444.5223	1713.9992(*)
	1 mm	-31.9990	476.0237	1362.2232(*)
	2 mm	4.8129	409.0525	1283.7799(*)
	4 mm	39.3523	-1187.6156(*)	-960.9898(*)
	5 mm	72.1103	-634.5482(*)	-1141.2665(*)
4	0 mm	-81.1480	1632.1380(*)	2674.9890(*)
	1 mm	-71.3513	1663.6394(*)	2323.2130(*)
	2 mm	-34.5393	1596.6682(*)	2244.7697(*)
	3 mm	-39.3523	1187.6156(*)	960.9898(*)
	5 mm	32.7581	553.0674	-180.2767
5	0 mm	-113.9061(*)	1079.0705(*)	2855.2657(*)
	1 mm	-104.1094(*)	1110.5719(*)	2503.4897(*)
	2 mm	-67.2974	1043.6007(*)	2425.0464(*)
	3 mm	-72.1103	634.5482(*)	1141.2665(*)
	4 mm	-32.7581	-553.0674	180.2767

Table 25. Mean difference in Part B mean peak force values (N) at 1.3, 2.3, and 3.0 m/s for each vent diameter (1-5 mm) across both material stiffnesses (TPU 45D and TPU 90A). * indicates significance at $p<0.01$.